NASA CR-72479

DEVELOPMENT OF A TURBOCOMPRESSOR GAS BEARING SIMULATOR

by

S. V. Lukas

prepared for

NATIONAL AERONAUTICS AND SPACE ADMINISTRATION

CONTRACT NAS 3-10927

UNION CARBIDE CORPORATION
Linde Division
Tonawanda, New York

Requests for copies of this report should be referred to:

National Aeronautics and Space Administration
Scientific and Technical Information Facility
P.O. Box 33
College Park, Md. 20740

NASA CR-72479

FINAL REPORT

DEVELOPMENT OF A TURBOCOMPRESSOR GAS BEARING SIMULATOR

by

S. V. Lukas

prepared for

NATIONAL AERONAUTICS AND SPACE ADMINISTRATION

October, 1968

CONTRACT NAS 3-10927

Technical Management
NASA Lewis Research Center
Cleveland, Ohio
Space Power Systems Division
Henry B. Tryon, Project Manager

UNION CARBIDE CORPORATION
Linde Division
Tonawanda, New York

FOREWORD

This report was prepared in accordance with Contract NAS3-10927 under the technical management of Henry B. Tryon of the Space Power Systems Division, and in consultation with William J. Anderson of the Fluid System Components Division, NASA Lewis Research Center, Cleveland, Ohio.

The work was conducted from June, 1967 to September, 1968 by the Linde Division of Union Carbide Corporation, Tonawanda, New York.

TABLE OF CONTENTS

LIST OF FIGURES

FINAL REPORT

DEVELOPMENT OF A TURBOCOMPRESSOR GAS BEARING SIMULATOR

by

S. V. Lukas

ABSTRACT

The Linde Division of Union Carbide Corporation has designed, built and tested a gas bearing simulator for a Brayton cycle radial flow turbocompressor. The gas bearing system consists of two cylindrical journal bearings supported on damped, flexible supports and a double-acting spiral-grooved thrust bearing. The stability of the journal bearings in the horizontal and vertical positions was investigated experimentally.

1.0 SUMMARY

This report describes the design, fabrication and testing in ambient air of a gas bearing simulator for a Brayton cycle radial flow turbocompressor.

The simulator consists of a two-wheel rigid rotor with a center bore, gas-supported on a stationary shaft. The shaft, in turn, is supported by two flexible supports. Damping is provided to the shaft by dashpots. The bearings are of the self-acting type with feeding holes for hydrostatic start-up and shut-down. The two journal bearings are of the full 360° cylindrical type, and the double-acting thrust bearing of the spiral-grooved inward pumping type. The simulator was operated in both the horizontal and vertical attitudes. The simulator was fully instrumented to measure bearing, rotor, and shaft performance.

Static tests were conducted in the vertical position to determine the flexible support stiffness, shaft damping, hydrostatic journal and thrust bearing stiffnesses, and bearing flow rates.

The simulator was operated hydrodynamically in the horizontal and vertical positions. In the horizontal position 94% of the design speed (38,500 rpm) and 78% of the overspeed (46,200 rpm) was reached. It is expected that further improvements will enable this bearing system to reach the overspeed condition. In the vertical position the rotor was operated hydrodynamically up to 12,000 rpm. The rotor whirled at all speeds with a frequency approximately one-half the rotational frequency. However, journal bearing stability in the vertical position was achieved with low supply pressures and therefore low gas consumption. A speed of 30,000 rpm was reached with a supply pressure of 18 psig.

The combined hydrodynamic-hydrostatic double acting thrust bearing did not exhibit any pneumatic instability at any supply pressure.

Chrome oxide, bearing surfacing material, was found quite effective in preventing bearing seizure when rubbing of the mating bearing surfaces occurred.

2.0 INTRODUCTION

NASA has presently under development a Brayton cycle space power system. Gas bearings are incorporated into current Brayton cycle turbomachinery because of their potential for long life and their ability to run on the system gaseous working fluid with no contaminating lubricant. The life requirement of such bearings is 10,000 hours with no maintenance or replacement. Present gas bearing designs are of the pivoted-pad type and may have a limited life due to fretting or wear at the pivot point. Plain cylindrical journal bearings cannot be used because they are unstable at high speeds and in the zero "g" environment.

An alternate gas bearing design would be full cylindrical journal bearings on flexible and damped supports. Flexibility and damping are necessary to provide journal bearing stability at high speeds. Work performed by the Linde Division of Union Carbide Corporation under Contract NAS3-8516 has indicated the applicability of such a bearing system to an existing Brayton cycle radial flow turbocompressor developed under Contract NAS3-2778.

The design of Linde's gas bearing system developed under Contract NAS3-8516 and incorporated into the radial flow turbocompressor is shown in Figure 1. The bearing system consists of two self-acting journal bearings located under the compressor and turbine wheels, and a double-acting spiral-grooved thrust bearing located near the compressor wheel. The spiral-grooved thrust stator is an integral part of the shaft. The stationary hollow shaft is mounted to the inlet and outlet ducting of the turbocompressor by flexible supports. This arrangement provides thermal isolation of the bearings from the housing and, therefore, the journal bearing clearances will be affected only slightly since the shaft and rotor will follow the same temperature excursions. The compressor and turbine inlet temperatures are 536°R and 1950°R, respectively. Damping, required for journal bearing stability, is provided by the pellets within the tube. The rotor consists of two pieces bolted together at the thrust stator.

All bearings are provided with feeding holes, and pressurized argon (cycle working fluid) is introduced through the compressor end flexible support for hydrostatic start-up and shut-down. The operating speed of the turbocompressor is 38,500 rpm and the overspeed 46,200 rpm.

The object of the present work is to design, fabricate, and test in ambient air a dynamic simulator to substantiate the work done under Contract NAS3-8516 with actual performance data. Although the simulator does not fully simulate the turbocompressor conditions (hot argon), it nevertheless provides sufficient information about the required flexible support stiffness and damping for journal bearing stability which is the primary objective of this work. The simulator design is shown in Figure 2 and the details of the design are discussed in the following sections.

FOLDOUT FRAME 1

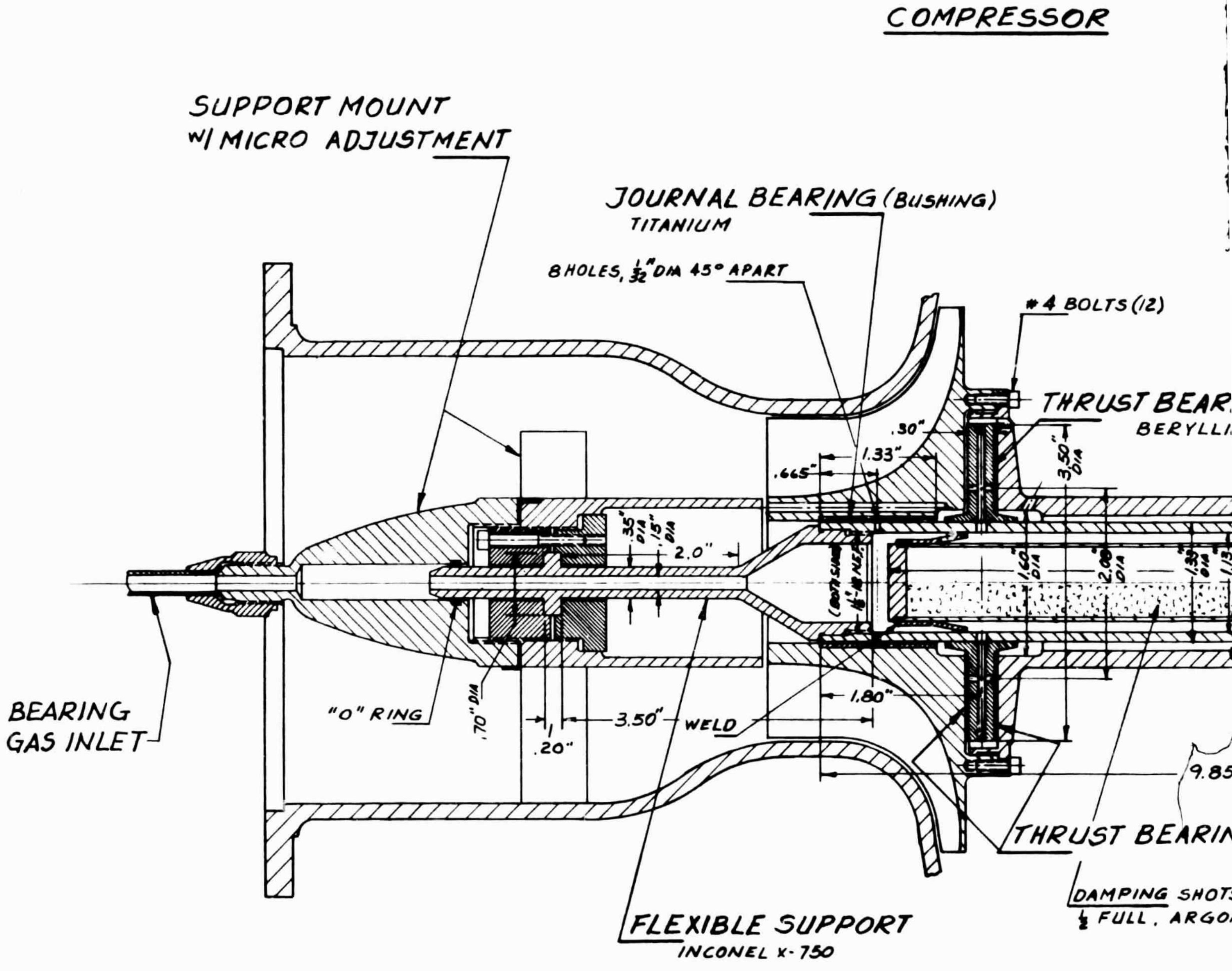

FIG. 1 BEARING AND SUPPO
TURBOCOMPRESSO

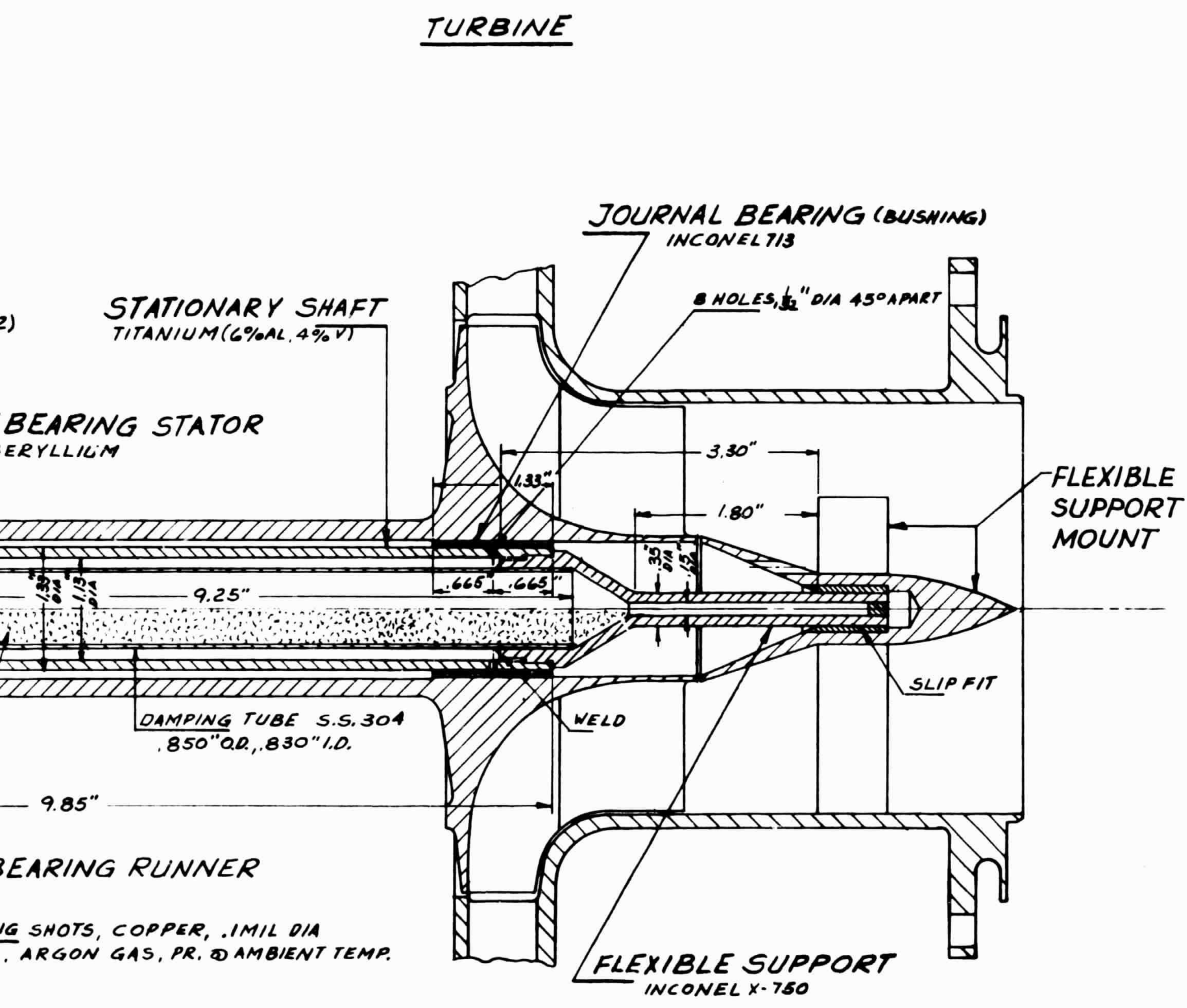

UPPORT SYSTEM FOR RADIAL FLOW
RESSOR - CONTRACT NAS3-8516

FOLDOUT FRAME 1

(2) STATIONARY SHAFT

(3) THRUST STATOR

(5)(6)(7)(8) ROTOR

(8) THRUST RUNNERS

(9)(10) FLEXIBLE SUPPORTS

(12)(13)(14)(15)(16)(17) DASHPOT

(14) DASHPOT DAMPING ADJUS

(21) THRUST BRG. LOADING D

(34) ROTOR DRIVE NOZZLES

(38)(39) JOURNAL BRG. FEEDING H
SEAL-OFF PISTON ROD

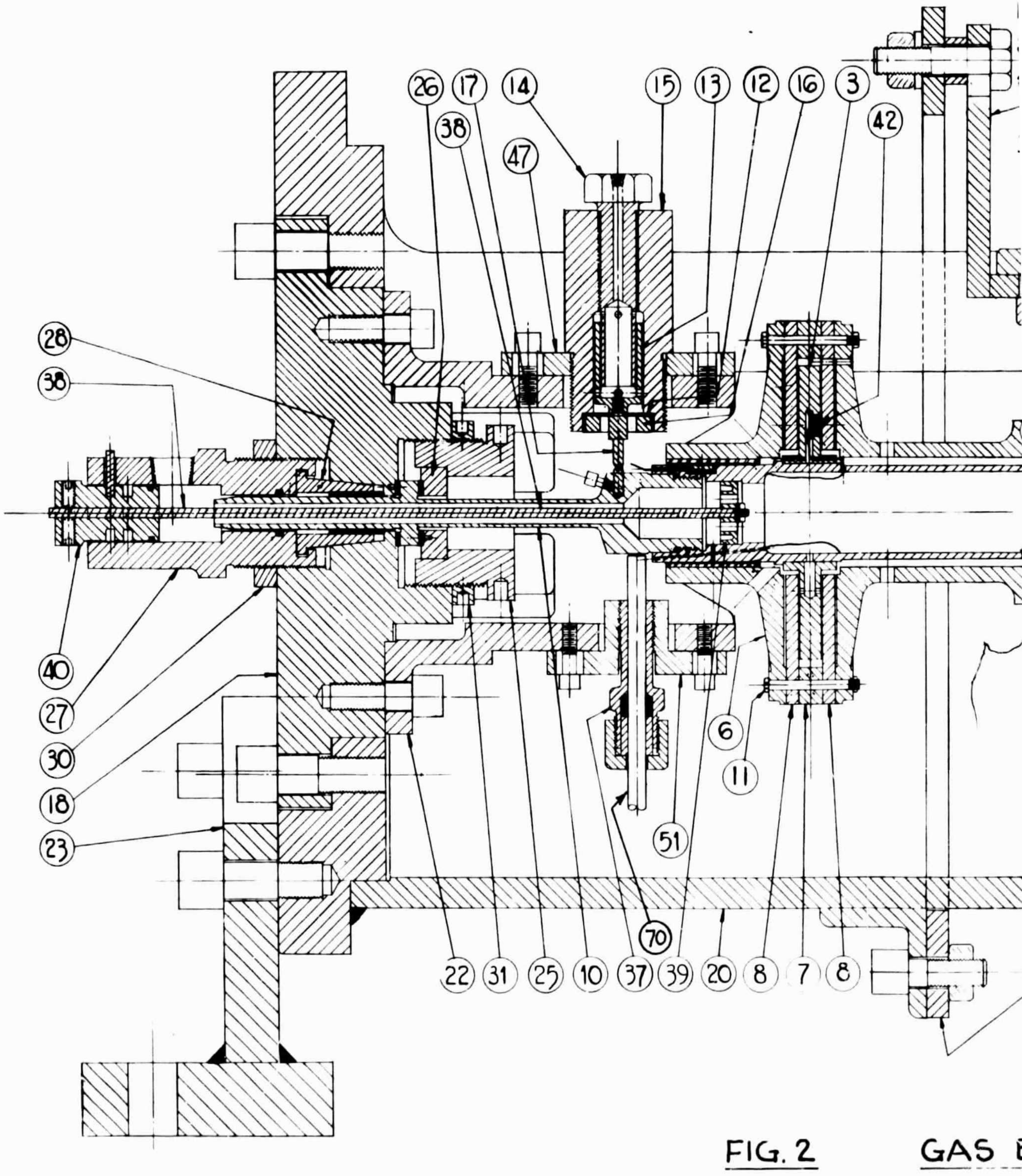

FIG. 2 GAS

RADIAL

FOLDOUT FRAME 2

NG ADJUSTING NUT

OADING DEVICE

IOZZLES

EEDING HOLES
ON ROD

(42) ROTOR MOTION RELATIVE TO SHAFT PICKUP CAPACITORS

(70) SHAFT MOTION RELATIVE TO FRAME CAPACITANCE PROBES

(71) ROTOR SPEED PICKUP PROBE

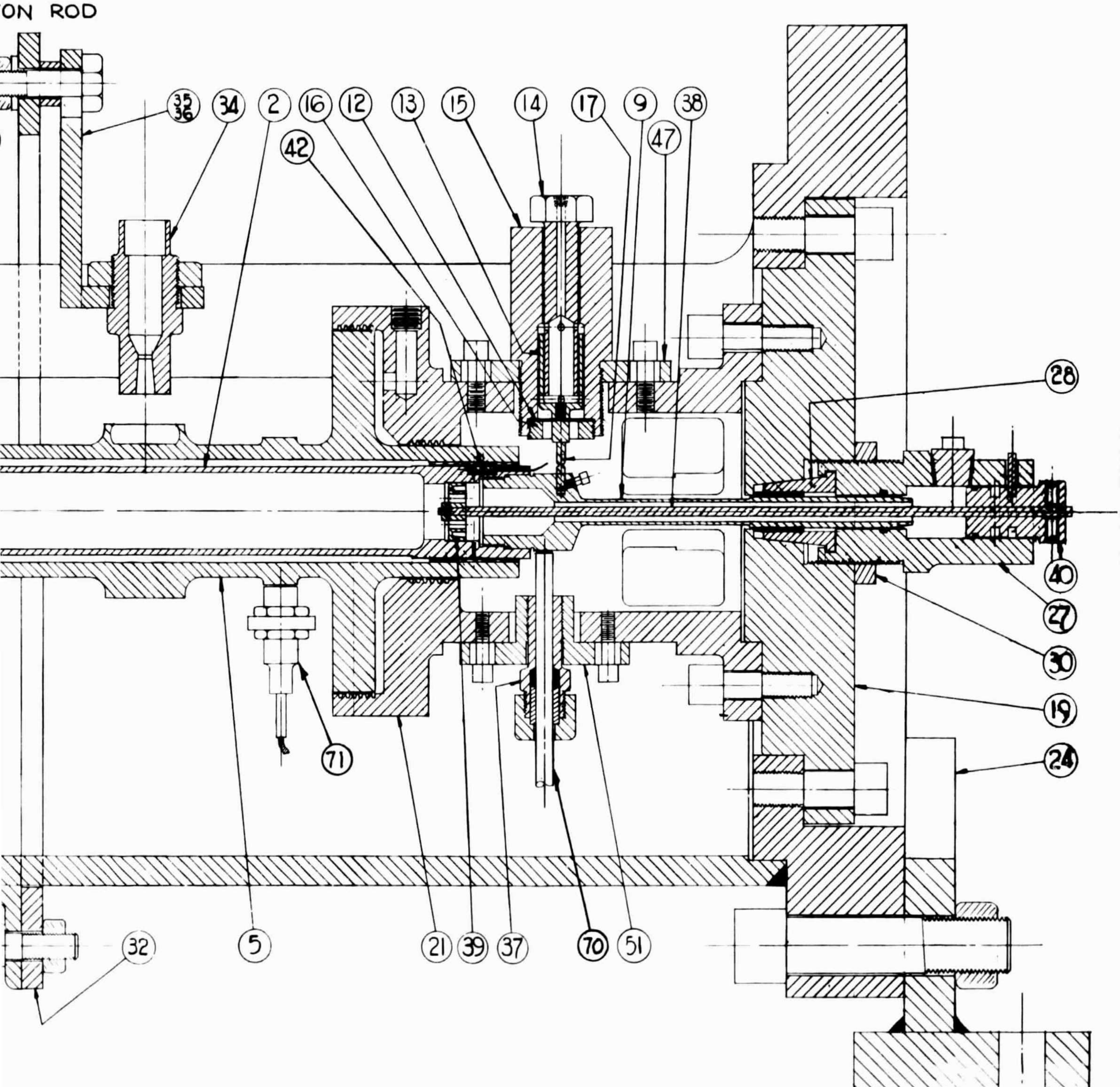

GAS BEARING SIMULATOR FOR
RADIAL FLOW TURBOCOMPRESSOR

3.0 SIMULATOR DESIGN

3.1 Simulator Rotor

Figure 3 shows an exploded view and Figure 4 an assembled view of the rotor. The overall length of the rotor is 11 inches, the O.D. of both wheels is 5.2 inches, and the bore diameter is 1.5 inches.

The design requirements of the simulator rotor were to duplicate the inertia properties of the compressor and turbine wheels of the radial flow turbocompressor and to minimize the centrifugal distortion of the thrust runner surfaces. The measured inertia properties of the rotor assembly were:

Mass:	0.02752 lb-sec^2/in
Transverse Moment of Inertia:	0.3209 lb-sec^2-in (about c.g.)
Polar Moment of Inertia:	0.07216 lb-sec^2-in
Center of Gravity:	5.406 in. (from the left end face of the rotor, Figure 2)

The distance between the center of bearing centers and the center of gravity of the rotor was kept as small as possible (0.094 in.) to uncouple the cylindrical and conical modes of vibration.

The compressor wheel and thrust runner arrangement is shown in Figure 5. This arrangement was chosen so that the axial deflections due to centrifugal forces of the thrust bearing running surfaces are small in comparison to the operating clearance (0.82 mils). Members 5 and 6 are made of 17-4 PH stainless steel, member 8 of 7075-T6 Aluminum, and member 7 of Beryllium Special (68,500 psi Y.S. and 72,500 psi U.T.S.) The five rotating members are

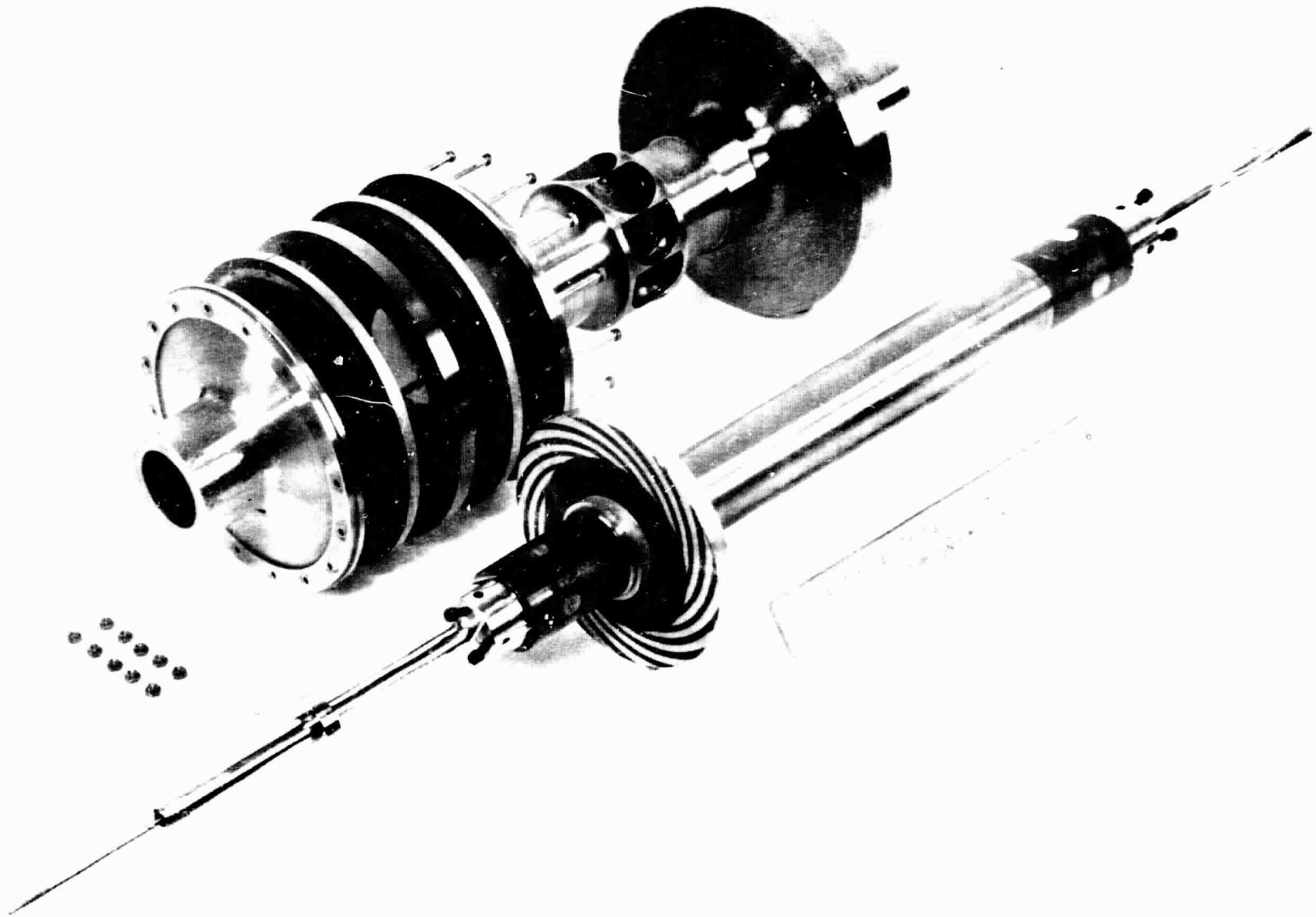

Fig. 3 - Rotor Parts and Shaft with Thrust Stator

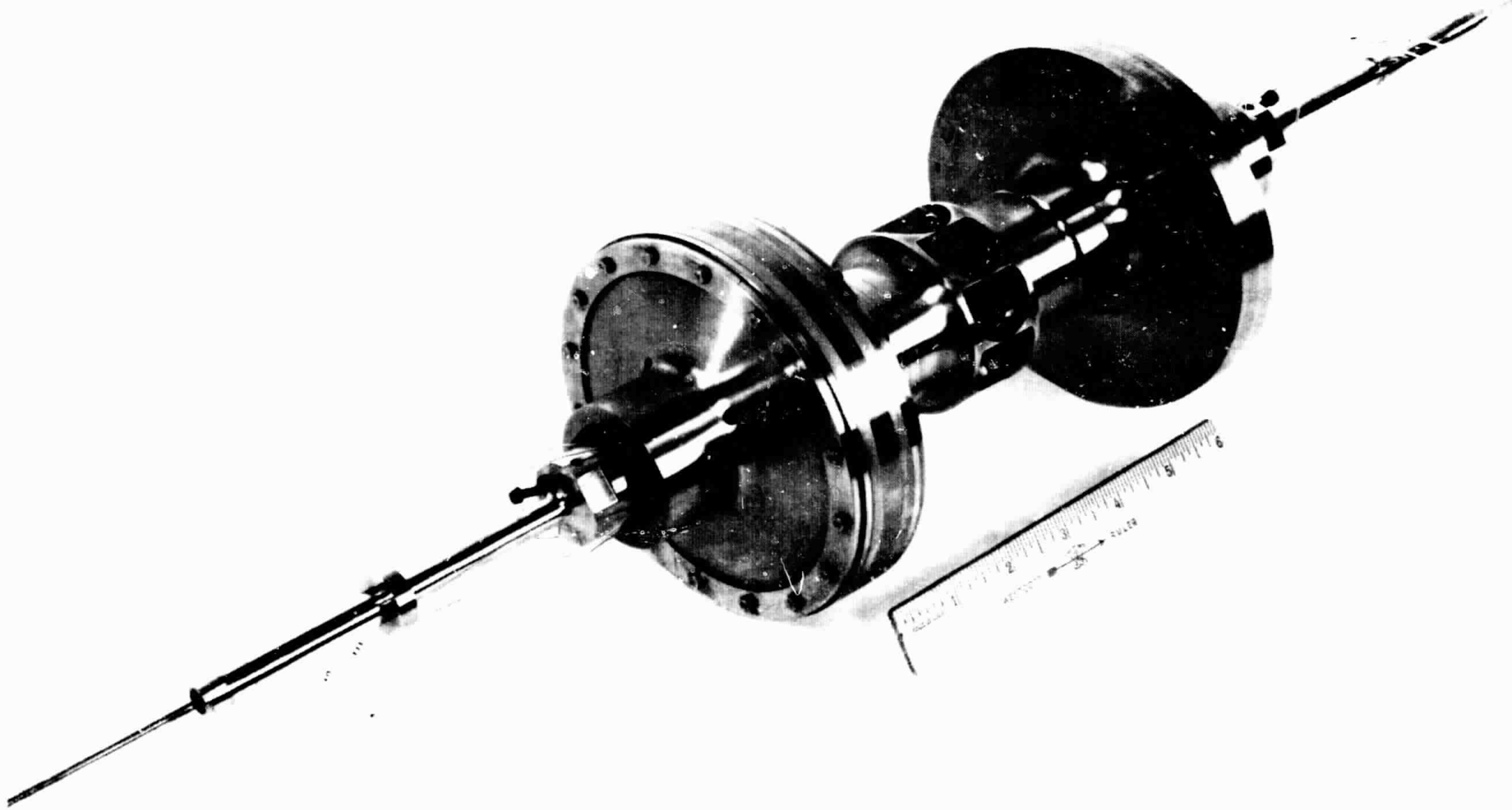

Fig. 4 - Shaft-Rotor Assembly

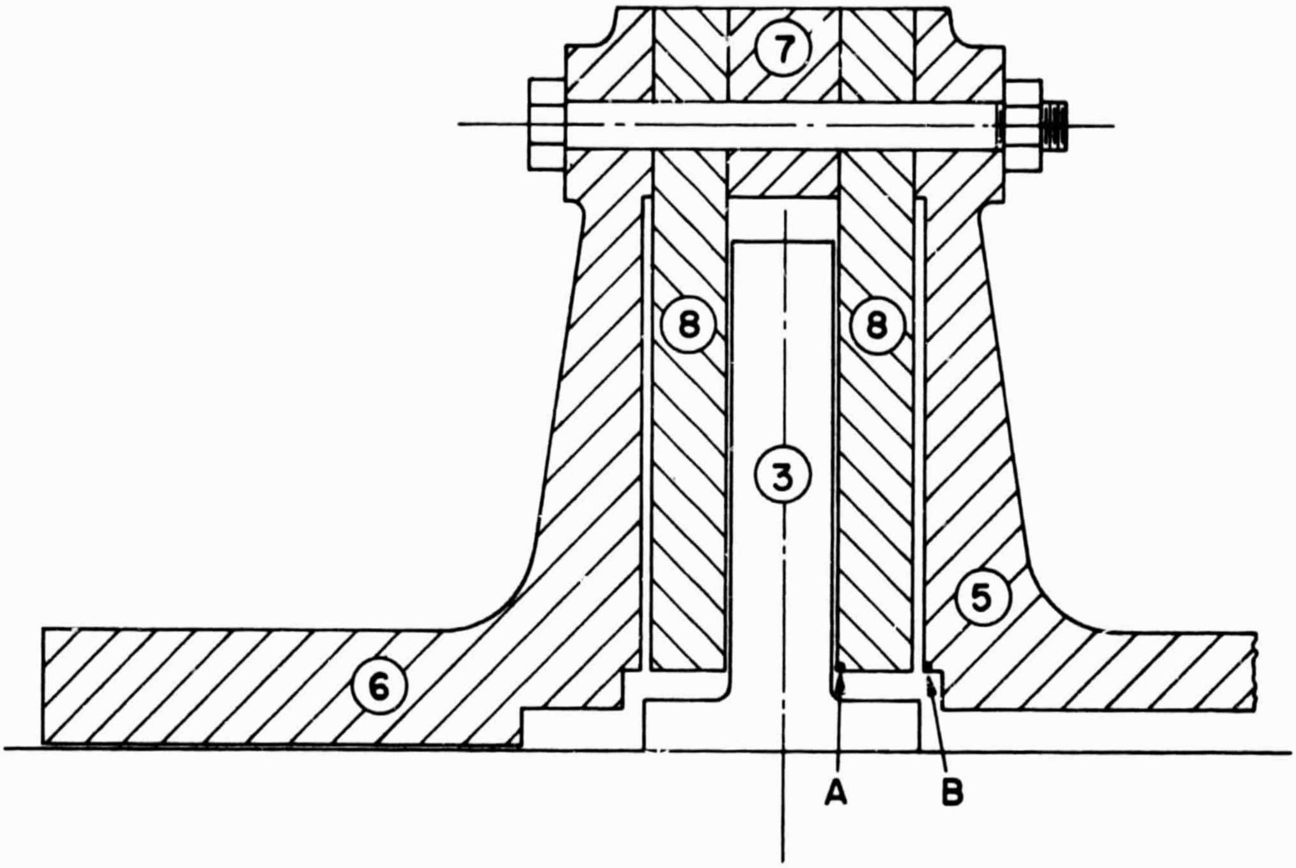

Figure 5

Compressor Wheel and Thrust Runner Arrangement

held together by sixteen 1/8 inches diameter bolts (17-4 PH). To assure alignment between the two journal bearings when the rotor is disassembled and reassembled the diametral clearance between bolt and hole was maintained at 0.2 mils. The stresses and deflections of the rotor were calculated by a computer program which is described in the Appendix. At 46,200 rpm (overspeed condition) the axial deflection of point A in member 8 (Figure 5) is 0.04 mils and of point B in member 5 is 3.96 mils. The gap (0.025 inches) between members 5 and 8 is to allow for the large axial deflection of member 5. At the same speed, the hoop stress of member 7 at the inner periphery is 50,000 psi.

The flexural critical speed of the rotor is approximately 83,000 rpm which is much higher than the overspeed.

The rotor was driven by an impulse turbine. The turbine buckets were cut on a 2.5 inch diameter wheel located at the center of gravity of the rotor. The four convergent-divergent nozzles were attached to the frame of the simulator.

3.2 Simulator Shaft

An assembled view of the shaft, thrust stator, and flexible supports is shown in Figure 3. The shaft has an overall length of 11.375 inches (excluding flexible supports), an O.D. of 1.3 inches, and an I.D. of 1.1 inches. The shaft is made of Titanium (6% Al, 4% V) in order to conserve weight. The smaller the shaft mass the higher the threshold of stability. The measured inertia properties of the shaft-thrust stator combination were:

Mass:	0.004517 lb-sec^2/in
Transverse Moment of Inertia:	0.08718 lb-sec^2-in (about c.g.)
Polar Moment of Inertia:	0.003333 lb-sec^2-in

The flexural critical speed of the stationary shaft is approximately 100,000 rpm, which is again much higher than the overspeed.

3.3 Thrust Stator

Beryllium was initially selected for the thrust stator material. The two reasons for selecting beryllium were, a) small thermal distortion and b) lightweight. However, attempts to coat with chrome oxide a test thrust stator were unsuccessful. Although the chrome oxide will adhere to beryllium, the bonding strength was found to be weak. Therefore, the coating could be easily removed from the corners. Figure 6 shows a beryllium test thrust stator coated with chrome oxide. Some of the coating came off when the plug was removed from the feeding hole.

As a result of this, an alternate material, 7075-T? aluminum was used. Figure 7 is a view of the chrome oxide coated aluminum thrust stator. Each face of the stator is a combination of a hydrodynamic (spiral-grooved) and hydrostatic (inherently compensated) thrust bearing. The grooves were formed by building up with chrome oxide the ungrooved section. Therefore, the groove depth is equal to the chrome oxide thickness. Two separate stainless steel (type 301, 0.010 in. thick) masks were used. One mask was used to plasma spray the hydrodynamic (spiral ridges) and the other one the hydrostatic section. The feeding holes, being of large size (1/16 inches in diameter), were not masked (or plugged) during the plasma spraying process. The geometrical and operating parameters of the thrust bearing are discussed in Section 3.7.

3.4 Flexible Supports

A view of the flexible supports screwed into each end of the shaft is shown in Figure 3. The supports are hollow so that pressurized air can be introduced during hydrostatic operation of the rotor. The material of the flexible supports is Inconel X-750. They have an O.D. of 0.375 inches, an I.D. of 0.281 inches and an effective length of 2.5 inches. The flexible support stiffness

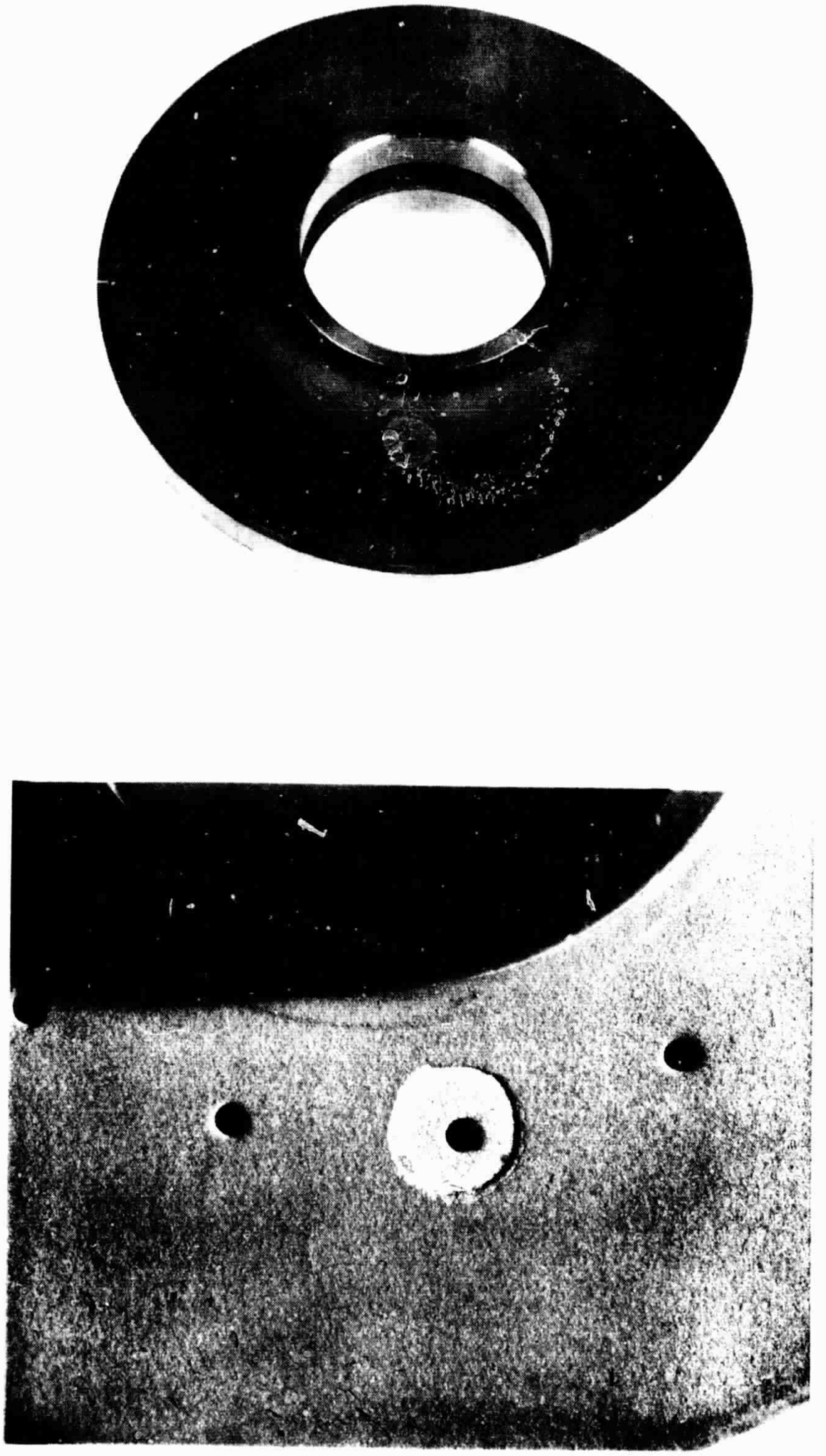

Fig. 6 - Chrome Oxide Coated Beryllium Test Thrust Stator. The Coating Came Off From The Vicinity Of A Feeding Hole Due To Poor Bonding

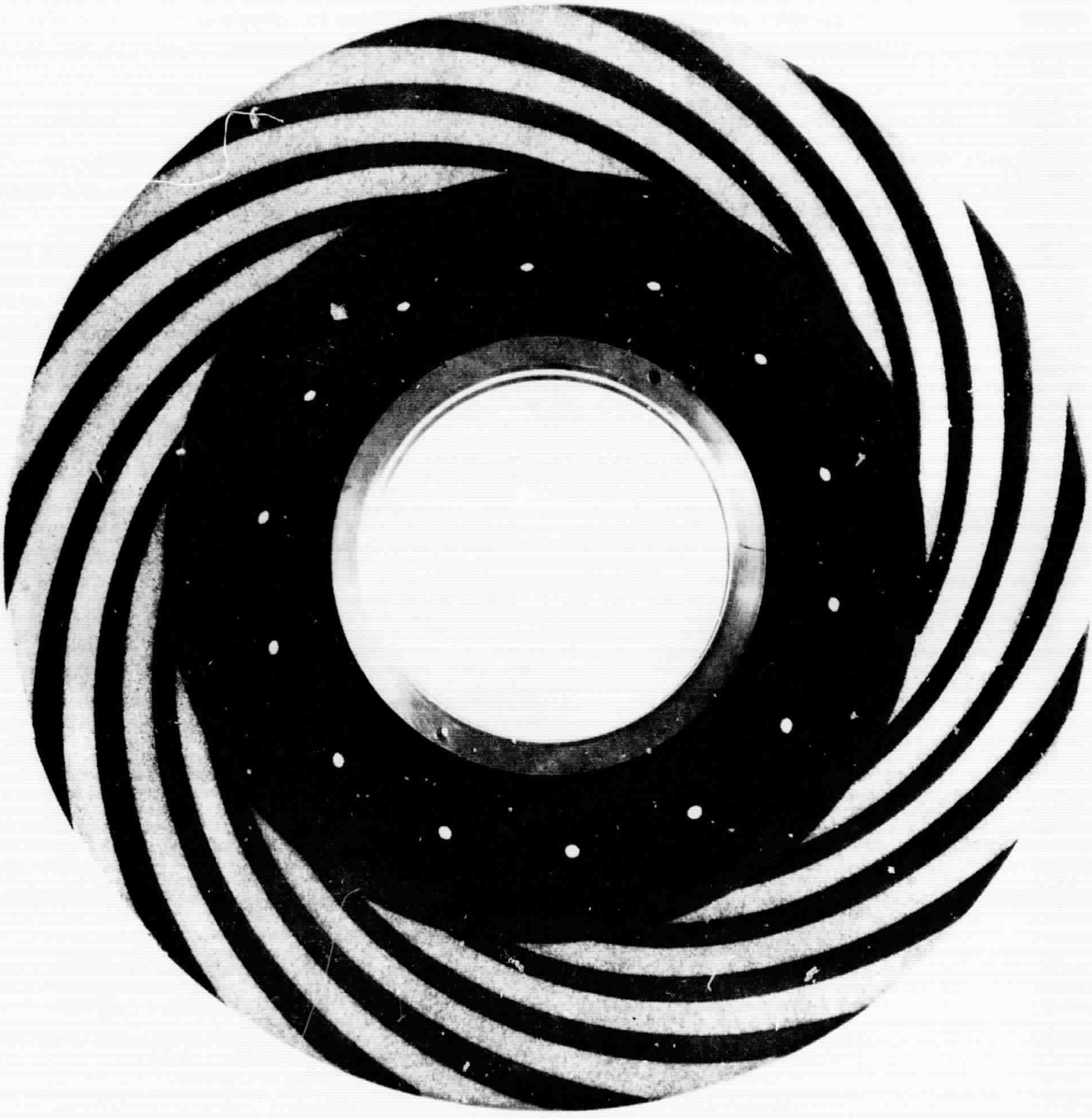

Fig. 7 - Chrome Oxide Coated Aluminum Thrust Stator. Combined Hydrodynamic And Hydrostatic Thrust Bearing Surface.

depends on the manner in which the ends are restricted. The calculated average stiffness per support was 8,700 lbs/in for end conditions between fixed and simply supported. During test work it was found that lower stiffness was needed to increase the journal bearing threshold of instability. This was done by mounting the flexible supports in rubber bushings. In this manner, stiffnesses as low as 2,000 lbs/in were obtained.

3.5 Shaft Damping - Dashpots

Shaft damping is required for journal bearing stability. In the initial design (Figure 1) damping is provided by inserting a tube within the stationary hollow shaft. The tube is filled to approximately one-half of its volume with copper shot of 0.1 mils in diameter. However, damping shot of the desired size could not be obtained. As a result of this, viscous dampers (dashpots) have been used in the simulator. Two dashpots, located 90 degrees apart, were installed at each end of the shaft as shown in Figure 8. The orbiting motion of the shaft causes surface A to move with respect to the stationary surface B. The cylindrical gap (1.5 mils) between surfaces A and B contains silicone fluid with a viscosity of 30,000 cs (4.17×10^{-3} lb-sec/in^2). The amount of damping can be varied by the adjustment nut which increases or decreases the overlapping distance ℓ between surfaces A and B. The damping is maximum when the adjustment nut is fully screwed in.

The dashpot damping coefficient is given by the simple expression:

$$B = \frac{A\mu}{h} = 4.367\,\ell \tag{1}$$

where B = viscous damping coefficient per dashpot, lb-sec/in

A = area = $0.5\pi\ell$ in^2

ℓ = overlapping distance, in.

μ = silicone fluid viscosity = 4.17×10^{-3} lb-sec/in^2

h = gap = 1.5×10^{-3} in.

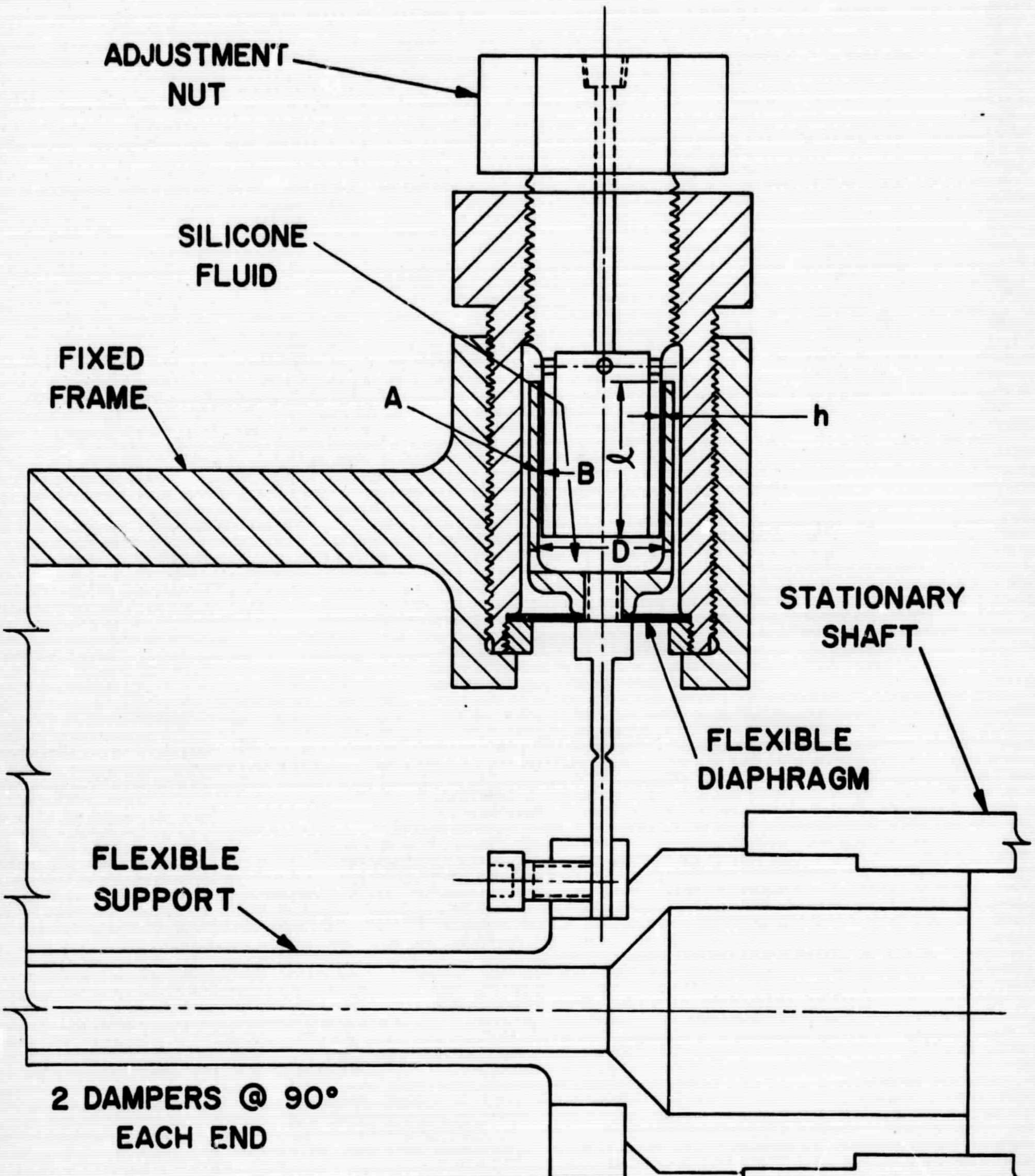

Figure 8

Dashpot – Shaft Arrangement

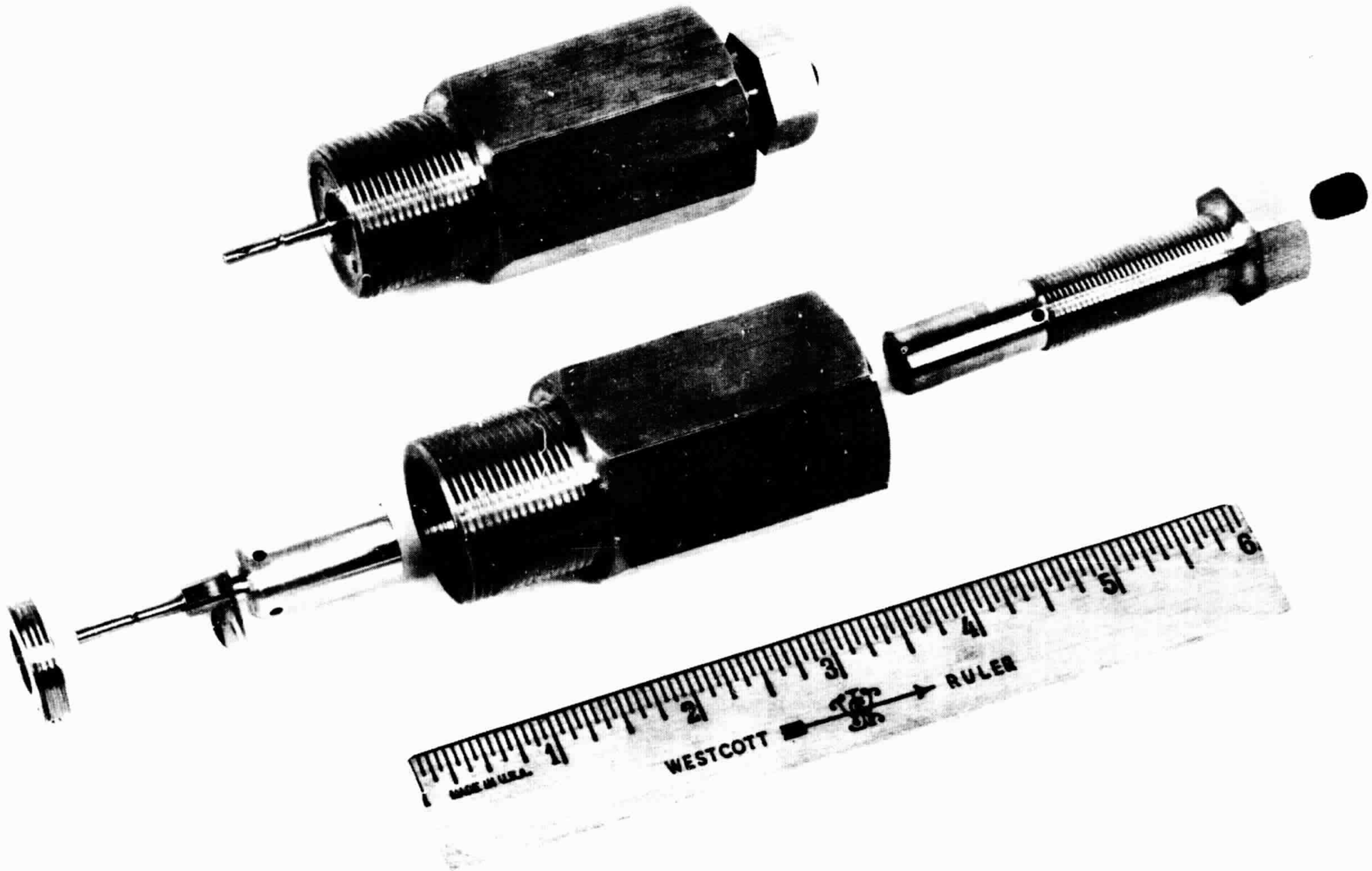

Fig. 9 - Dashpot Assembly and Dashpot Parts

Analytical and experimental data of dashpot damping coefficients is given in Section 5.2. Figure 9 is a view of the dashpot assembly and dashpot parts.

3.6 Journal Bearings

The simulator has two full cylindrical journal bearings of the self-acting type. The journal bearings are provided with feeding holes (inherently compensated type) for hydrostatic start-up and shut-down. During hydrodynamic operation the feeding holes can be sealed off to prevent loss of load carrying capacity due to leakage. This is accomplished by a nylon piston guided by a rod as shown in Figure 2 (Items 38 and 39). The piston rods are operated pneumatically.

The journal bearing and associated parameters are:

Bearing length	1.313 in.
Bearing diameter	1.316 in.
Length-to-diameter ratio	1
Zero speed radial clearance	0.65 mils
Diameter of feeding holes	1/32 in.
Number of feeding holes	8 (per brg)
Bearing span	9.687 in. (center to center)
Lubricant gas	air
Viscosity	2.6×10^{-9} lb-sec/in^2
Ambient pressure	14.7 psia
Gravity load	5.313 lb. (per brg)
Substrate Materials	
Shaft	Titanium (6% Al, 4% V)
Bushing	17-4 PH Stainless Steel
Surfacing Material	Chrome Oxide

The measured rotor bore and shaft O.D. dimensions at each journal bearing are as follows:

	Compressor End Journal Brg	Turbine End Journal Brg
Rotor I.D., in.	1.3164	1.31610 to 1.31615
Shaft O.D., in.	1.3151 (0.00015 neg. taper)	1.3148 (max. deviation 0.00005)

The journal bearing performance parameters in the horizontal position are shown in the following Figures:

Figure 10 - Radial Clearance vs. Speed

Figure 11 - Compressibility Number vs. Speed

Figure 12 - Eccentricity Ratio vs. Speed

Figure 13 - Hydrodynamic Film Stiffness vs. Speed

The centrifugal growth of the radial clearance was calculated from the displacement equation (2) of an annular disk at the inside radius. This assumes the rotor portion along the journal bearing as an annular disk.

$$\Delta c = \frac{\rho \omega^2}{4Eg} \left[(3 + \nu) r_i r_o^2 + (1 - \nu) r_i^3 \right] \qquad (2)$$

Where Δc = centrifugal growth, in.

ρ = density = 0.281 lb_m/in^3

E = modulus of elasticity = 28.5×10^6 lb_f/in^2

ν = Poisson's ratio = 0.272

r_i = inside radius = 0.658 in.

r_o = outside radius = 0.950 in.

g = dimensional constant = 386.09 in-lb_m/lb_f-sec^2

ω = rotor speed, rad/sec

material = 17 - 4PH Stainless Steel

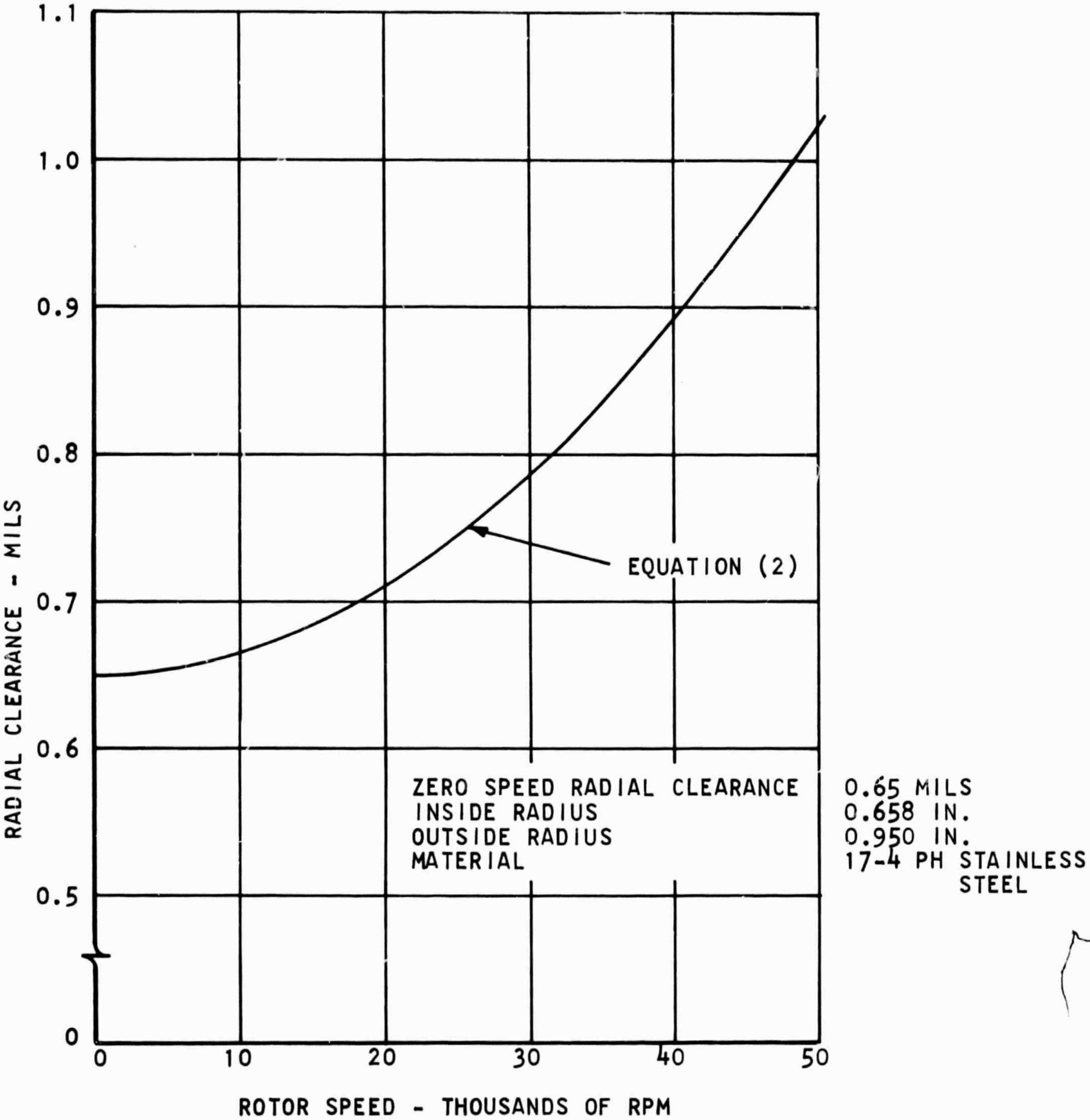

Fig. 10 - Illustrating Growth of Journal Bearing Radial Clearance vs. Rotor Speed

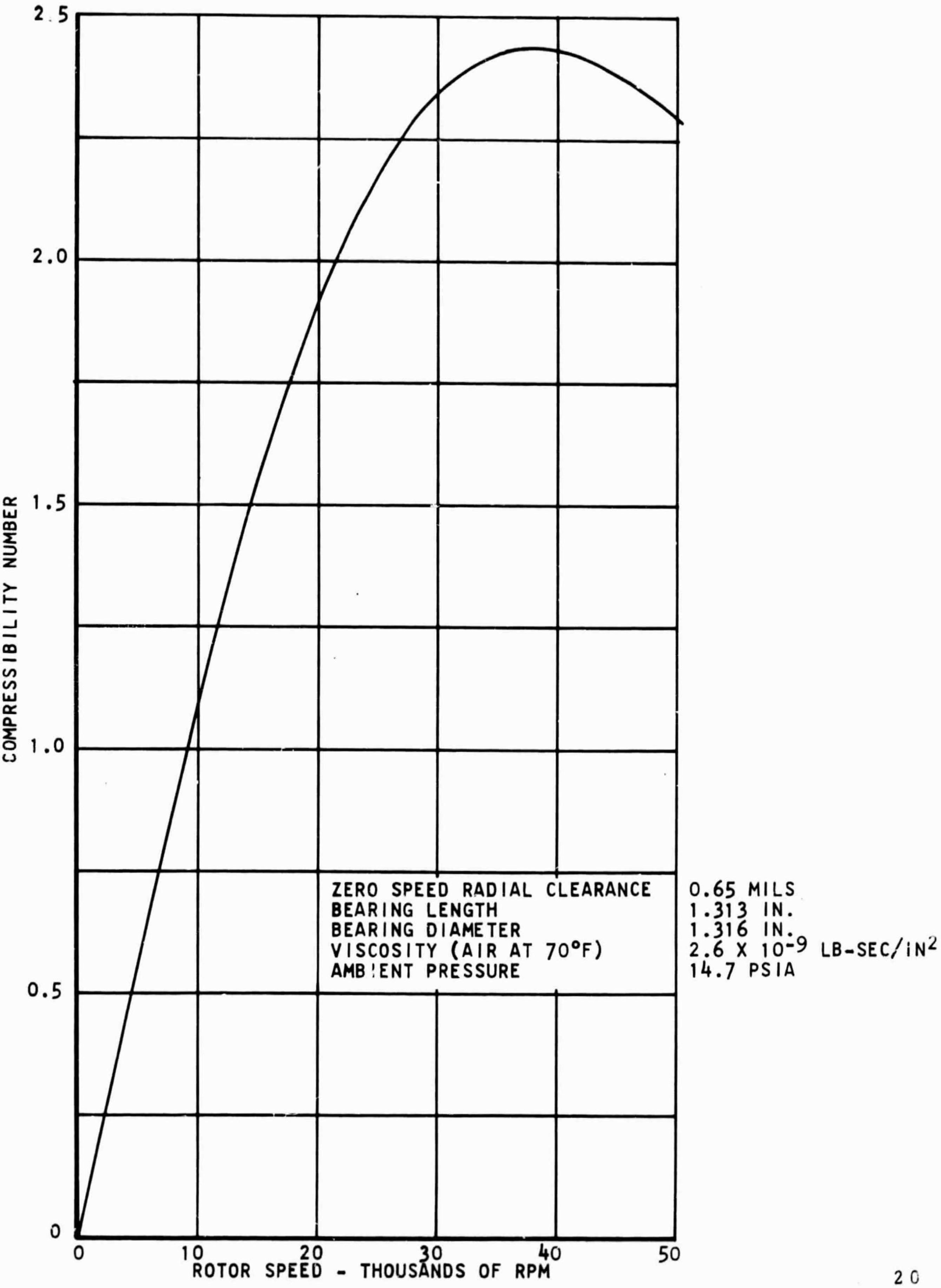

Fig. 11 - Journal Bearing Compressibility Number vs. Rotor Speed

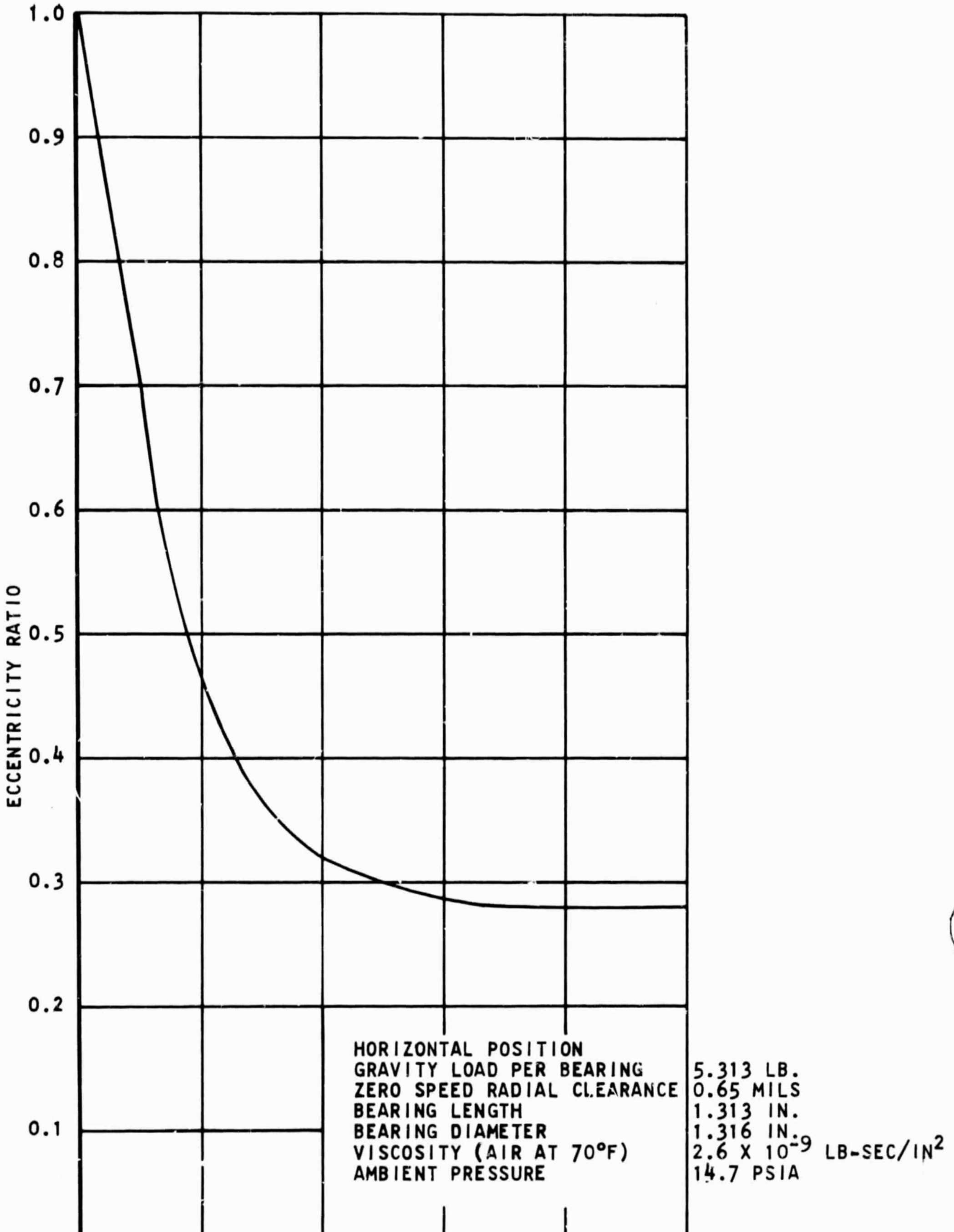

Fig. 12 - Journal Bearing Eccentricity Ratio vs. Rotor Speed

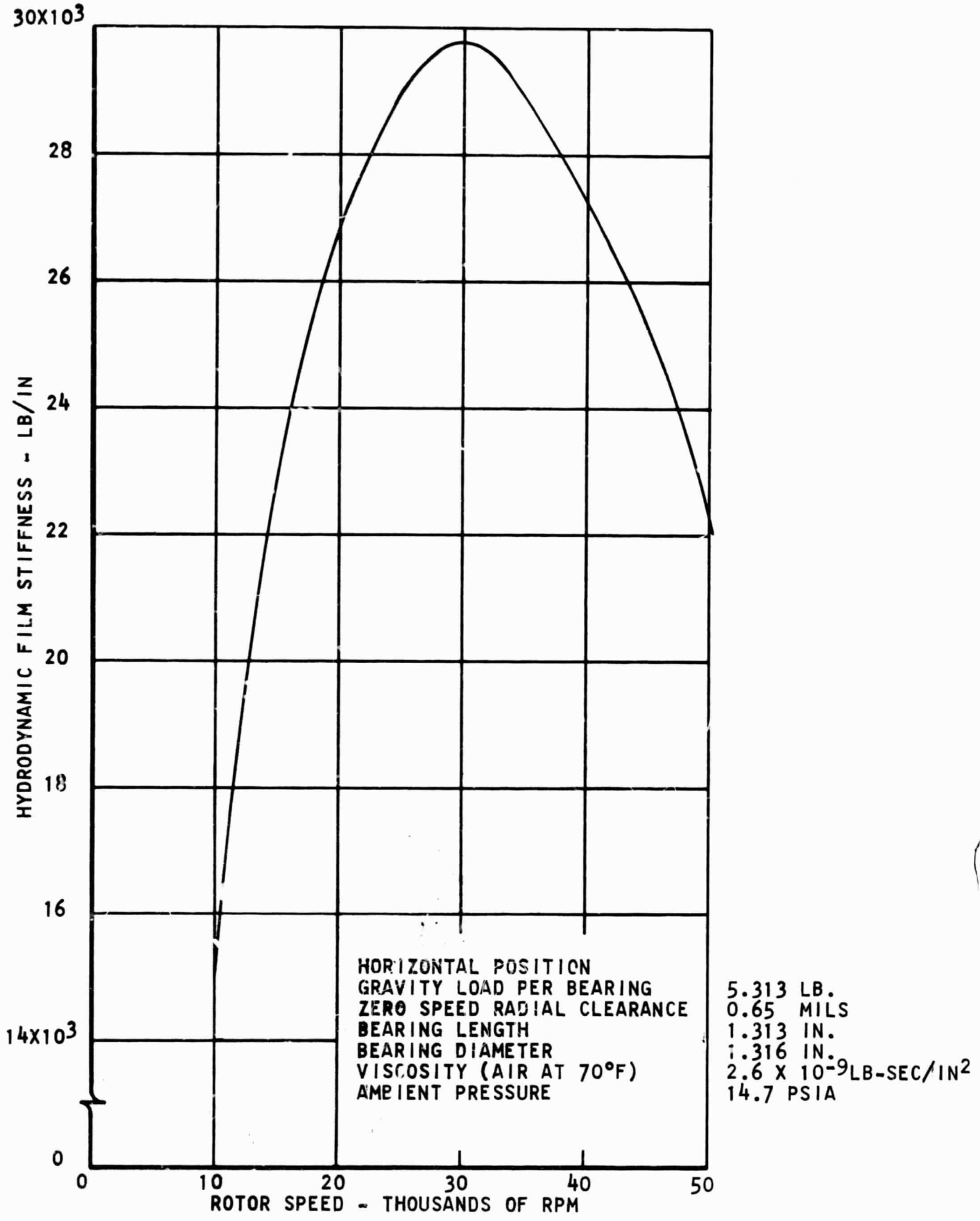

Fig. 13 - Journal Bearing Hydrodynamic Film Stiffness vs. Rotor Speed

The variation of the eccentricity ratio and hydrodynamic film stiffness with respect to speed was calculated from Reference (1).

3.7 Thrust Bearing

The simulator has a double-acting hydrodynamic thrust bearing. Both faces of the thrust stator have inward pumping spiral grooves and feeding holes (inherently compensated type) for hydrostatic start-up and shut-down. The thrust runners are plain surfaces. The geometrical and operating parameters of the thrust bearing are as follows:

Outside groove radius	2.0 in.
Inside groove radius	1.379 in.
Feeding hole circle radius	1.069 in.
Inside radius	0.85 in.
Number of grooves	15
Groove depth	2.45 mils
Groove angle	17.5 degrees
Groove width (arc)	14.5 degrees
Ridge width (arc)	9.5 degrees
Groove-to-ridge width ratio	1.53
Total axial clearance	6 mils
Diameter of feeding holes	1/16 in.
Number of feeding holes	14
Lubricant gas	air
Viscosity	2.6×10^{-9} lb-sec/in^2
Ambient pressure	14.7 psia
Stator and runner material	7075-T6 aluminum
Stator and runner surfacing material	Chrome oxide
At 38,500 rpm with 35 lb. thrust load	
Running clearance	0.82 mils
Compressibility number	10.5
Stator thermal distortion	0.1 mils (at the outer rim)

The thrust bearing was designed from the design information given in Reference (1).

The change in the bearing gap, Δh, due to the thermal distortion of thrust stator was calculated by the equation:

$$\Delta h = \frac{\alpha}{k} \quad \frac{0.5 \mu \omega^2 (R_o^{\ 2} + R_i^{\ 2})}{4Jh} \tag{3}$$

where:

Δh = change of gap at outer rim, in.

α = coefficient of linear thermal expansion = 13.0×10^{-6} per °F

k = coefficient of thermal conductivity = 0.0194 Btu/sec-ft-°F

μ = viscosity = 2.6×10^{-9} lb-sec/in^2

ω = speed = 4,032 rad/sec

R_o = thrust bearing outside radius = 2.0 in.

R_i = thrust bearing inside radius = 0.85 in.

h = gap = 0.00082 in.

J = Joule constant = 778 ft-lb/Btu

The derivation of Equation (3) which is given in Reference (2) assumes:

a. The temperature gradient across the faces of the thrust plate is linear.

b. The temperature at each face is uniform.

c. The bearing gap is constant

d. One-half of the heat generated flows axially through the thrust plate.

The coordinates (r, θ) of the spiral grooves were calculated from the equation of logarithmic spiral

$$r = R_g \, e^{\theta \tan \beta} \tag{4}$$

where

R_g = inside groove radius = 1.379 in.

β = groove angle = 17.5 degrees

3.8 Rigid Body Critical Speeds

A knowledge of the critical speeds is important so that they do not occur near the operating speed. The rigid body critical speeds of the gas bearing system were calculated from the equivalent mechanical system shown in Figure 14. The equations of motion of the system for undamped free vibrations are:

For translatory motion:

$$\left.\begin{aligned} M_r \ddot{x} + 2K_f x - 2K_f y &= 0 \\ M_s \ddot{y} + 2(K_f + K_s) y - 2K_f x &= 0 \end{aligned}\right\} \tag{5}$$

For conical motion:

$$\left.\begin{aligned} I_r \ddot{\theta} + 2K_f \ell_f^2 \theta - 2K_f \ell_f^2 \phi &= 0 \\ I_s \ddot{\phi} + 2(K_f \ell_f^2 + K_s \ell_s^2) \phi - 2K_f \ell_f^2 \theta &= 0 \end{aligned}\right\} \tag{6}$$

Note that the equations of motion are uncoupled; that is the translatory equations of motion do not contain θ and ϕ, and the conical equations of motion do not contain x and y. In this case, the system translatory and conical frequencies are independent of each other. Actually, the centers of gravity or rotor and shaft

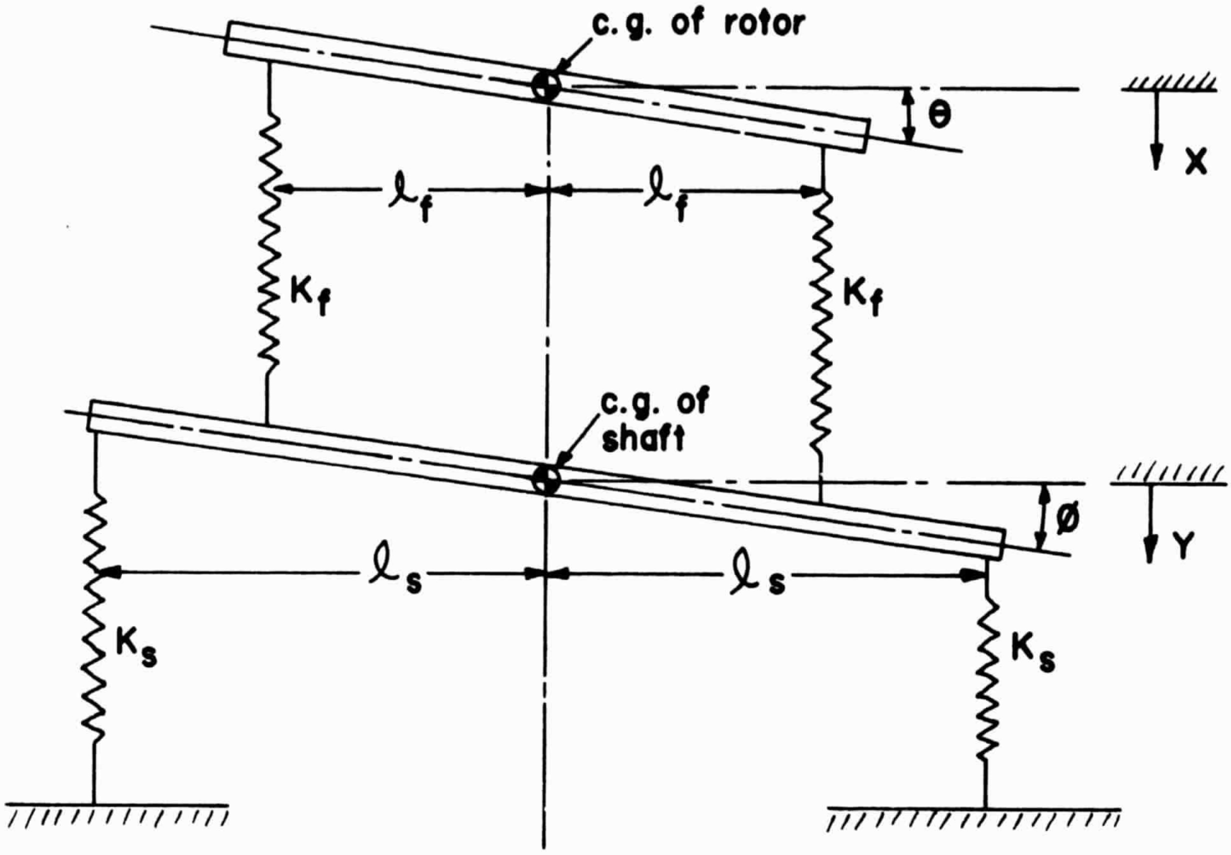

Figure 14

Equivalent Mechanical System of the Gas Bearing System.

Uncoupled, undamped free vibrations of a two-degree-of-freedom system.

do not exactly coincide and therefore some coupling between the modes of vibration does exist. A small amount of coupling will affect the modes of vibration but not the location of the critical speeds. Coupling is ignored in order to simplify the analysis.

The frequency equation of equations (5) and (6) is:

$$\omega = \left[\frac{A}{2} \pm \frac{1}{2} \sqrt{A^2 - 4B} \right]^{\frac{1}{2}} \tag{7}$$

where

For translatory motion:

$$A = \frac{2\,[M_r(K_f + K_s) + M_s K_f]}{M_r M_s} \qquad B = \frac{4\,K_f K_s}{M_r\,M_s}$$

For conical motion:

$$A = \frac{2\,[I_r\,(K_f\,\ell_f^2 + K_s\,\ell_s^2) + I_s\,K_f\,\ell_f^2]}{I_r\,I_s}$$

$$B = \frac{4K_f\,K_s\,(\ell_f\,\ell_s)^2}{I_r\,I_s}$$

where:

M_r = mass of the rotor = 0.02752 lb-sec^2/in.

M_s = mass of the shaft = 0.004517 lb-sec^2/in.

I_r = (transverse-polar) moment of inertia of the rotor = 0.2487 lb-sec^2-in.

I_s = transverse moment of inertia of the shaft = 0.08718 lb-sec^2-in.

K_f = hydrodynamic film stiffness, lb/in.(see Figure 13)

K_s = flexible support stiffness = 2,500 lb/in.

ℓ_f = 4.844 in. (see Figure 14)

ℓ_s = 6.4 in. (see Figure 14)

The rigid body critical speeds calculated from equation (7) are plotted in Figure 15. As it can be seen, the lower critical speeds remain constant with respect to rotor speed. This is because the hydrodynamic film stiffness has little effect on the lower critical speeds. Also, the conical speeds are above the translatory since the journal bearings are placed outside the wheels.

3.9 Dynamic Balancing of the Rotor

The rotor was dynamically balanced on its own shaft while supported on hydrostatic air bearings. As machined, the rotor was not too much out of balance, and therefore, only small amounts of material were removed with a hand grinder from the simulated compressor and turbine wheels. The rotor was balanced to the unbalance limit of the machine (less than 1 unbalance units) with the meter in its most sensitive position. Provisions have been made to install a small screw at the center of gravity of the rotor which will produce an unbalance of 0.0054 ounce-inches above the residual unbalance.

3.10 Simulator Instrumentation

The simulator was instrumented to measure, observe, or record the following:

a. Rotor speed

b. Lissajous patterns, frequency, and amplitude of rotor motion at each journal bearing relative to the shaft.

c. Lissajous patterns, frequency, and amplitude of shaft motion at each end relative to the frame.

d. Frequency and amplitude of axial rotor motions relative to the thrust stator.

e. Film thickness on both sides of the thrust bearing.

f. Total air flow to the bearings under hydrostatic conditions.

g. Inlet air pressures to the bearings under hydrostatic conditions.

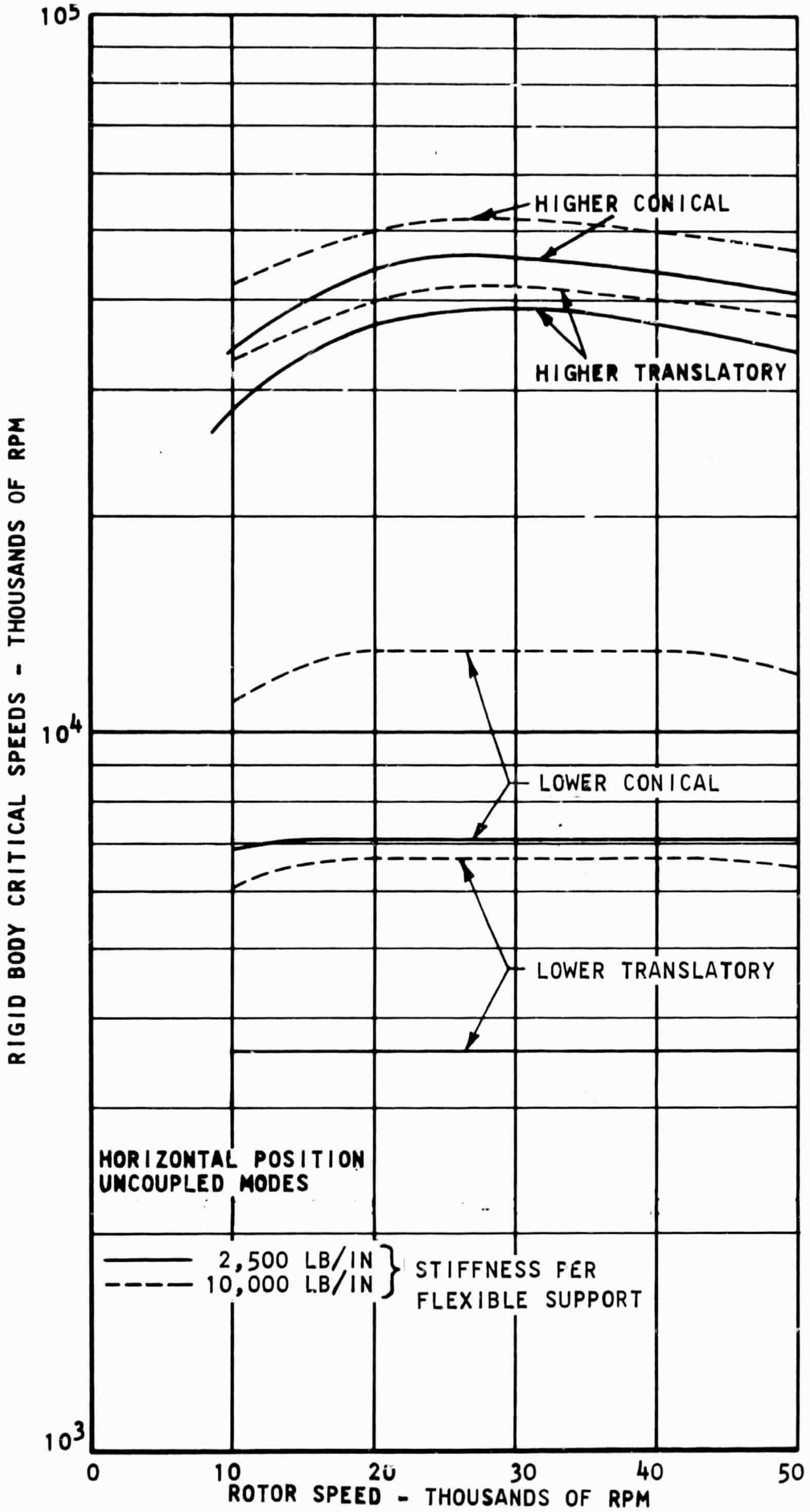

Fig. 15 - Rigid Body Critical Speeds vs. Rotor Speed

A total of 14 capacitors and capacitance probes were incorporated in the simulator to measure the dynamic performance of the bearing system. The Wayne Kerr (Model B731B Vibration Meter) capacitance system was used to measure the shaft motion relative to the frame. In this system, two probes (90° apart) were located at each end of the shaft. The rotor motion relative to the shaft was measured with the Decker (Model 951 Delta Unit) capacitance system. In this system, four capacitors were embedded at each journal surface, and one capacitor at each face of the thrust stator. Attempts to coat with chrome oxide the epoxy which insulates the brass capacitor from the shaft were not successful. This is shown in Figure 16 where a test steel plate with two epoxy (Armstrong C-4) insulated brass capacitors was chrome oxide coated and ground. As can be seen, the chrome oxide did not adhere to the epoxy, and therefore a recess of approximately 3 mils deep was formed all around the epoxy. Also, small pieces of overhanging chrome oxide could be easily dislodged. As a result of this, the shaft and thrust stator bearing surfaces were chrome oxide coated with all capacitor holes drilled but without the capacitors. The capacitors were then inserted complete with wires into their mating parts with epoxy (Armstrong A-12) adhesive. Finally, the bare capacitors, epoxy, and chrome oxide were ground flush at the surface.

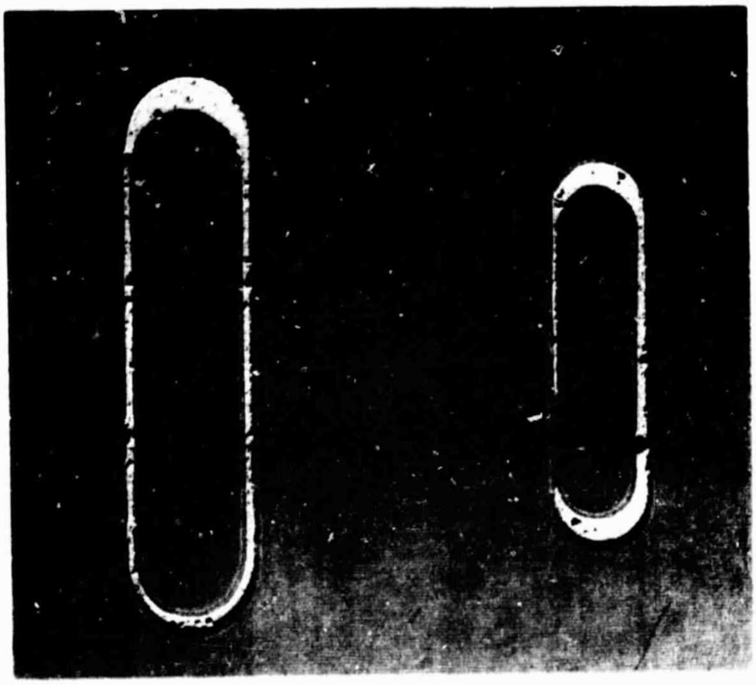

Fig. 16 - Test Steel Plate With Epoxy Insulated Brass Capacitors. Plate and Capacitors are Chrome Oxide Coated and Ground. Coating Did Not Adhere to Epoxy.

4.0 SIMULATOR SHAFT-ROTOR ASSEMBLY

The shaft and rotor parts were first ultrasonically cleaned and then the rotor was assembled on the shaft. The shaft was pressurized to check the floating ability of the rotor. The rotor was freely floating in the horizontal position at 35 psig, and in the vertical position at 26 psig. The oscilloscope bearing orbit traces showed a larger orbit for the compressor end bearing and a smaller orbit for the turbine end bearing as shown in Figure 17. This is expected to be due to the misalignment between the two journal bearings. Also, the hydrostatic (80 psig) lift of the rotor at each end was measured by a precision dial indicator (with 0.000010 inch graduations). The lift of the rotor at the compressor end was from 0.45 mils to 0.65 mils, and at the turbine end from 0.45 mils to 0.55 mils as the rotor was rotated 360 degrees. This again is an indication of misalignment. The radial clearance at each journal bearing was 0.65 mils. Whether this misalignment is caused due to manufacturing inaccuracy or due to the disassembly and re-assembly of the rotor was not determined. The rotor bore was ground but not lapped while the five rotor members were bolted together. The rotor had to be disassembled in order to be reassembled on the shaft. The tests were conducted with this inherent journal bearing misalignment.

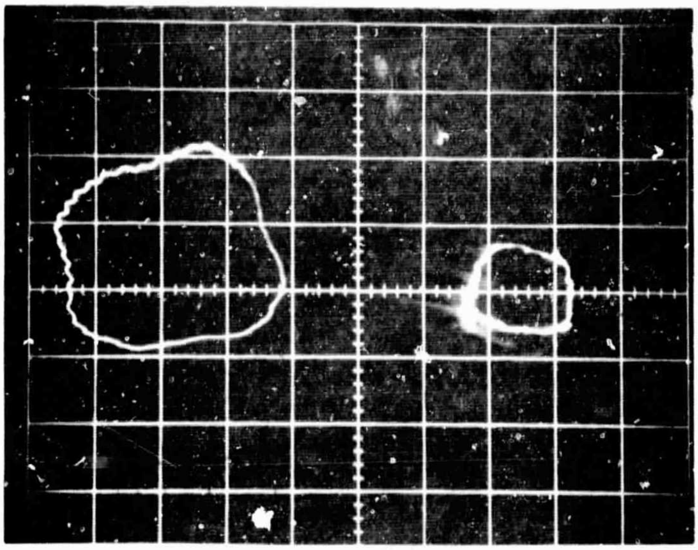

Zero Film

Zero Film

40 psig Supply Pressure

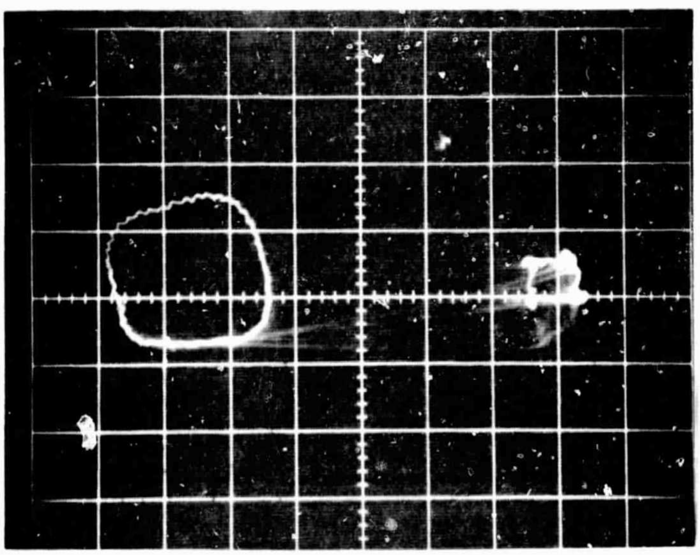

Zero Film

Zero Film

80 psig Supply Pressure

Large Orbit: Compr. End Brg. - Small Orbit: Turb. End Brg.

The zero film line is mainly for the turbine end journal bearing.

Oscilloscope Calibration: Vertical and Horizontal $\approx$ 0.2 mils/major division

Fig. 17 - Oscilloscope Traces of Misaligned Journal Bearing Orbits. Rotor Speed 900 rpm. Rotor Vertical

5.0 STATIC TESTS

Static tests were conducted in the vertical position to determine the following:

a. Flexible support stiffness
b. Dashpot damping
c. Hydrostatic journal bearing stiffness at four (4) inlet pressures from 55 to 115 psia
d. Hydrostatic thrust bearing stiffness at four (4) inlet pressures from 55 to 115 psia
e. Bearing flow rates at inlet pressures from 55 psia to 115 psia

The static tests are discussed in the following sections. Figure 18 is a view of the simulator assembly in the vertical position on the test bench during the static tests.

5.1 Flexible Support Stiffness

The flexible support ends were mounted in DU non-lubricated sleeve bearings as shown in Figure 2. In case of seizure, the shaft will rotate with the rotor, thus reducing the damage to the bearing surfaces. The flexible supports were designed to have a stiffness of approximately 9,000 lb/in. (per support) for end condition between clamped and simply supported. However, there were no provisions to vary their stiffness. Dynamic tests indicated lower stiffness was needed to increase the journal bearing threshold of instability. This was done by replacing the DU bearings by rubber bushings. Measured data of load vs. deflection for the flexible supports mounted in DU and rubber bushings is given in Figures 19 and 20, respectively. Some variation in the support stiffness is caused due to misalignment in the dashpots.

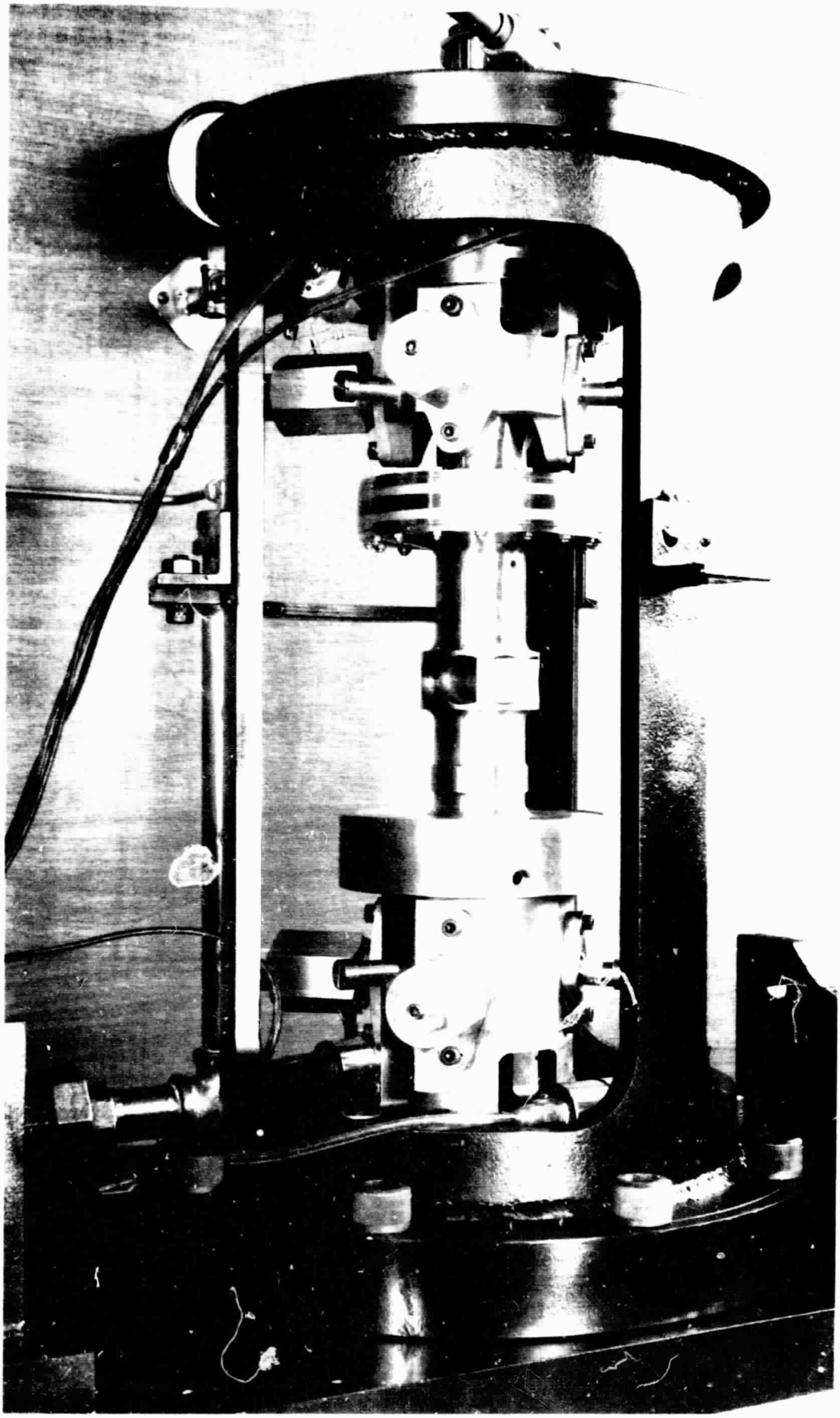

Fig. 18 - View of Simulator Assembly on Test Bench
(Vertical Position, Burning End Down)

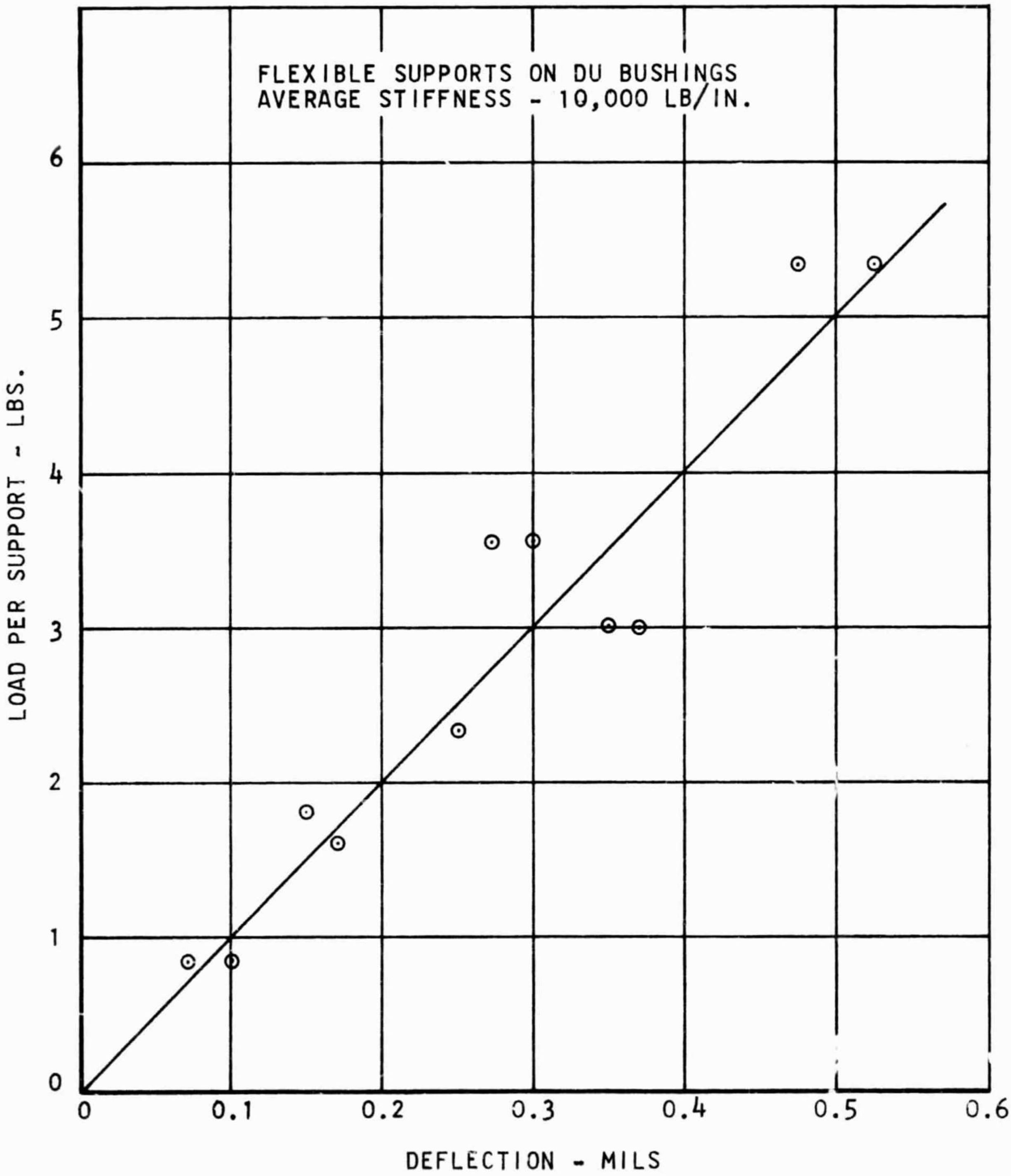

Fig. 19 - Measured Load vs. Deflection Curve of the Flexible Supports Supported by DU Bushings

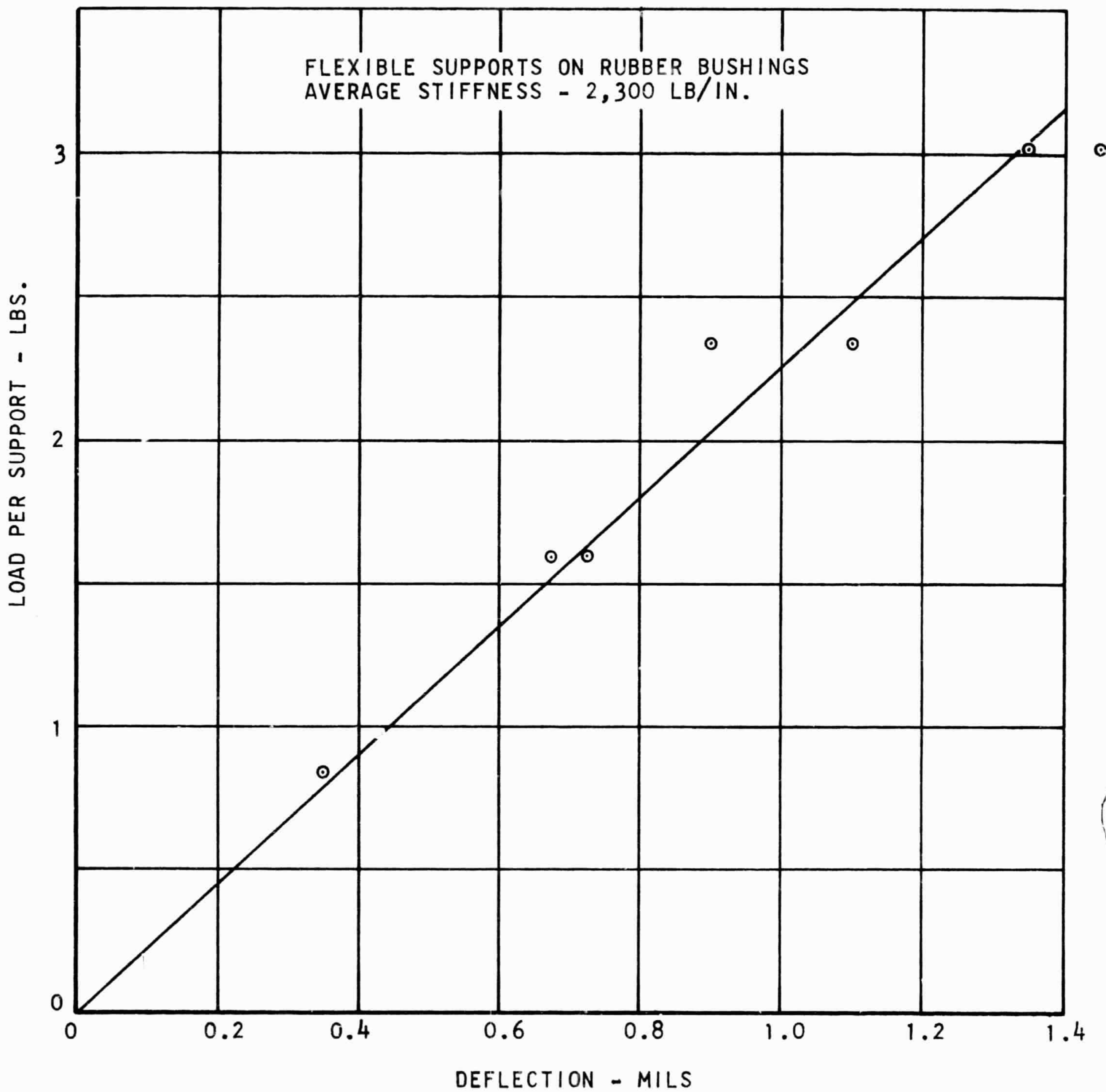

Fig. 20 - Measured Load vs. Deflection Curve of the Flexible Supports Supported by Rubber Bushings

5.2 Dashpot Damping

To measure the parameters for calculating the dashpot damping coefficients the tester shown in Figure 21 was used. The shaft shown in this figure has approximately the same mass as that of the simulator. The dashpot spindle (Item 17 in Figure 2) was fastened at the center of the shaft by a set screw. The dashpot contains silicone fluid with a viscosity of 30,000 cs. (4.17×10^{-3} lb-sec/in^2). A steel ball of 1-inch in diameter was swung against the center of the shaft setting the shaft into vibration. The signal from the capacitance probe was displayed on the oscilloscope and photographed by a Polaroid camera. In this manner, each of the four dashpots was tested with the adjusting nut (Item 14 in Figure 2) at five different positions. Typical oscilloscope traces of dashpot No. 2 are shown in Figure 22. The amplitude of vibration decays faster as the adjusting nut is screwed in. The damping coefficients were calculated from the measured amplitudes, decay time, and shaft mass by the equation:

$$B = \frac{2M_s}{t} \log_e \left(\frac{X_o}{X}\right) \tag{8}$$

where B = damping coefficient per dashpot, lb-sec/in.

M_s = mass of the shaft = 0.004522 lb-sec^2/in.

X_o = initial amplitude of vibration, cm

X = amplitude of vibration at a later time, cm

t = time, sec. [the time t is equal to the distance (cm) over which the amplitude decays from X_o to X, multiplied by the sweep rate (sec/cm)].

Figure 23 is a comparison between the analytical, Equation (1), and the experimentally determined damping coefficients as a function of the overlapping distance. When the adjusting nut is 1-inch out, the overlapping distance is zero. When it is 1/8 of an inch out, the overlapping distance is

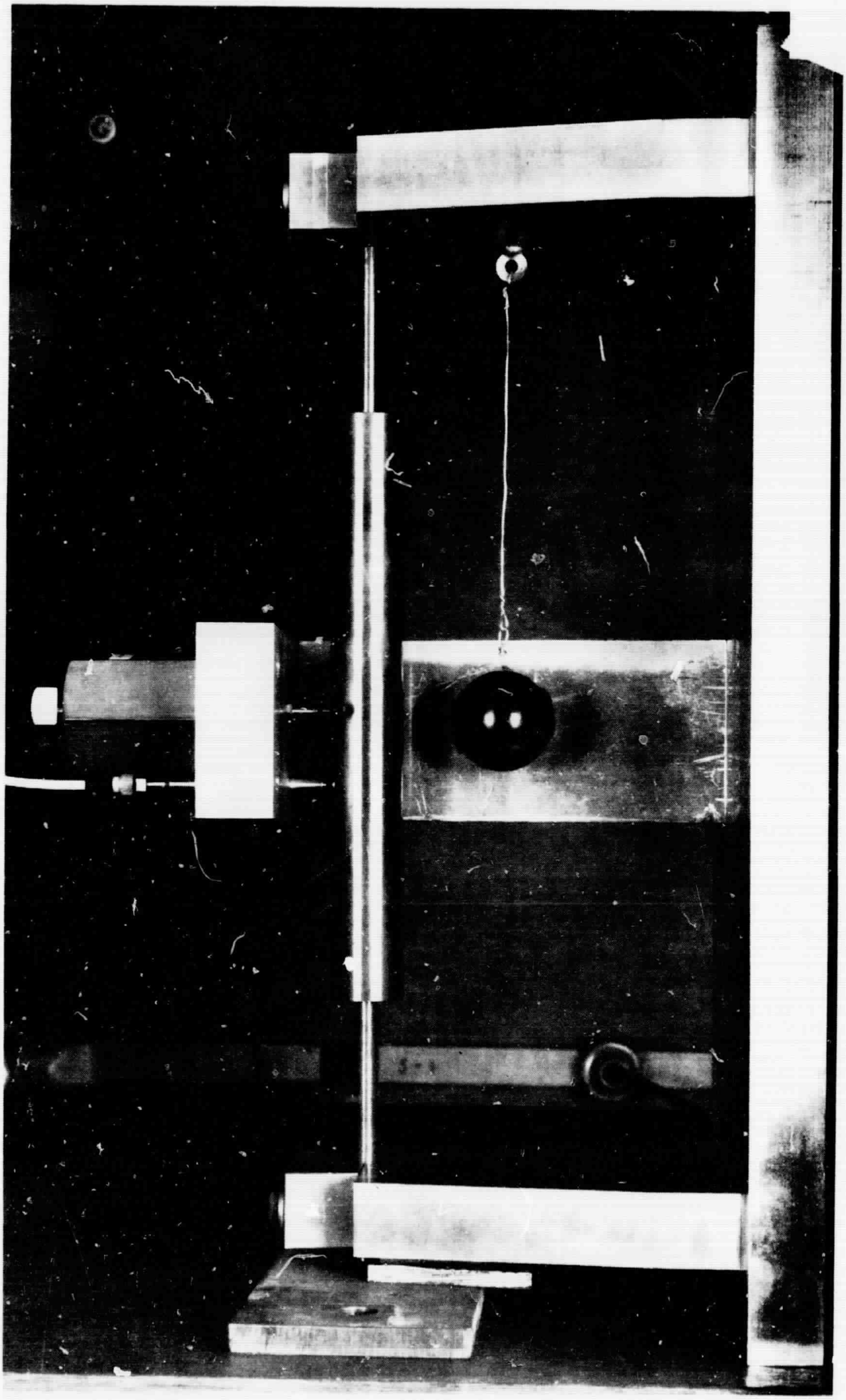

Fig. 21 - View of Viscous Damper Tester

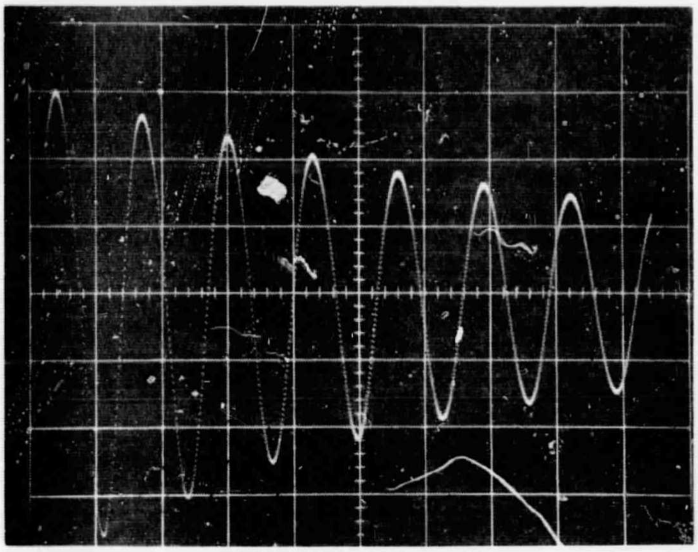

Adjusting Nut 1-Inch Out

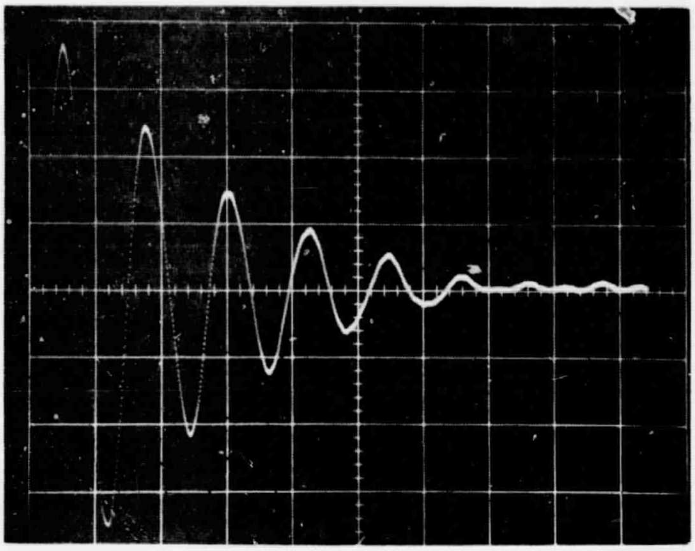

Adjusting Nut 3/4-Inch Out

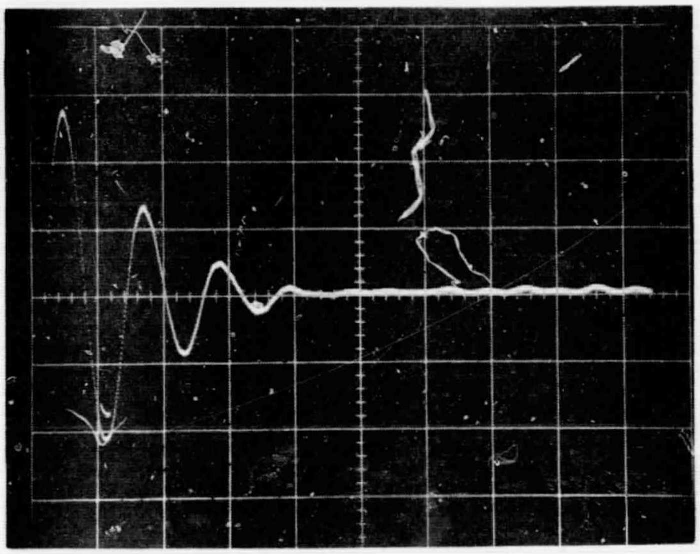

Adjusting Nut 1/2-Inch Out

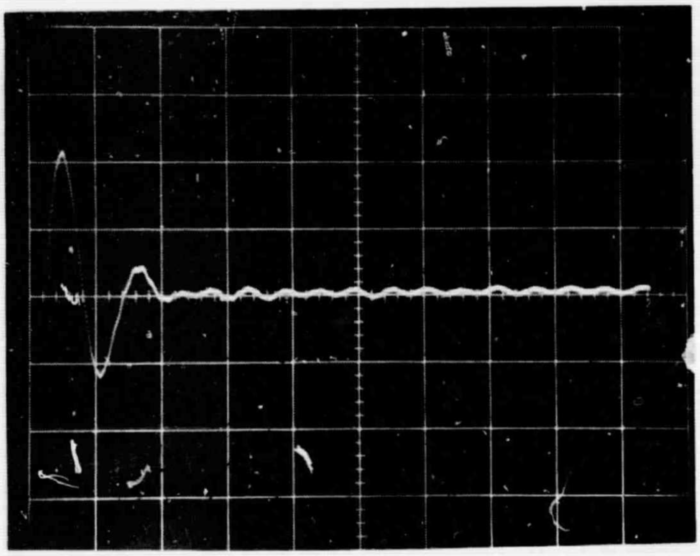

Adjusting Nut 1/8-Inch Out

Dashpot No. 2

Oscilloscope Calibration:

Vertical - 0.43 mils/major division
Horizontal - 2.0 milliseconds/major division

Fig. 22 - Oscilloscope Time - Base Traces of Damped Free Vibration of the Shaft Due to Viscous Damping.

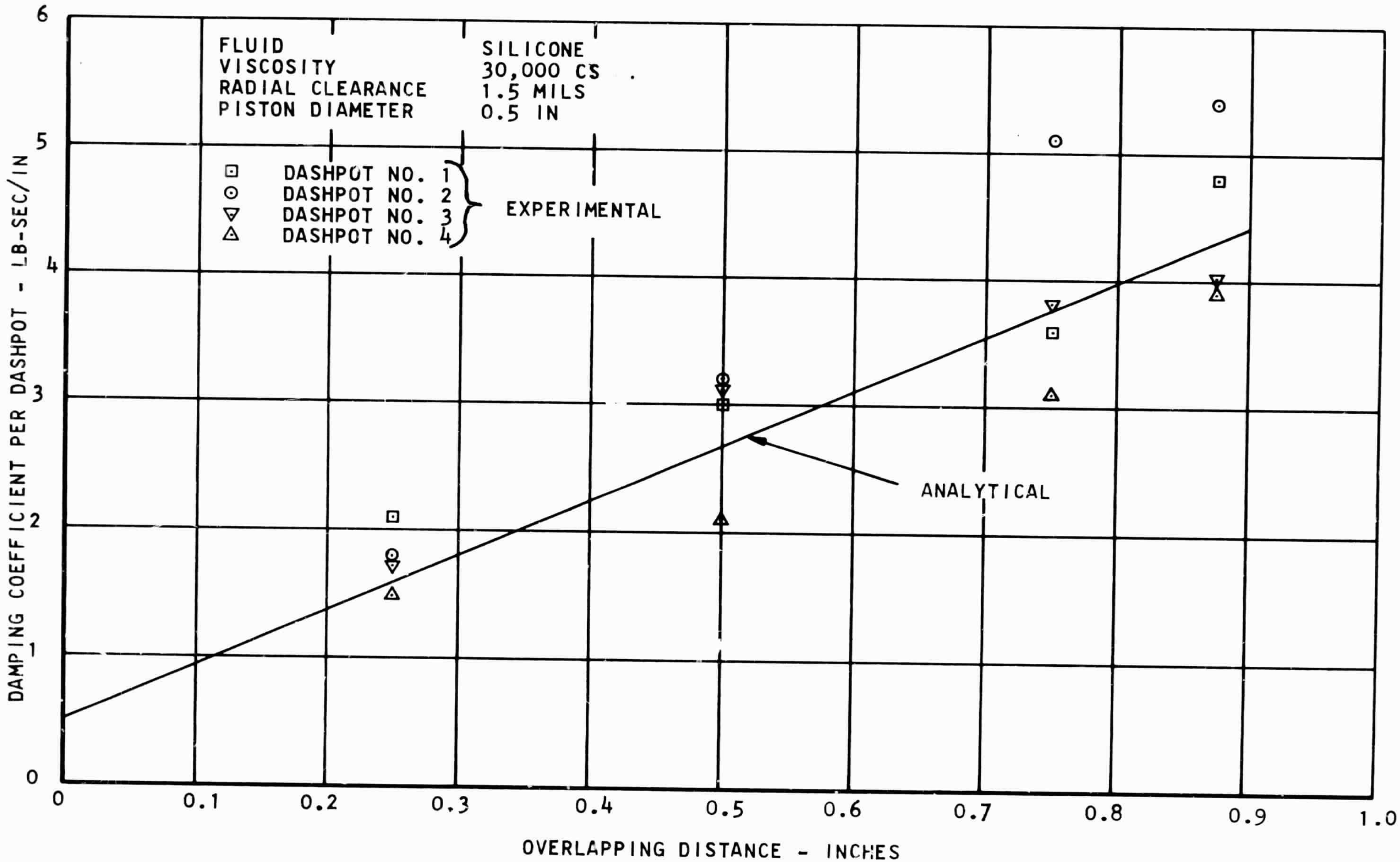

Fig. 23 - Analytical and Experimental Dashpot Damping Coefficients vs. Overlapping Distance

0.875 inches (max.). At zero overlapping distance the inherent dashpot damping is 0.5 lb-sec/in. The variation in the experimental data is most likely due to contact between stationary and moving parts of the dashpot as a result of misalignment and small clearances.

5.3 Journal Bearing Hydrostatic Film Stiffness

To determine experimentally the journal bearing hydrostatic film stiffness, the simulator shaft was rigidly fixed at each end by three 1/2-inch radial screws. This changed the bearing system from a two degree-of-freedom to a single degree-of-freedom system. The rotor was then set into a linear free damped vibration in the radial direction. The radial vibration of the rotor was displayed on the oscilloscope by means of capacitance pickups (Decker System) embedded at the bearing surface of the shaft. Photographs of oscilloscope traces showing the vibration of the rotor on the two journal bearings at four supply pressures (55 - 115 psia) are shown in Figure 24. Knowing the rotor mass and measuring (from the photographs) the vibrational frequency, the film stiffness was calculated by the simple equation:

$$f_n = \frac{1}{2\pi}\sqrt{\frac{2K}{M_r}} \tag{9}$$

where

f_n = natural frequency of vibration of the rotor, cycles/sec.

M_r = mass of the rotor = 0.02752 lb-sec^2/in.

K = film stiffness per journal bearing, lb/in.

Figure 25 is a comparison of analytical and experimental journal bearing film stiffness versus supply pressure. The analytical data was calculated from Reference 1.

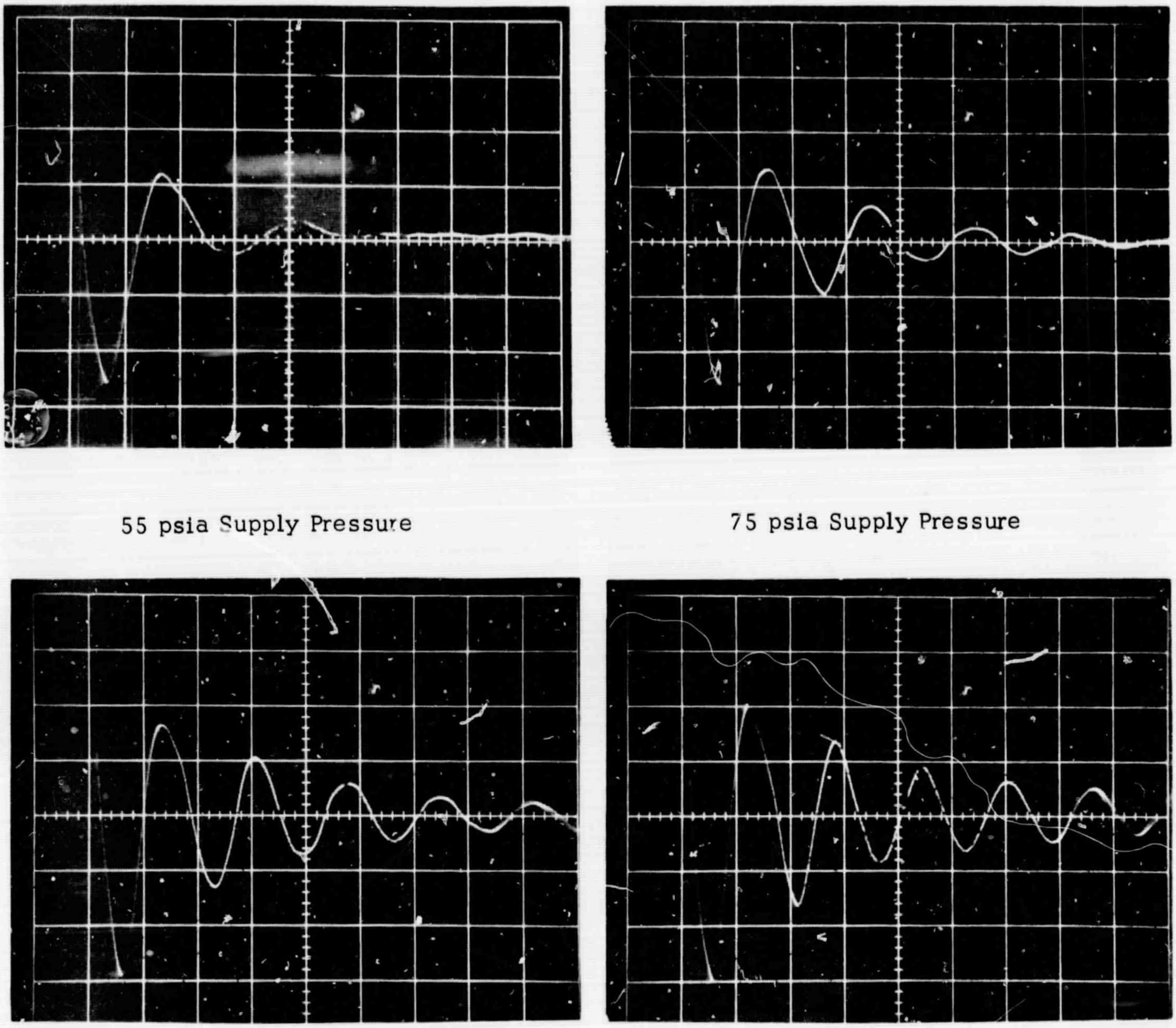

55 psia Supply Pressure

75 psia Supply Pressure

95 psia Supply Pressure

115 psia Supply Pressure

Oscilloscope Sweep Rate - 2.0 milliseconds/major division
Vertical Scale (Approx.) - 0.1 mils/major division

Fig. 24 - Oscilloscope Time - Base Traces of Damped Free Vibration of the Rotor on Two Hydrostatic Journal Bearings at Various Supply Pressures. Rotor Vertical.

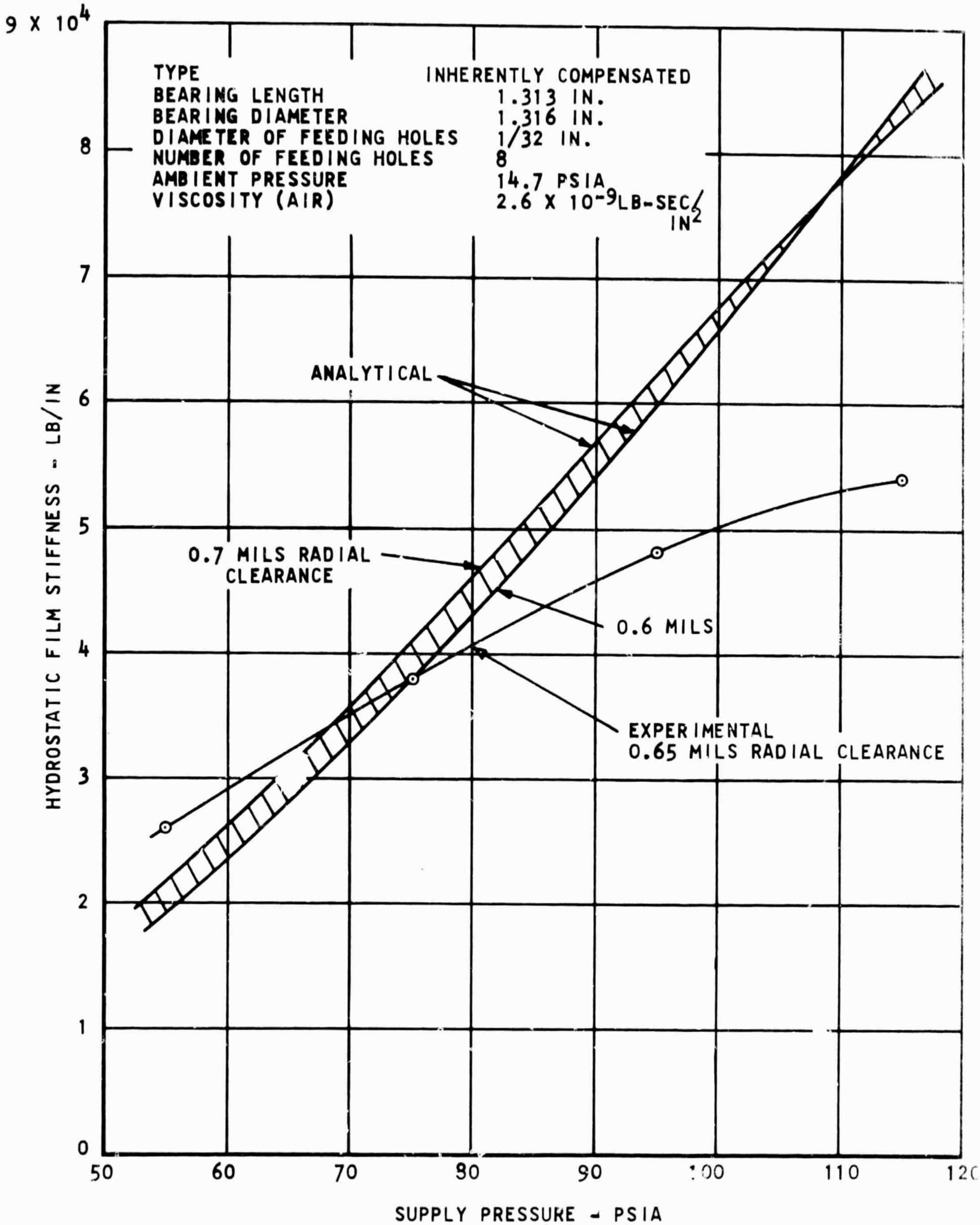

Fig. 25 - Analytical and Experimental Journal Bearing Hydrostatic Film Stiffness vs. Supply Pressure

5.4 Thrust Bearing Hydrostatic Film Stiffness

The thrust bearing hydrostatic film stiffness was determined experimentally, with the shaft in the vertical position, in a similar manner as that of the journal bearing. The rotor was set into a linear free damped vibration in the axial direction. Oscilloscope traces of vibration of the rotor relative to the thrust stator at four supply pressures (55-115 psia) are shown in Figure 26. A comparison of the analytical and experimental results is presented in Figure 27. As can be seen, the analytical values are much lower than the experimental, if the inside groove radius (1.379 inches) of the hydrodynamic bearing is used as the outside radius of the hydrostatic bearing. The correlation is better if the outside groove radius (2 inches) is used as the outside radius of the hydrostatic bearing.

5.5 Total Flow Rate To The Bearings

The air flow rate to the bearings was measured with a rotometer at four shaft cavity pressures (55, 75, 95, and 115 psia). Because of low air line pressure, the 115 psia test was conducted with nitrogen instead of air. A comparison of the calculated and measured flow rates versus supply pressure is shown in Figure 28. The discrepancy between the measured and calculated values may be due to the inertia effects which become important at large gaps and high supply pressures. Since 95% of the total flow rate is through the thrust bearing, the flow rate can be reduced by reducing the number of feeding holes. This will also reduce the thrust bearing load carrying capacity and stiffness which presently have a considerable safety factor.

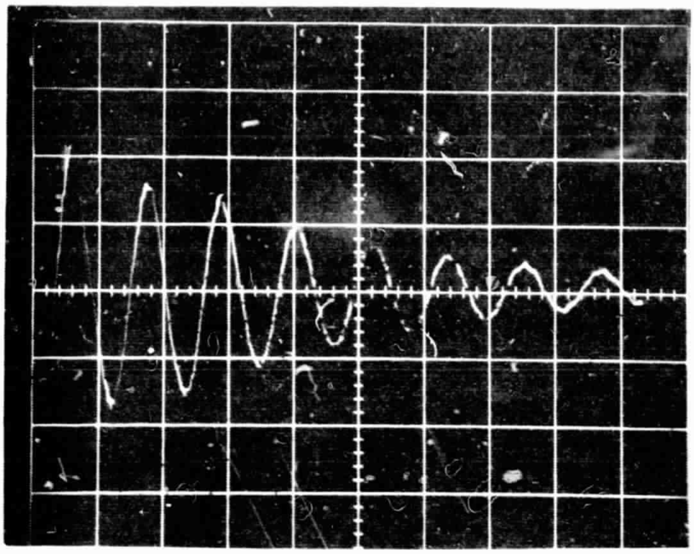

55 psia Supply Pressure

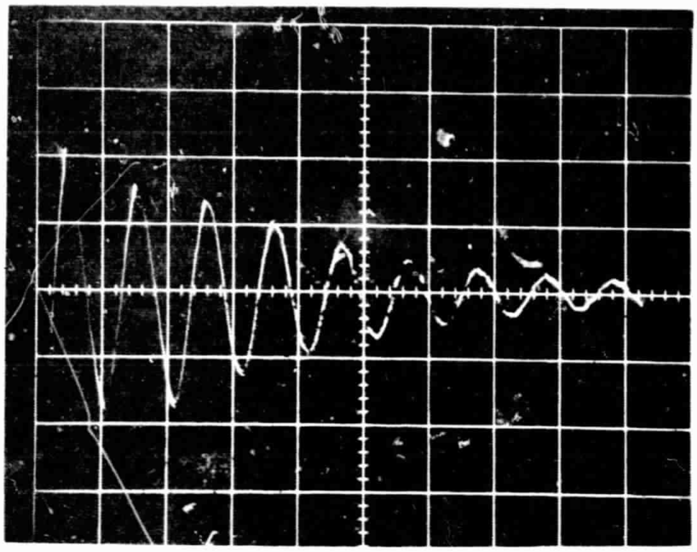

75 psia Supply Pressure

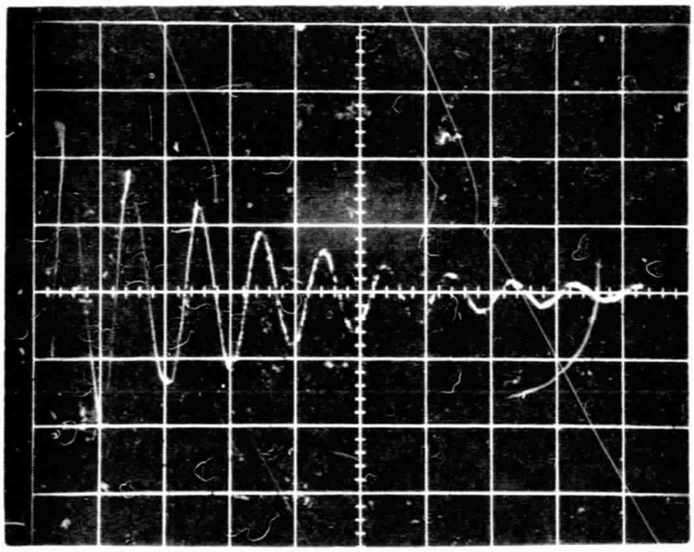

95 psia Supply Pressure

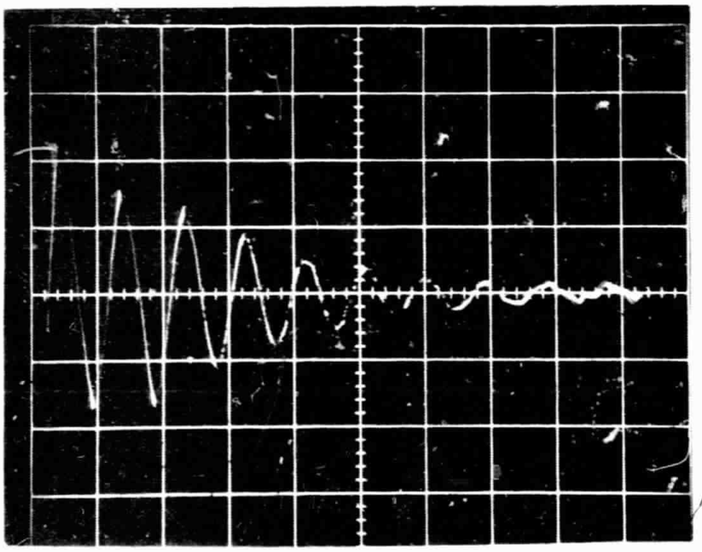

115 psia Supply Pressure

Oscilloscope Sweep Rate - 5.0 milliseconds/major division
Vertical Scale (approx.) - 0.5 mils/major division

Fig. 26 - Oscilloscope Time - Base Traces of Damped Free Vibration of the Rotor on Hydrostatic Double-Acting Thrust Bearing at Various Supply Pressures. Rotor Vertical.

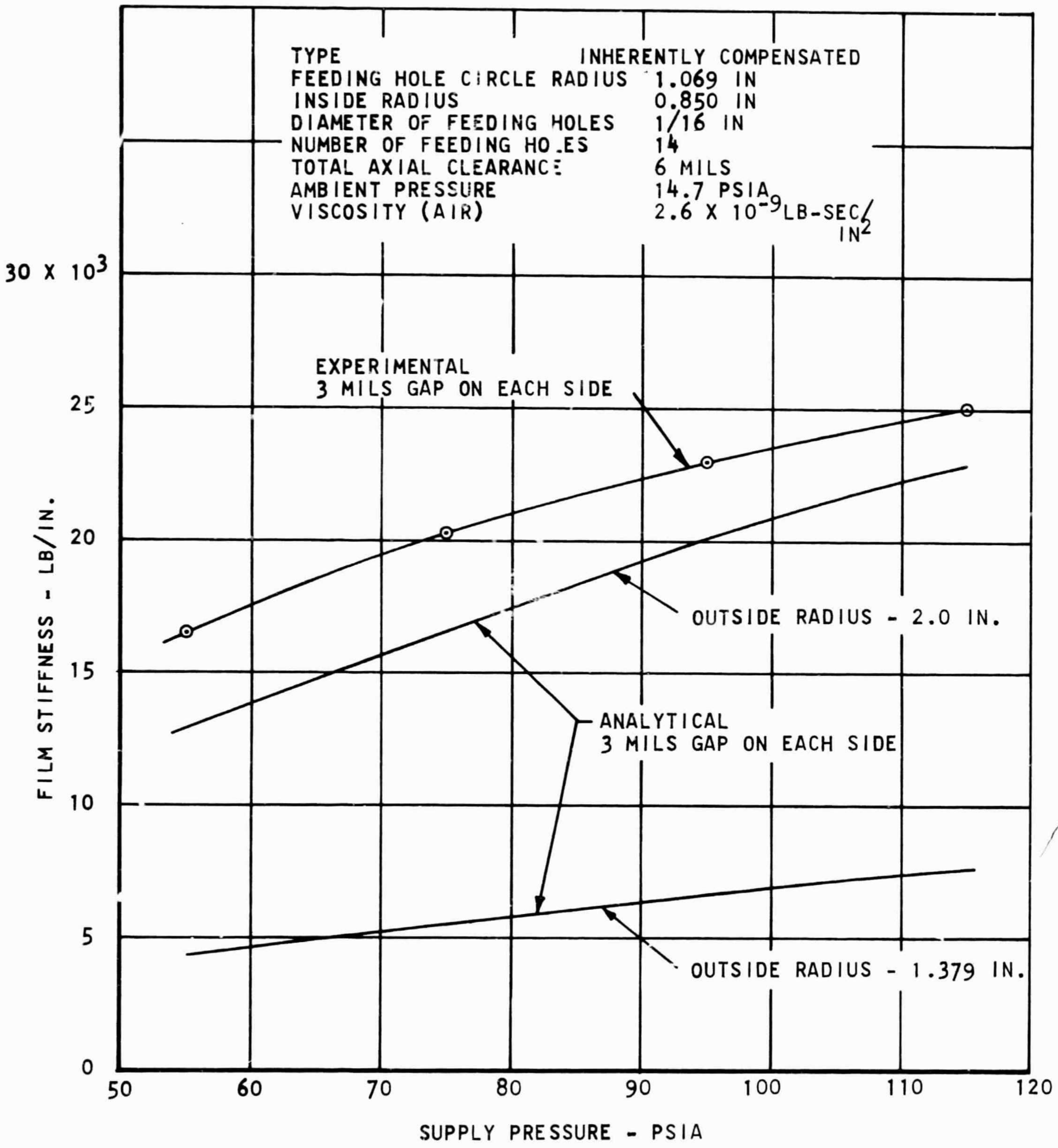

Fig. 27 - Analytical and Experimental Thrust Bearing Hydrostatic Film Stiffness vs. Supply Pressure

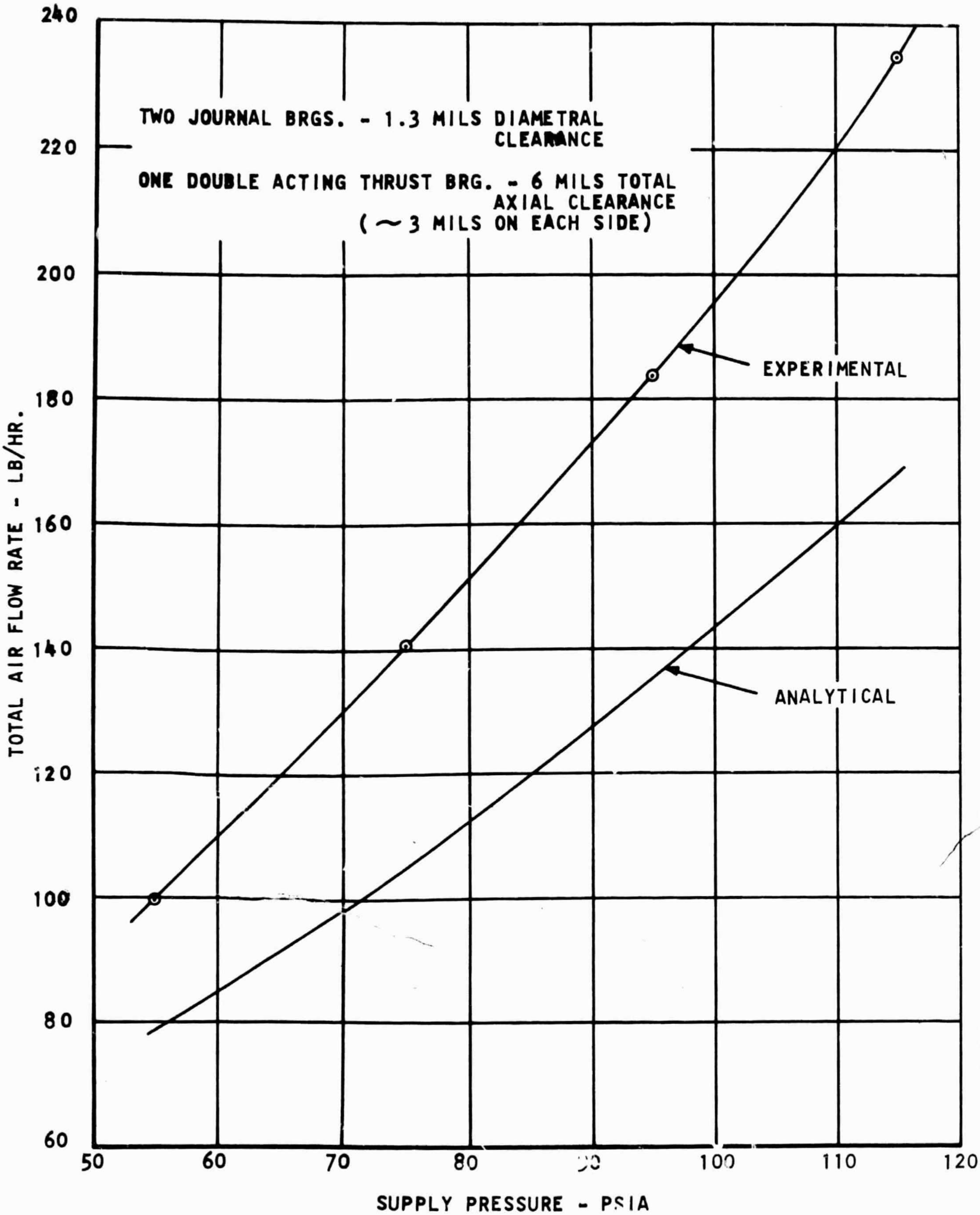

ig. 28 - Analytical and Experimental Total Air Flow Rate to the Bearings vs Supply Pressure

6.0 DYNAMIC TESTS

Dynamic tests were conducted in the horizontal and vertical positions under hydrostatic and hydrodynamic conditions. The effect of two support stiffnesses, 10,000 lb/in. and 2,300 lb/in. on the stability was investigated. Significantly higher journal bearing threshold of instability was observed with the lower support stiffness. Figure 29 is a view of the simulator with the read-out equipment.

6.1 Hydrostatic Tests In The Horizontal Position

In these tests, the threshold supply pressures at onset of journal bearing instability from 15,000 rpm to 30,000 rpm were determined. The flexible support stiffness during these tests was 10,000 lb/in. The rotor speed was held constant and the supply pressure was reduced until journal bearing instability was observed. Photographs of the test results are shown in Figure 30. As can be seen, due to high support stiffness the required threshold pressures are high.

Also, the rotor was operated hydrostatically to 39,000 rpm. As the speed was increased from 36,000 rpm to 39,000 rpm a high amplitude (~80% of the radial clearance) synchronous whirl was observed in both journal bearings. This could be either due to rotor mass shift unbalance or out-of-roundness of the rotor bearings which impresses a synchronous radial forcing function upon the rotor (Reference 3). It is not possible to determine which of the aforementioned synchronous forcing functions caused the high synchronous whirl amplitudes that have been observed.

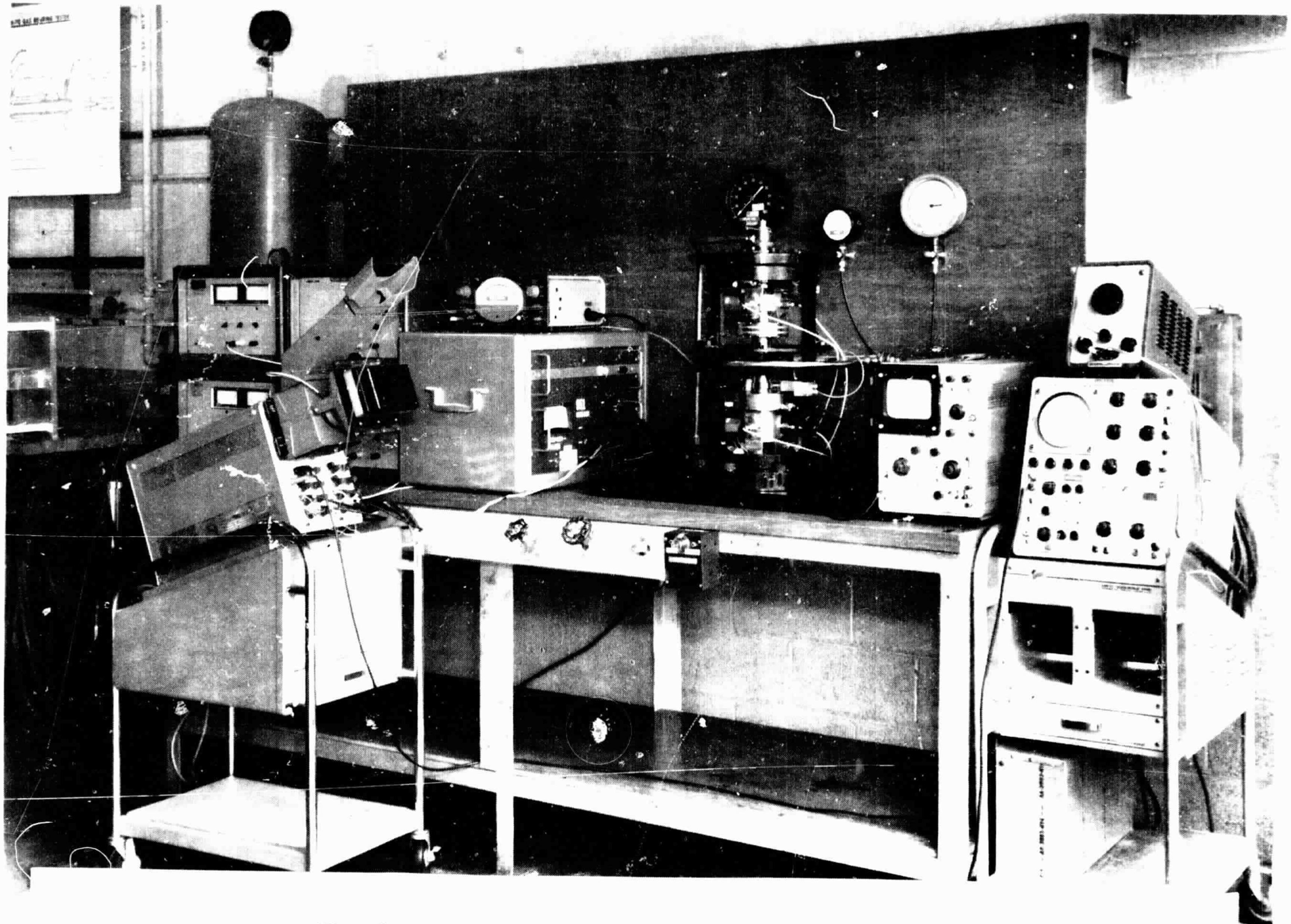

Fig. 29 - View Of Simulator In The Vertical Position
And Bearing Performance Read-Out Equipment

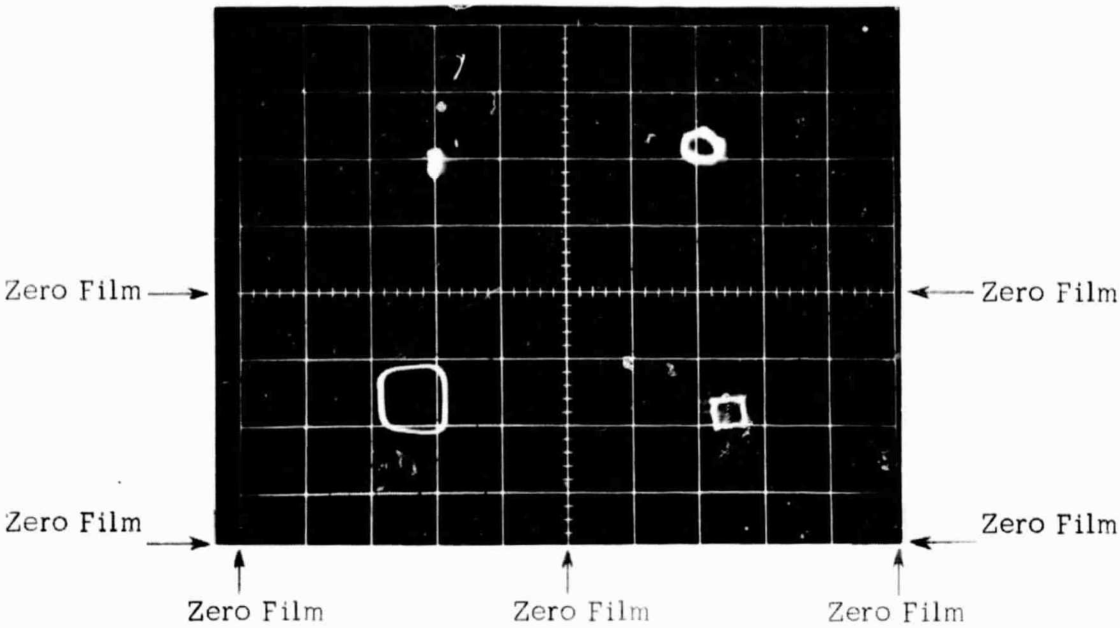

12,000 RPM - 80 PSIG

Top Left Orbit:	Compressor End Shaft (Journal) Motion
Top Right Orbit:	Turbine End Shaft (Journal) Motion
Bottom Left Orbit:	Compressor End Rotor (Bearing) Motion
Bottom Right Orbit:	Turbine End Rotor (Bearing) Motion

Oscilloscope Calibration: Vertical and Horizontal 0.5 Mils/Major Division
(For Shaft Orbits Only)

Rotor Horizontal
Hydrostatic Operation

Average Flexible Support Stiffness:	10,000 lb/in (per support)
Average Damping Coefficient:	3.9 lb-sec/in (per dashpot)

Fig. 30 - Oscilloscope Traces of Shaft Orbits Relative to the Frame and Rotor Orbits Relative to the Shaft - Rotor Horizontal, Hydrostatic Operation, Support Stiffness 10,000 lb/in.

(Fig. 30 Continued →)

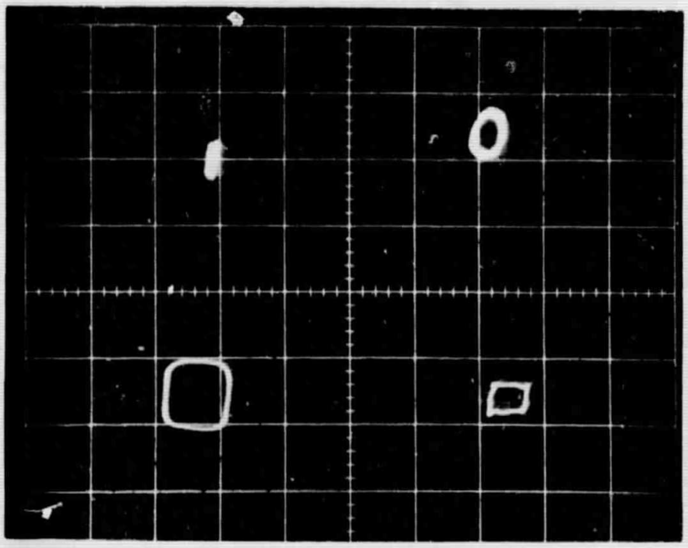

15,000 RPM - 80 psig

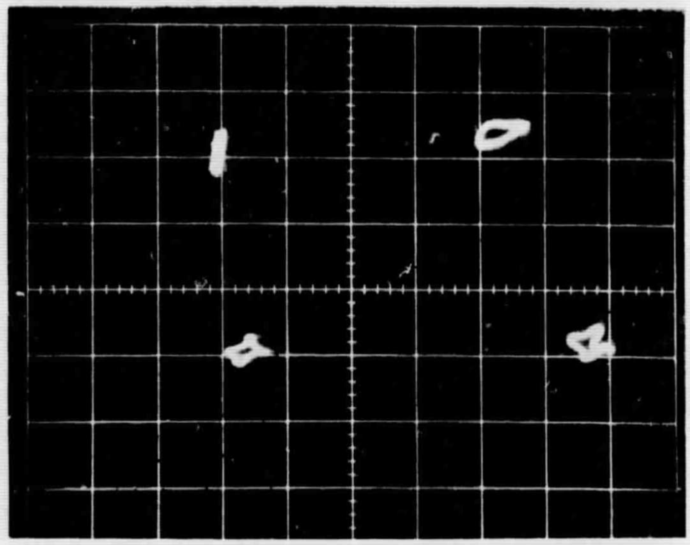

15,000 RPM - 10 psig

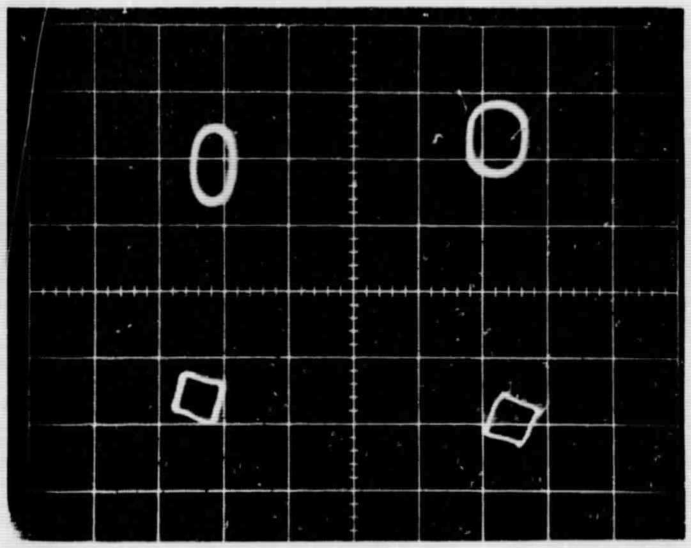

18,000 RPM - 80 psig

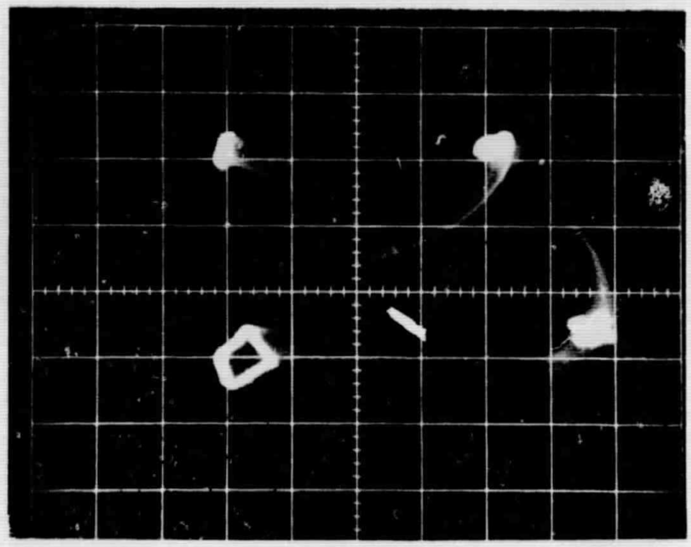

18,000 RPM - 10 psig

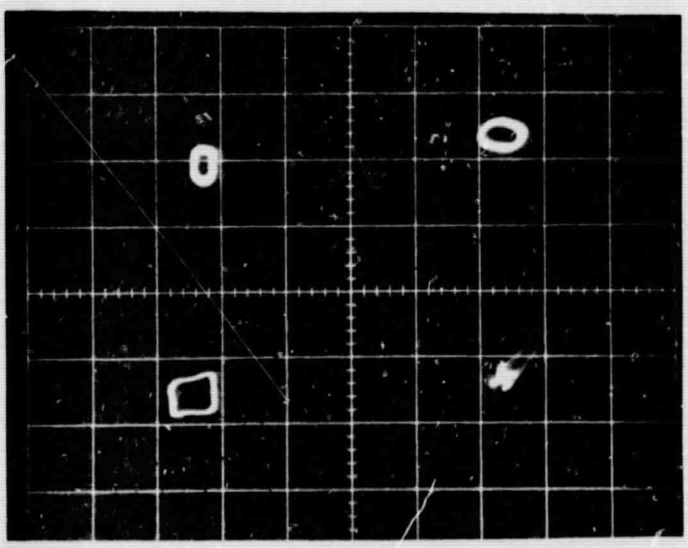

24,000 RPM - 80 psig

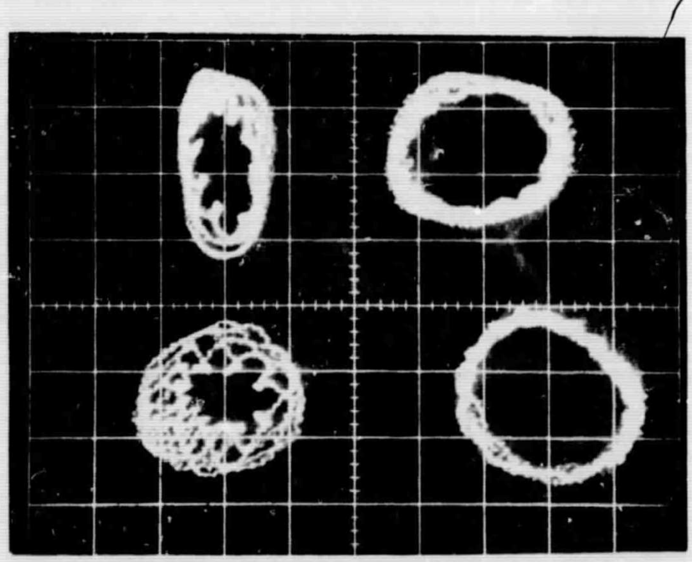

24,000 RPM - 26 psig

(Fig. 30 Continued →)

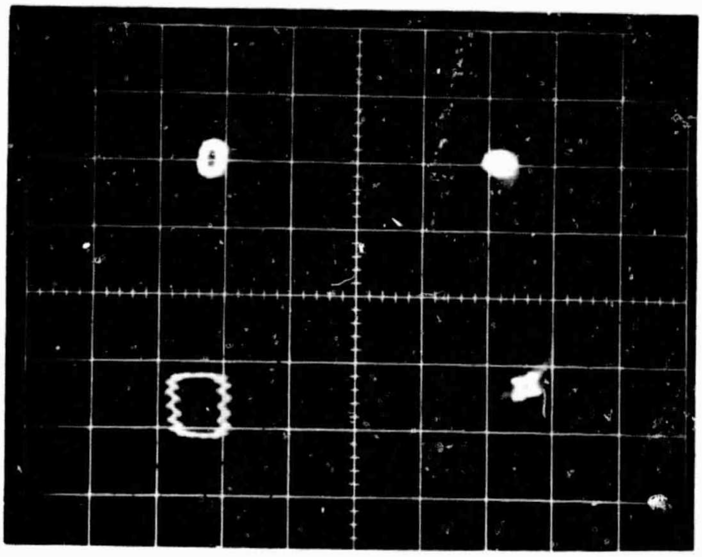

30,000 RPM - 77.5 PSIG

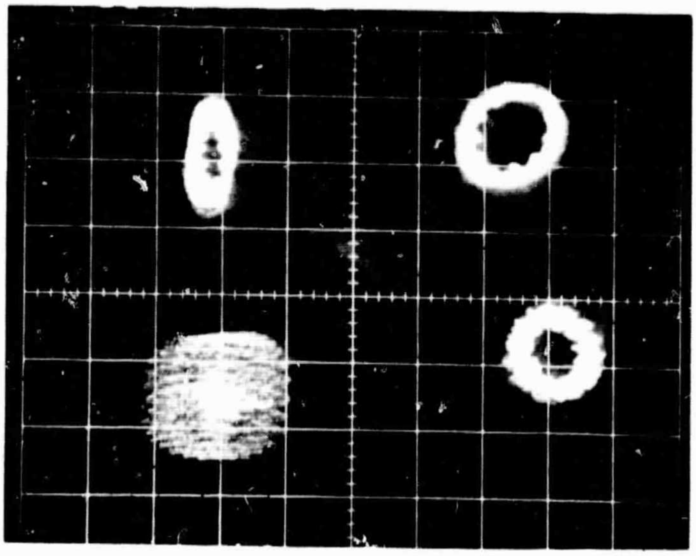

30,000 RPM - 30 PSIG

NOTE: The threshold pressure at 15,000 RPM is less than 10 PSIG.

(End of Fig. 30)

6.2 Hydrodynamic Tests In The Horizontal Position

Hydrodynamic tests in the horizontal position were conducted at three flexible support stiffnesses: 10,000 lb/in., 2,300 lb/in., and 1,900 lb/in.

With a flexible support stiffness of 10,000 lb/in., journal bearing hydrodynamic instability was encountered at 13,800 rpm. At this stiffness level, increasing or decreasing the amount of dashpot damping did not affect the threshold of instability. Photographs of the test results from 12,000 rpm to 15,000 rpm are shown in Figure 31.

The threshold of hydrodynamic instability was raised to 30,000 rpm by reducing the support stiffness to 2,300 lb/in. The reduction in stiffness was done by replacing the DU bearings by rubber bearings. Photographs of the test results from 3,000 rpm to 30,000 rpm are shown in Figure 32. At 27,000 rpm signs of journal bearing instability started to show up. At 30,000 rpm the amplitudes became quite large and therefore the test was stopped. At this speed there may have been partial contact between journal and sleeve, but no seizure occurred. During this test the thrust bearing was operating hydrostatically by sealing-off the journal bearing feeding holes and allowing a pressure of 10 psig within the shaft cavity.

In the previous tests it was observed that the amount of dashpot damping did not have a significant effect on the stability. The system may have had sufficient inherent damping due to the rubber bushings. Since the dashpots were contributing to some extent to the support stiffness due to their misalignment they were completely removed to reduce further the support stiffness. The measured average stiffness per support was 1,900 lb/in. (for deflections from 0.4 mils to 2 mils). With the dashpots removed, the rotor was brought hydrostatically to 12,000 rpm and then the supply pressure was completely shut off. Thrust and journal bearings were operating under complete hydrodynamic conditions. It was observed that when the journal bearing feeding holes are open the running clearance will decrease, indicating loss in load carrying capacity. The rotor was slowly accelerated to determine threshold speeds. With the feeding holes open the threshold speed was 36,000 rpm and with the feeding holes closed 21,000 rpm. Photographs of this test were not recorded.

The maximum attained speed of 36,000 rpm is three times higher than the fixed shaft threshold speed (12,000 rpm) of hydrodynamic instability.

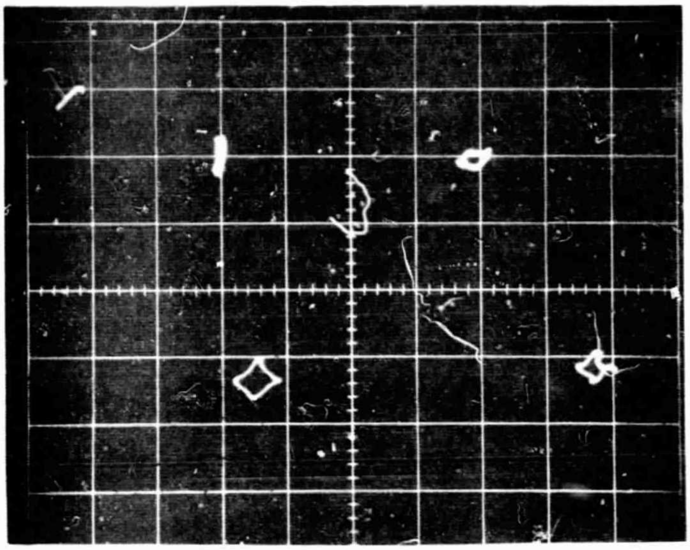

12,000 RPM

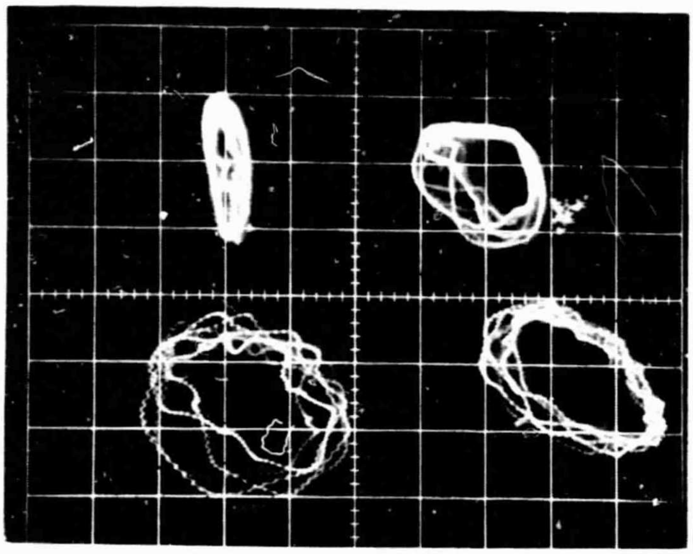

13,800 RPM

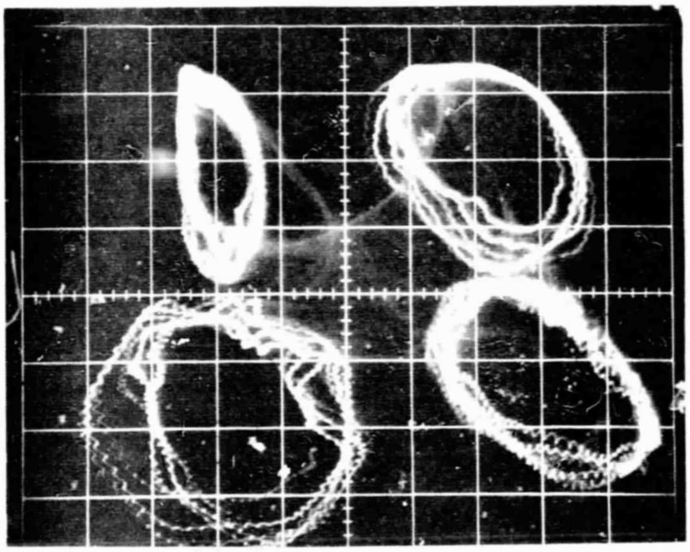

15,000 RPM

Oscilloscope calibration same as in Fig. 30.

Rotor Horizontal
Hydrodynamic Operation

Average Flexible Support Stiffness:	10,000 lb/in (per support)
Average Damping Coefficient:	3.9 lb-sec/in (per dashpot)

Fig. 31 - Oscilloscope Traces of Shaft Orbits Relative to the Frame and Rotor Orbits Relative to the Shaft - Rotor Horizontal, Hydrodynamic Operation, Support Stiffness 10,000 lb/in.

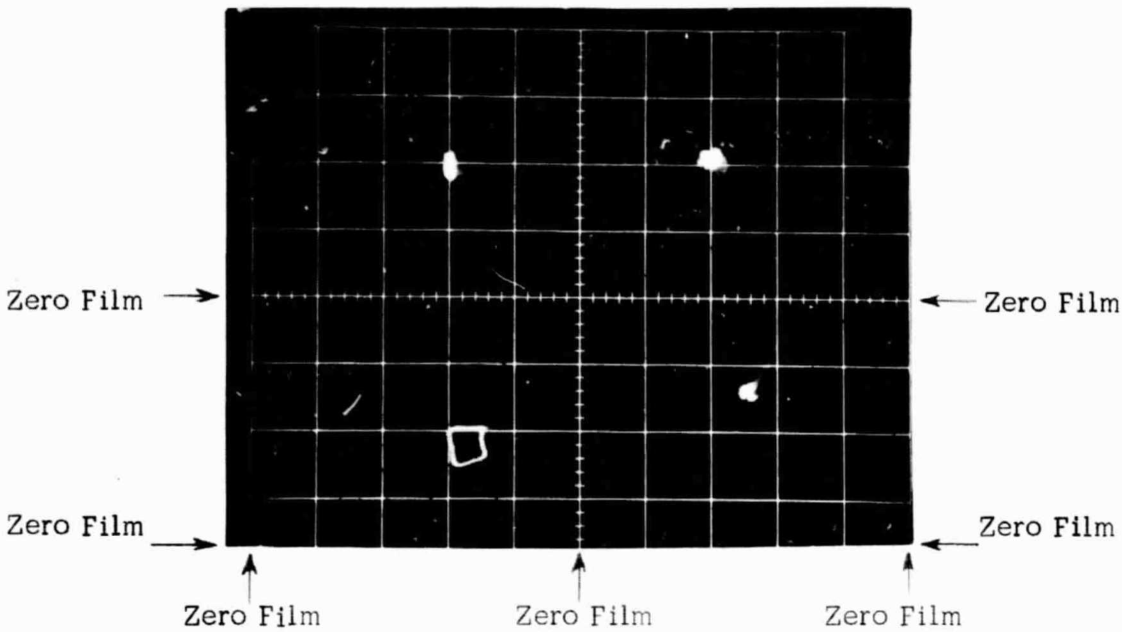

3,000 RPM

Top Left Orbit:	Compressor End Shaft (Journal) Motion
Top Right Orbit:	Turbine End Shaft (Journal) Motion
Bottom Left Orbit:	Compressor End Rotor (Bearing) Motion
Bottom Right Orbit:	Turbine End Rotor (Bearing) Motion

Oscilloscope Calibration: (For Shaft Orbits Only) Vertical and Horizontal 0.25 mils/major division

Rotor Horizontal
Hydrodynamic Operation
Average Flexible Support Stiffness: 2,300 lb/in (per support)
Average Damping Coefficient: 1.8 lb-sec/in (per dashpot)

Fig. 32 - Oscilloscope Traces of Shaft Orbits Relative to the Frame and Rotor Orbits Relative to the Shaft - Rotor Horizontal, Hydrodynamic Operation, Support Stiffness 2,300 lb/in.

(Fig. 32 Continued →)

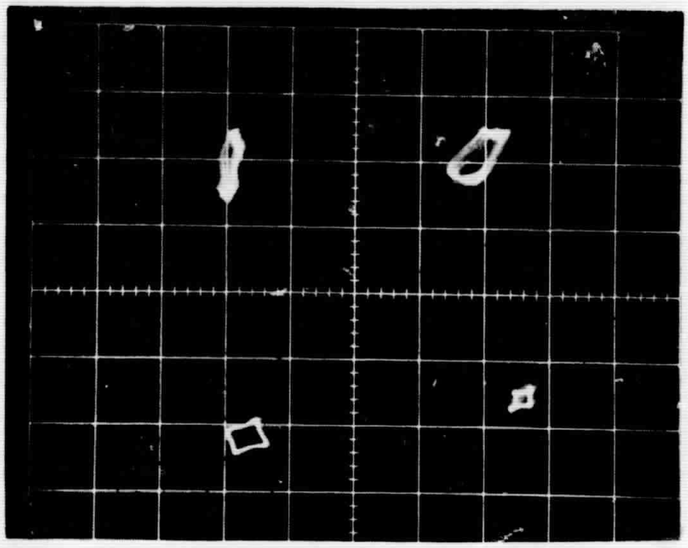

6,000 RPM

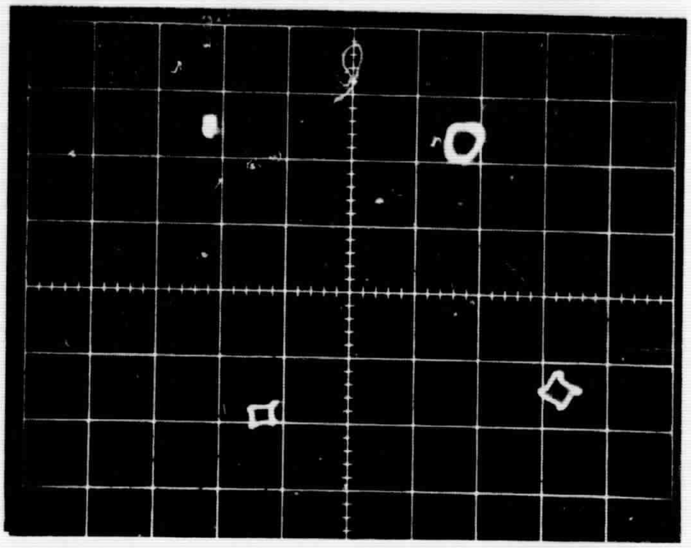

9,000 RPM

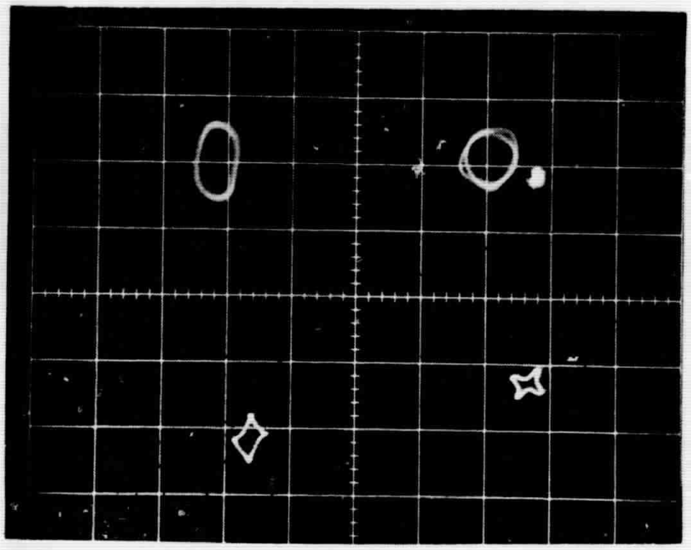

12,000 RPM

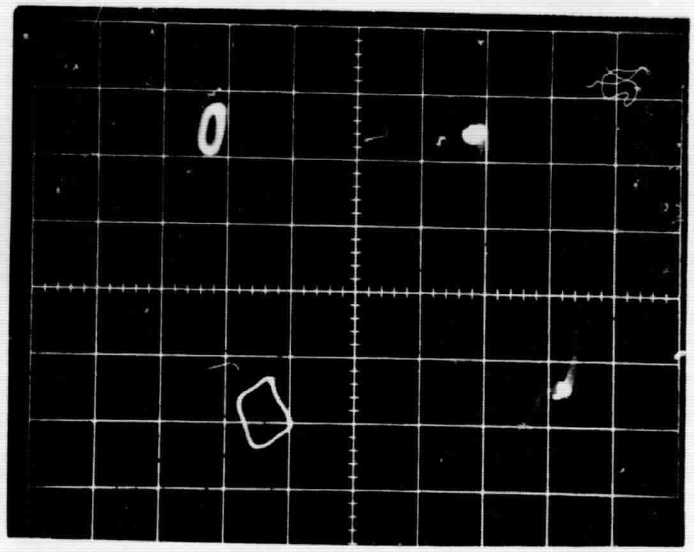

15,000 RPM

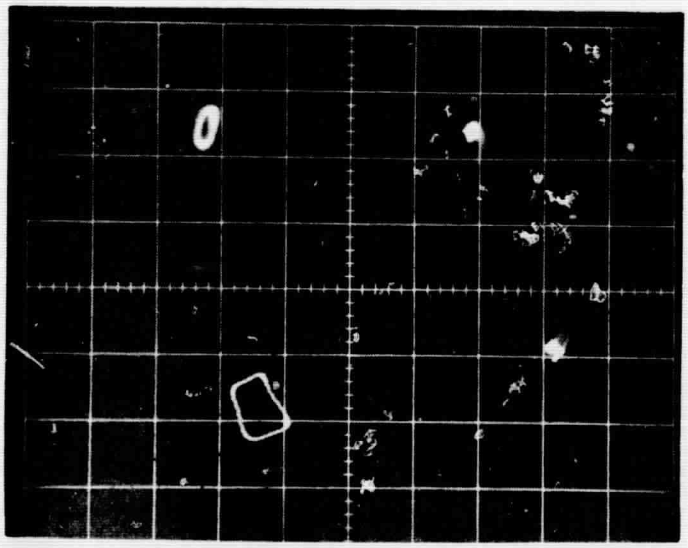

18,000 RPM

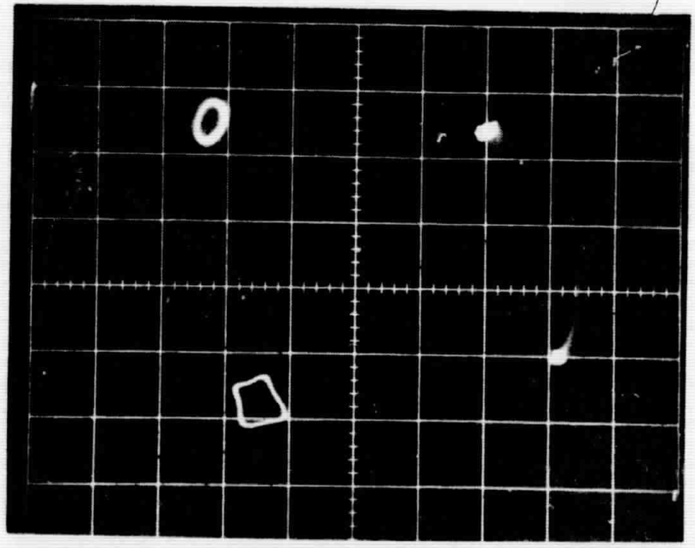

21,000 RPM

(Fig. 32 Continued →)

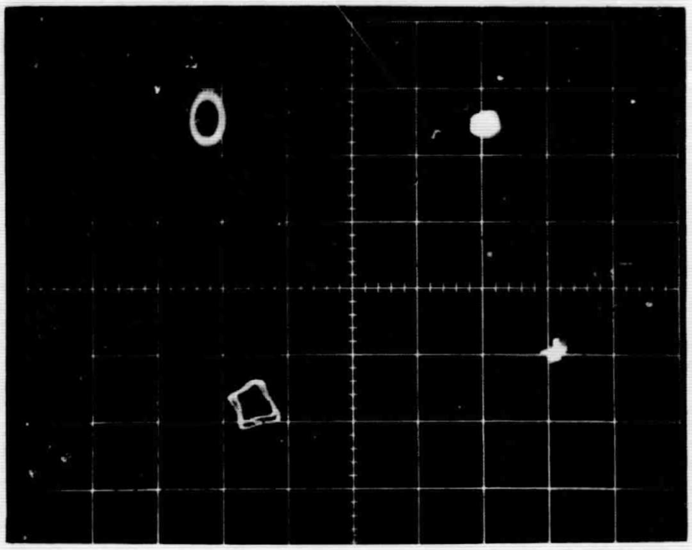

24,000 RPM

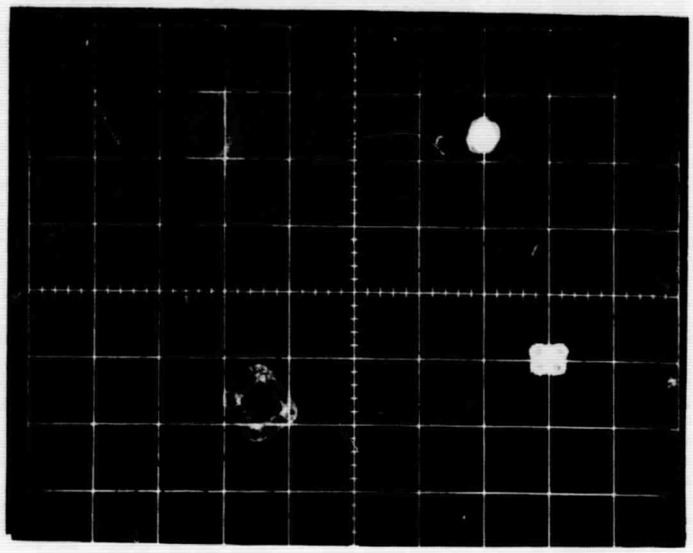

27,000 RPM

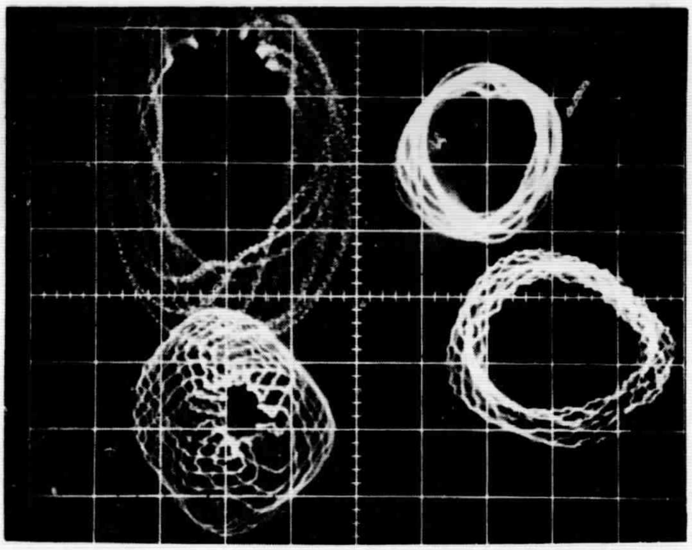

30,000 RPM

(End of Fig. 32)

6.3 Hydrostatic Tests In The Vertical Position

Hydrostatic tests in the vertical position were conducted at two flexible support stiffnesses: 10,000 lb/in. and 1,900 lb/in. In these tests the minimum supply pressure required for journal bearing stability was determined. As previously, the rotor speed was held constant and the supply pressure was reduced until journal bearing instability was observed.

Photographs of the test results with 10,000 lb/in. flexible support stiffness are shown in Figure 33. In this test, the flexible supports were mounted in DU bushings, and the average damping coefficient per dashpot was 3.9 lb-sec/in.

The test results with 1,900 lb/in. flexible support stiffness were as follows:

Speed, rpm	Threshold Pressure, psig
18,000	10
24,000	15
30,000	18

In this test, the flexible supports were mounted in rubber bushings and the dashpots were removed. Lowering the support stiffness from 10,000 lb/in. to 1,900 lb/in. reduced significantly the threshold supply pressures.

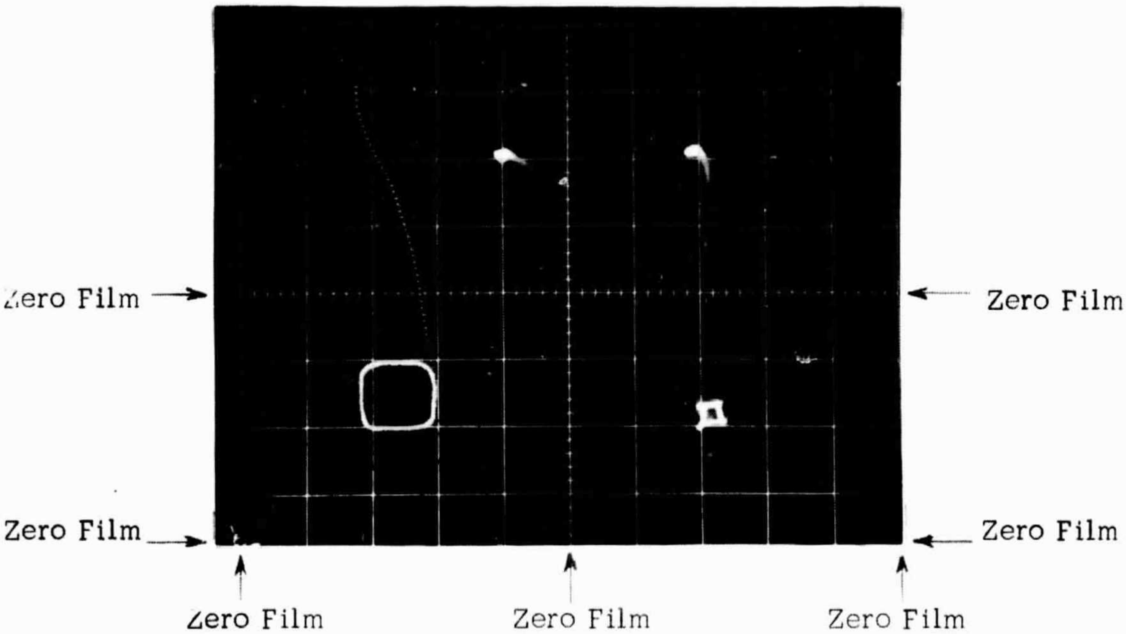

9,000 RPM - 80 PSIG

Top Left Orbit:	Compressor End Shaft (Journal) Motion
Top Right Orbit:	Turbine End Shaft (Journal) Motion
Bottom Left Orbit:	Compressor End Rotor (Bearing) Motion
Bottom Right Orbit:	Turbine End Rotor (Bearing) Motion

Oscilloscope Calibration: Vertical and Horizontal 0.5 mils/major division
(For Shaft Orbits Only)

Rotor Vertical
Hydrostatic Operation
Average Flexible Support Stiffness: 10,000 lb/in (per support)
Average Damping Coefficient: 3.9 lb-sec/in (per dashpot)

Fig. 33 - Oscilloscope Traces of Shaft Orbits Relative to the Frame and Rotor Orbits Relative to the Shaft - Rotor Vertical, Hydrostatic Operation, Support Stiffness 10,000 lb/in.

(Fig. 33 Continued →)

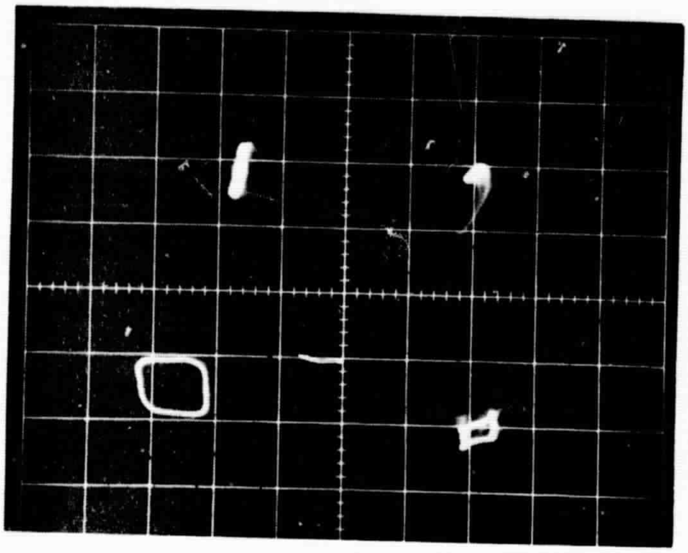

12,000 RPM - 80 psig

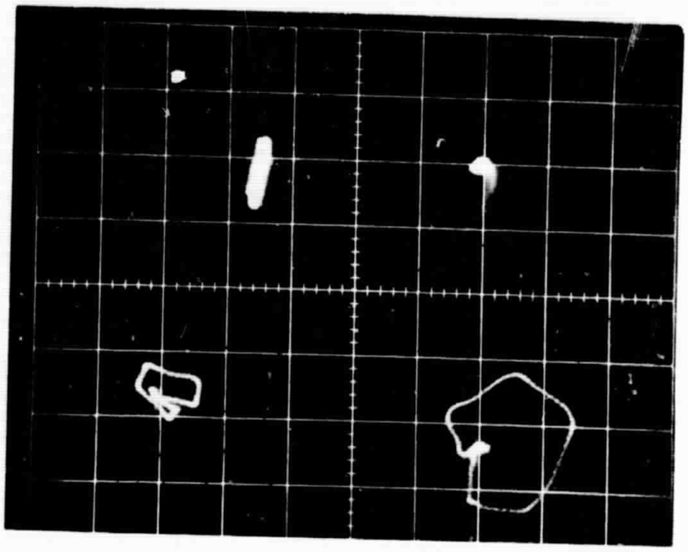

12,000 RPM - 26 psig

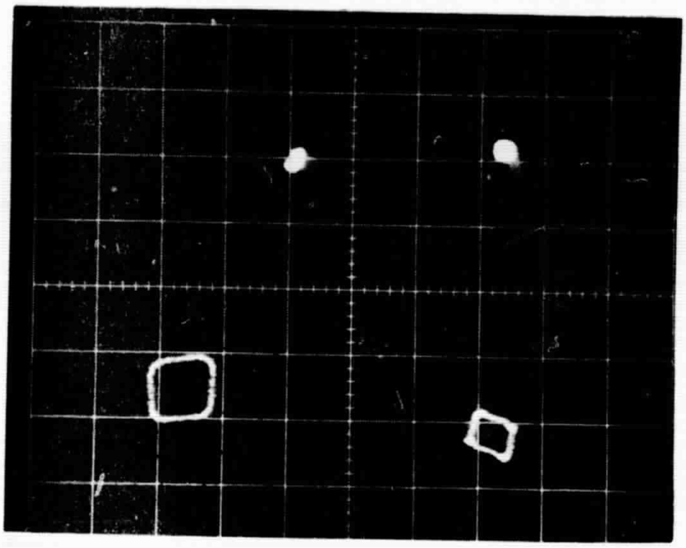

18,000 RPM - 80 psig

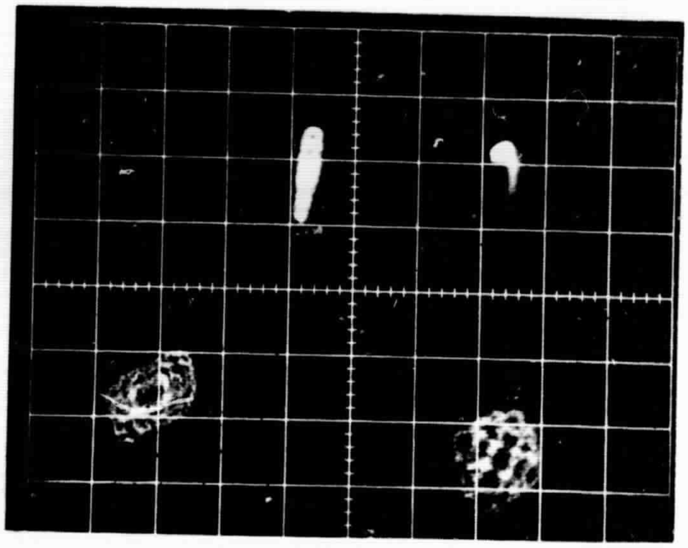

18,000 RPM - 35 psig

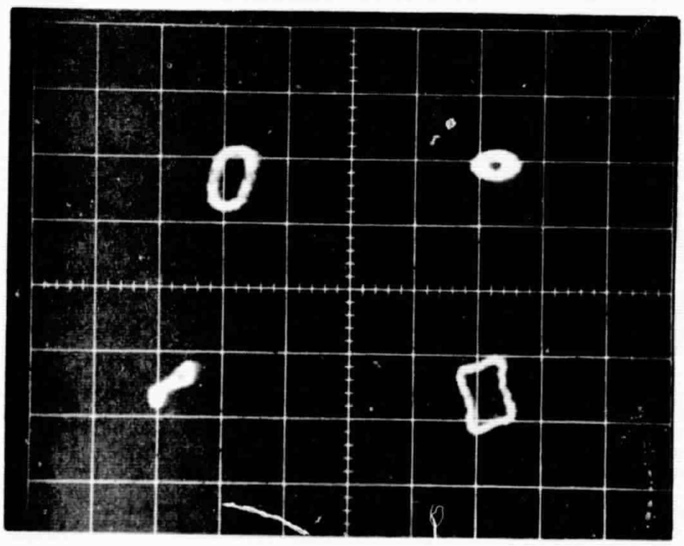

24,000 RPM - 72 psig

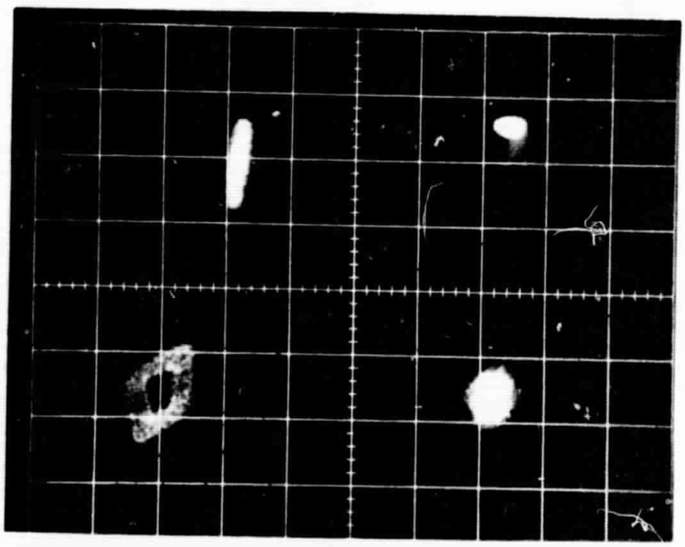

24,000 RPM - 38.5 psig

(Fig. 33 Continued →)

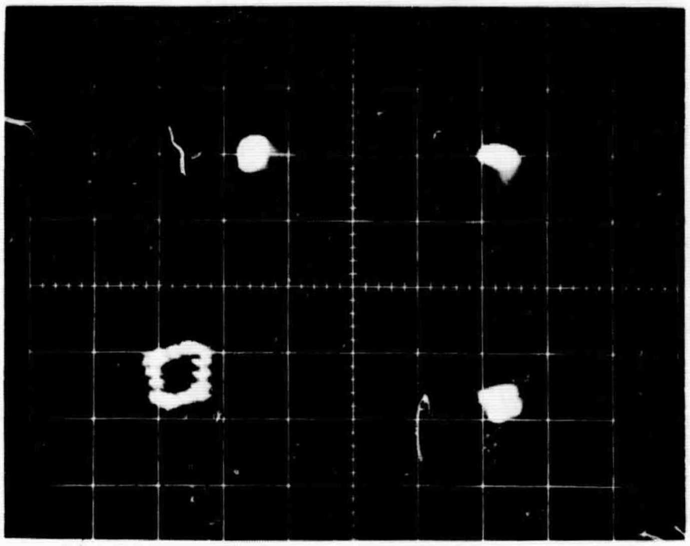

27,000 RPM - 64 psig

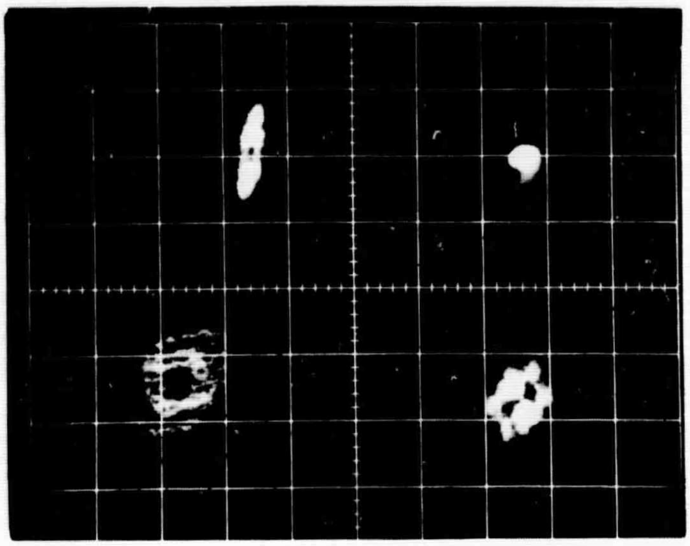

27,000 RPM - 40 pgis

(End of Fig. 33)

6.4 Hydrodynamic Tests In The Vertical Position

The rotor was operated hydrodynamically in the vertical position up to 12,000 rpm. The rotor whirled at all speeds with large amplitude. The whirling mode was cylindrical and the frequency approximately one-half the rotational frequency. The shaft motion was lagging the rotor motion, but the phase angle was not determined. In this test, the dashpots were re-installed to reduce the amplitude of shaft motion. The flexible supports were mounted in rubber bushings, but the support stiffness was somewhat higher (4,000 lb/in.) than in the horizontal position (2,300 lb/in.). In vertical hydrodynamic operation, closing or opening the journal bearing feeding holes did not have any effect on journal bearing performance. Photographs of the test results from 1,000 rpm to 12,000 rpm are shown in Figure 34.

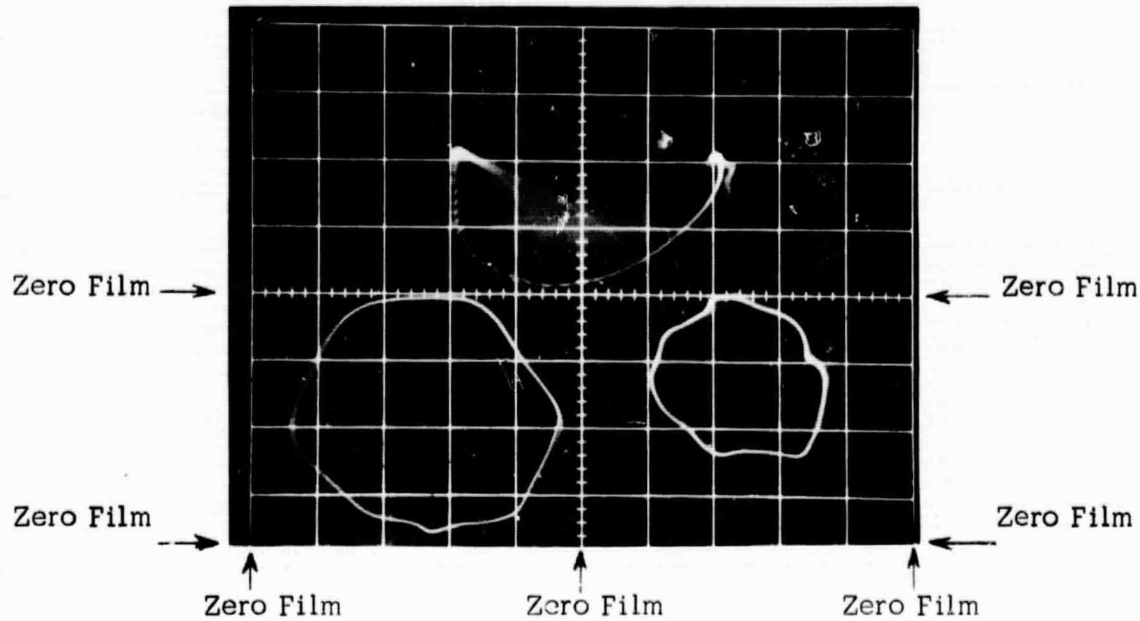

1,000 RPM

Top Left Orbit: Compressor End Shaft (Journal) Motion
Top Right Orbit: Turbine End Shaft (Journal) Motion
Bottom Left Orbit: Compressor End Rotor (Bearing) Motion
Bottom Right Orbit: Turbine End Rotor (Bearing) Motion

Oscilloscope Calibration: Vertical and Horizontal 0.5 mils/major division
(For Shaft Orbits Only)

Rotor Vertical
Hydrodynamic Operation
Rotor Whirling Frequency: one-half rotational frequency
Average Flexible Support Stiffness: 4,000 lb/in (per support)
Average Damping Coefficient: 4 lb-sec/in (per dashpot)

Fig. 34 - Oscilloscope Traces of Shaft Orbits Relative to the Frame and Rotor Orbits Relative to the Shaft - Rotor Vertical, Hydrodynamic Operation, Support Stiffness 4,000 lb/in.

(Fig. 34 Continued →)

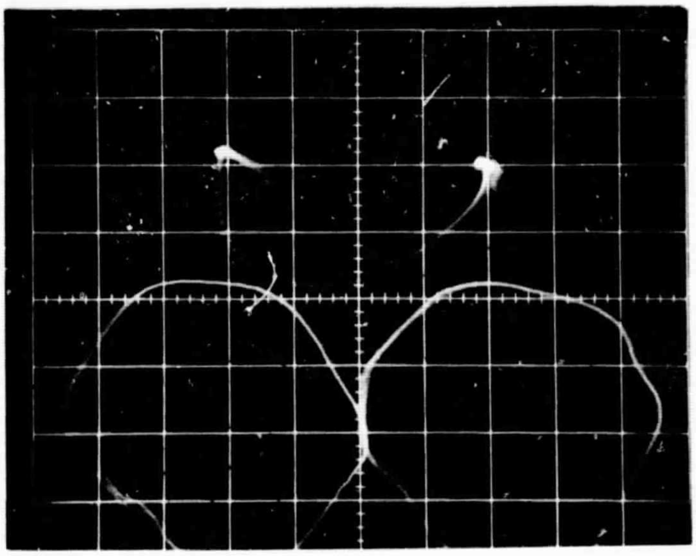

3,000 RPM

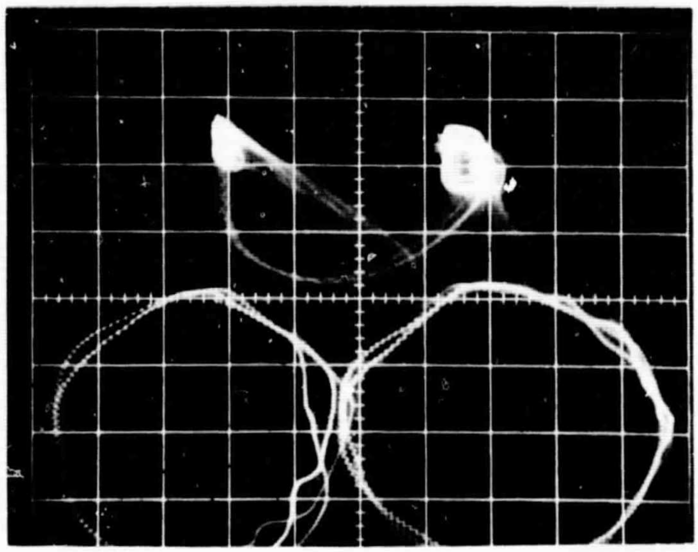

6,000 RPM

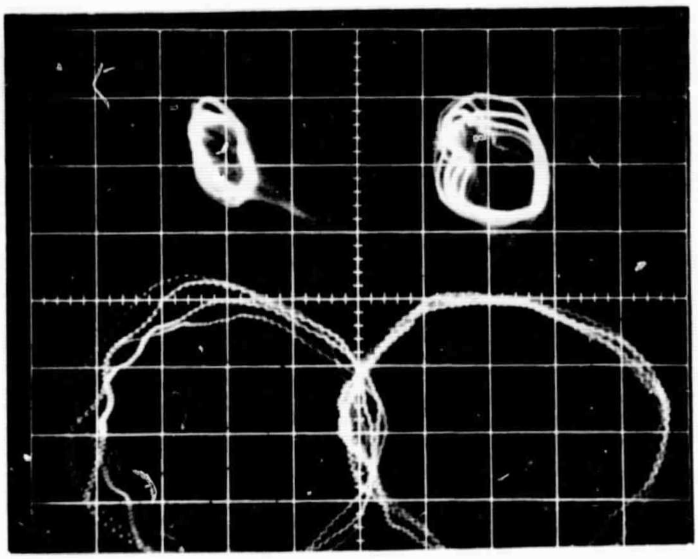

9,000 RPM

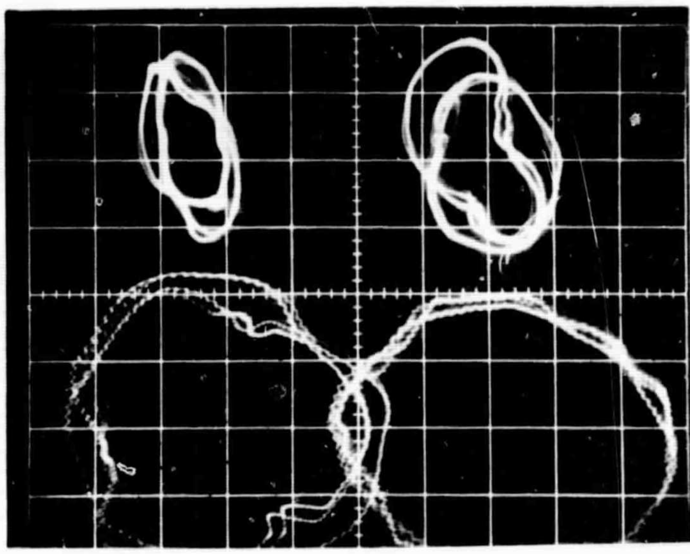

12,000 RPM

(End of Fig. 34)

6.5 Comparison Of The Test Results

Figure 35 is a plot of the hydrostatic test results and the calculated fixed shaft whirl threshold. The fixed shaft whirl threshold speed was calculated by the equation:

$$N_w = 9.55\, R \sqrt{\frac{2K}{M_r}} = 162.8 \sqrt{K} \tag{10}$$

where:

N_w = whirl threshold speed, rpm

R = whirl ratio = 2

K = measured hydrostatic film stiffness per journal bearing, lb/in. (see Fig. 25)

M_r = mass of the rotor = 0.02752 lb-sec^2/in.

The following conclusions can be made from Figure 35.

a. For the same support stiffness at a given supply pressure the whirl threshold speed is higher in the horizontal position than in the vertical.

b. In the horizontal position, lowering the support stiffness makes it possible for the journal bearings to operate hydrodynamically (0 psig) at high speeds.

c. In the vertical position, lowering the support stiffness reduces significantly the required supply pressure for journal bearing stability.

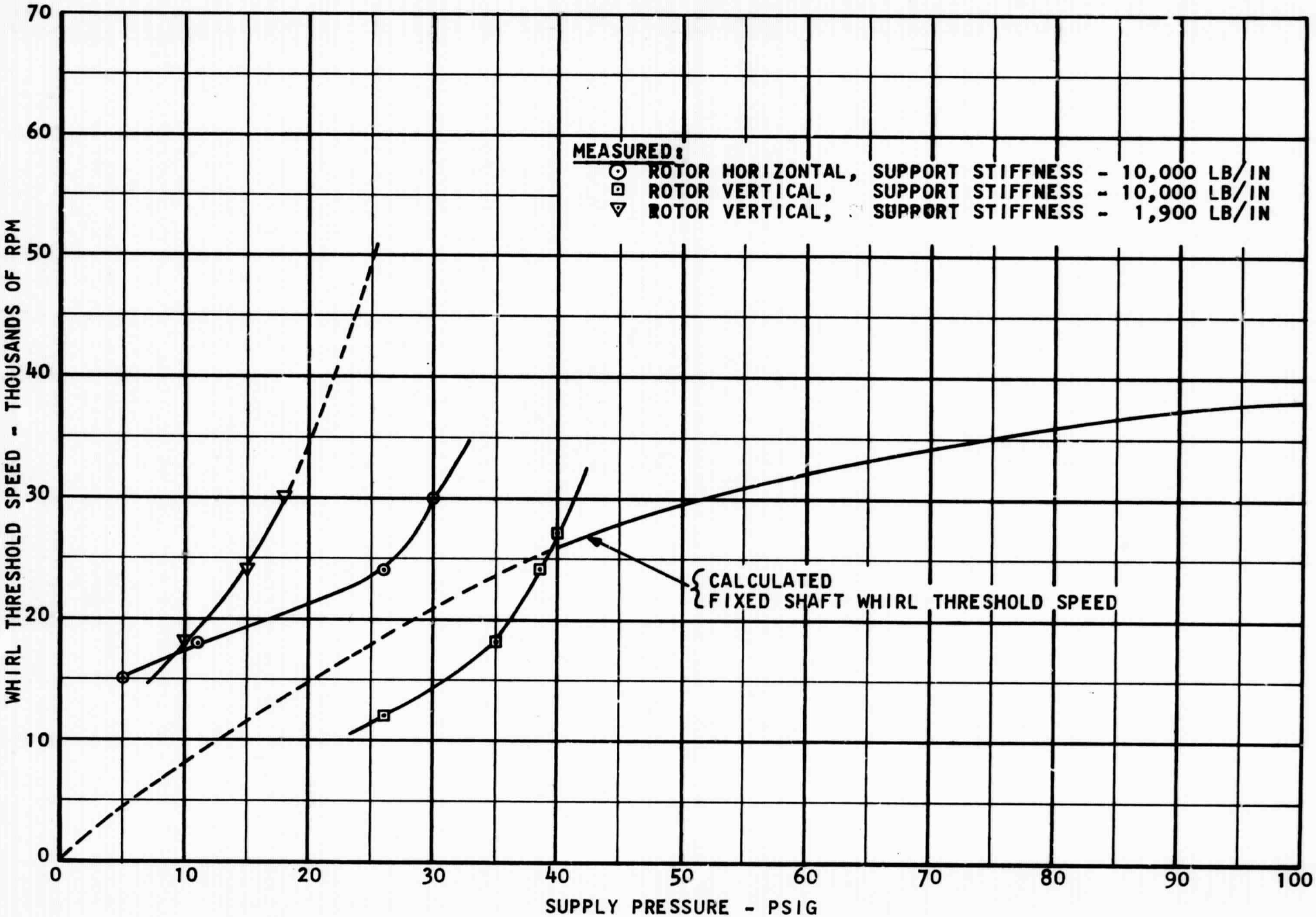

Fig. 35 - Comparison Between Calculated Fixed Shaft and Measured Flexibly Supported Shaft Whirl Threshold Speeds vs. Supply Pressure

7.0 BEARING POWER LOSS

From Reference (2) the total bearing frictional power loss at 38,500 rpm (operating speed) was 156 watts; 45 watts for the two journal bearings and 111 watts for the thrust bearing.

For the stable operation of the journal bearings in the vertical position at 38,500 rpm the required supply pressure is 21.5 psig (by extrapolation from Figure 35). The calculated flow rate for both journal bearings at 21.5 psig supply pressure is 1.9 lbs/hr. This corresponds to a pumping power loss of 18 watts. The combined, frictional and pumping, power loss for the two journal bearings at 38,500 rpm will be 63 watts. This is less by approximately a factor of two, than the frictional power loss of the tilting-pad journal bearing of the radial flow turbocompressor.

Therefore, the use of low supply pressures will ensure journal bearing stability in the vertical position and the total bearing power loss of 174 watts will be well below the permissible maximum limit of 350 watts.

8.0 BEARING SEIZURE

A bearing seizure occurred when the rotor was operating hydrodynamically at 12,000 rpm in the vertical position. Also, a crack was observed at the beryllium ring when the rotor came to a stop. The rotor was disassembled and it was found that the seizure had occurred at the compressor end journal bearing. It is expected that heat generated by journal and sleeve rubbing caused swelling or chipping of the epoxy which resulted in seizure. As mentioned previously, attempts to coat with chrome oxide the epoxy which insulates the brass capacitor from the shaft were not successful. The appearance, after seizure, of the compressor and turbine end journals is shown in Figure 36. It has not been possible to determine whether the beryllium ring cracked before or after the seizure. Some cracking may have initiated during high speed operation and broke completely when seizure occurred. The cracked beryllium ring is shown in Figure 37. As can be seen, the edges of four holes were not good to begin with. During drilling some of the beryllium flaked and came off from the edges of the holes.

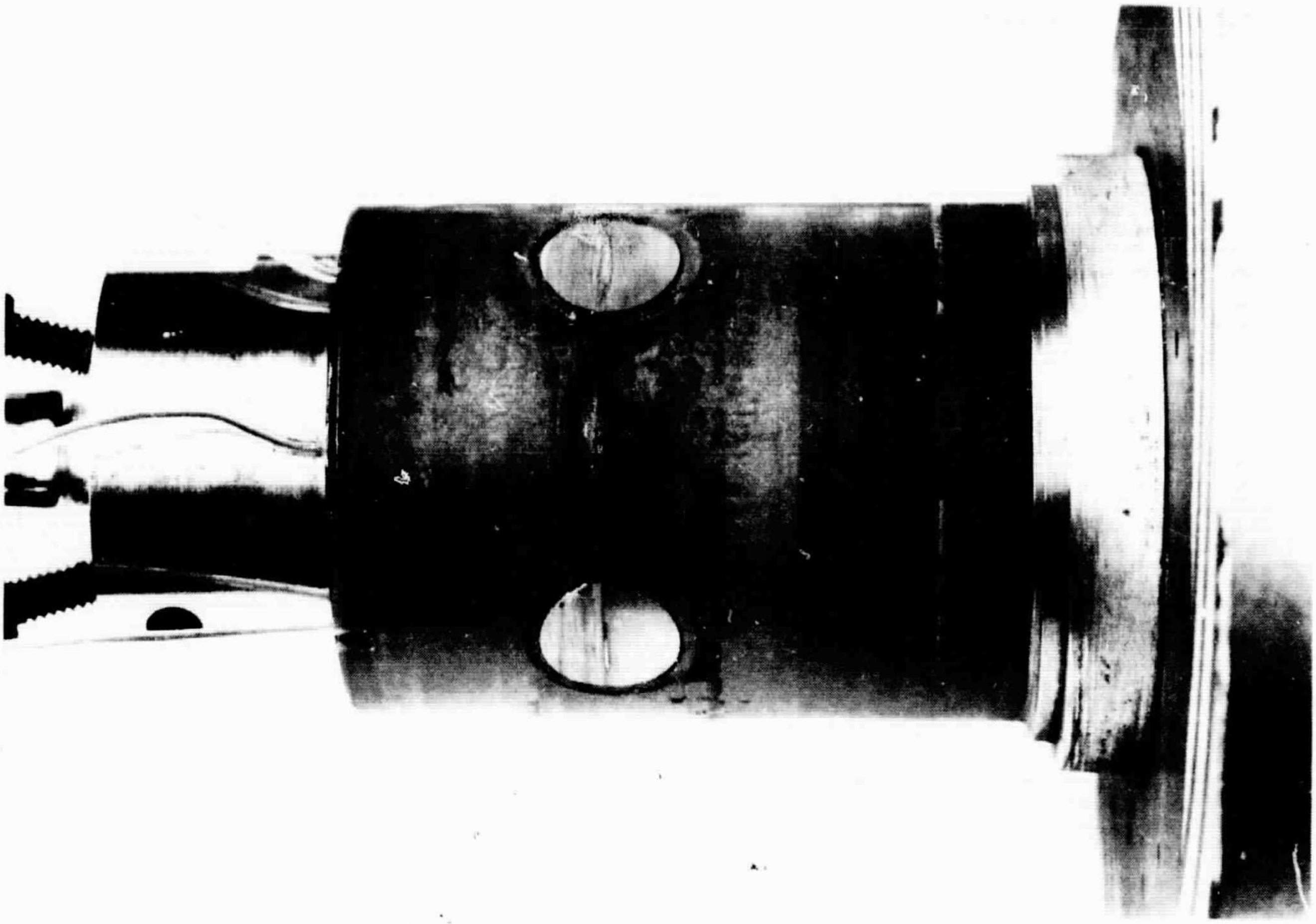

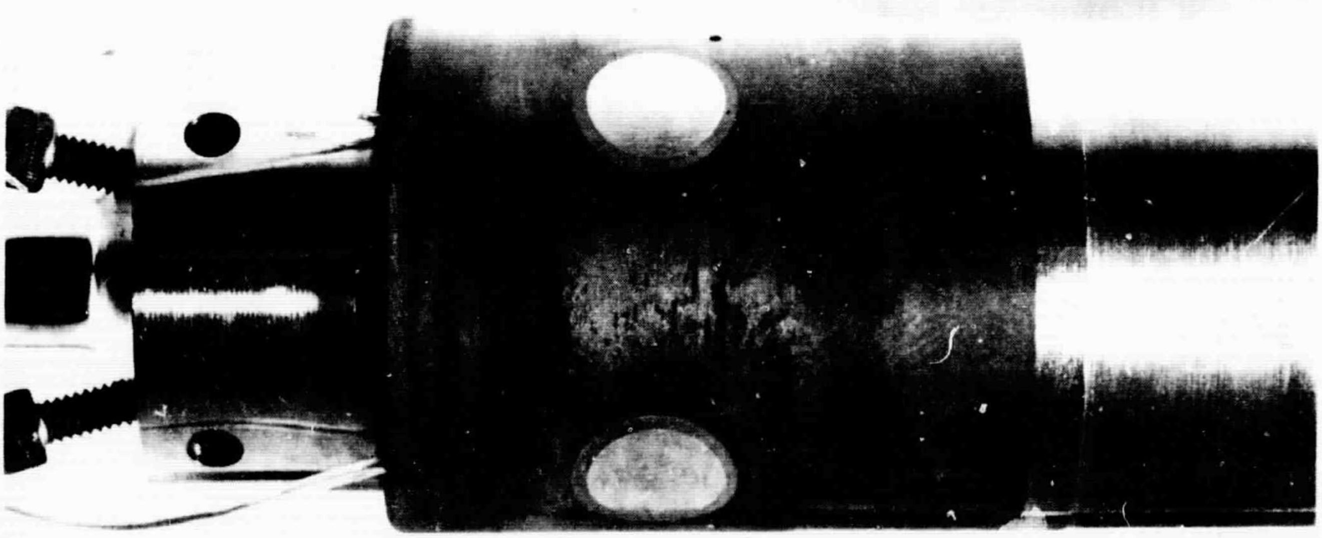

Fig. 36 - Compressor End (Upper) and Turbine End (Lower) Shaft Bearing Surfaces After Seizure. Chrome-Oxide Coated Surfaces.

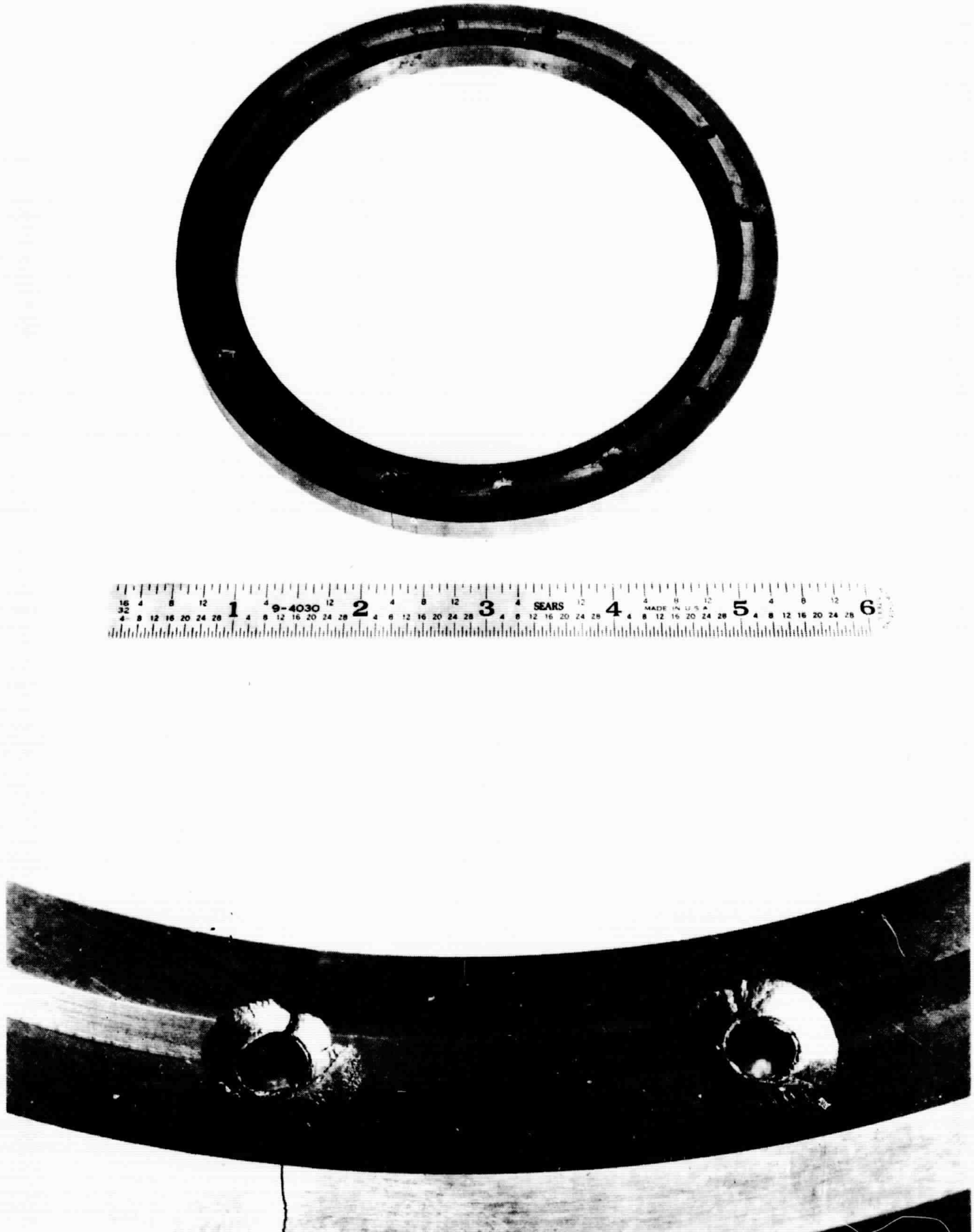

Fig. 37 - Beryllium Ring (Upper) and Close-Up View of Cracked Portion (Lower).

9.0 CONCLUSIONS

A gas bearing simulator for the Brayton cycle radial flow turbocompressor has been designed, built and tested in ambient air. The simulator employs the Linde-developed gas bearing system, in which the gas lubricated rotor rides on a stationary, flexible-supported, and damped shaft. The advantages of this gas bearing system are:

a. Stable operation
b. Low bearing power loss
c. Thermal isolation of the bearings from the housing
d. Large bearing running clearances
e. Elimination of a gimbal mount for the thrust bearing
f. Reliable operation

Dynamic tests in the horizontal and vertical positions indicated that the threshold of journal bearing stability is affected very strongly by the stiffness of the flexible supports. The amount of damping (within the investigated range) did not have any appreciable effect on the stability. In the horizontal position the rotor was operated hydrodynamically up to 36,000 rpm, and the vertical position up to 30,000 rpm with low hydrostatic supply pressures. The pumping and frictional power loss of this bearing system is less than the frictional power loss of the tilting-pad gas bearing system.

This gas bearing system offers a potentially stable rotor support system to meet the design requirements for turbocompressors.

APPENDIX

Rotor Deflections And Stresses

The following is a description of the computer program by which the deflections and stresses of the rotor were calculated.

A program has been developed for high speed computation of deflections and stresses in heavy walled members with axial symmetry under various combinations of surface and body loadings. It is particularly appropriate for analyzing centrifugal force effects in rotating machine elements.

The theoretical basis for the program is the "direct stiffness" or "finite deformation" technique which is being widely discussed in current engineering journals. The approach consists of developing a Green's function, or master stiffness matrix for the member being analyzed. To develop this matrix, the member is regarded as being composed of a large number of annular rings of rectangular cross section. An 8 x 8 stiffness matrix is developed for each such elemental ring, and then the master matrix (which might be as large as 100 x 100) is developed by appropriate superposition of the elements. Finally, the master matrix is inverted to determine deflections at all mesh points of the member cross section due to the applied forces. Knowledge of these deflections in turn permits computation of stresses throughout the member.

The program is implemented throughout by matrix representation. The subtlest point technically is in the development of the minor, 8 x 8, stiffness matrix for each of the elements. To do this, the element is assumed to have a displacement function very simply expressed in terms of the independent variables r and z. This in turn permits deflections in each such element to be expressed in terms of the deflections of its corner points (as they appear in a meridianal cross section). The displacement functions are also chosen simply enough so that at least within a typical element, straight lines in an r, z plane deflect into straight lines. Then by keeping track of the corner point deflections, we can be assured that no gaps or overlapping occurs among elements. In other words, locally the compatibility conditions are satisfied exactly. Locally the equilibrium conditions are only approximately satisfied, but the solution approaches the exact theoretical solution as the element size becomes smaller.

In our typical analyses to date, we have employed about 30 elemental rings and about 50 pivotal points in a member cross section.

SYMBOLS

A	dashpot viscous shear area, $in.^2$
B	dashpot viscous damping coefficient, lb-sec/in.
E	modulus of elasticity, psi
f_n	natural frequency of vibration of rotor, cycles/sec.
g	dimensional constant = 386.09 $in\text{-}lb_m/lb_f\text{-}sec.^2$
h	dashpot or thrust bearing gap, in.
I_r	rotor (transverse-polar) moment of inertia, $lb\text{-}sec^2\text{-}in.$
I_s	shaft transverse moment of inertia, $lb\text{-}sec^2\text{-}in.$
J	Joule constant = 778 ft-lb/Btu
K	journal bearing hydrostatic film stiffness, lb/in.
K_f	journal bearing hydrodynamic film stiffness, lb/in.
K_s	flexible support stiffness, lb/in.
k	coefficient of thermal conductivity, Btu/sec-ft-°F
ℓ	dashpot overlapping distance, in.
ℓ_f	distance from c.g. of rotor to journal brg. center, in.
ℓ_s	distance from c.g. of shaft to flexible support, in.
M_r	mass of rotor, $lb\text{-}sec^2/in.$
M_s	mass of shaft, $lb\text{-}sec^2/in.$
N_w	fixed shaft hydrostatic whirl threshold speed, rpm
R	hydrostatic whirl ratio
Rg	thrust bearing inside groove radius, in.
R_i	thrust bearing inside radius, in.
R_o	thrust bearing outside (groove) radius, in.
r	radial coordinate of spiral groove, in.
r_i	inside radius of rotor at journal brg., in.
r_o	outside radius of rotor at journal brg., in.
t	time, sec.
X	amplitude of vibration of shaft at time t, cm.

X_o	initial amplitude of vibration of shaft, cm.
x	translational coordinate of c.g. of rotor, in.
y	translational coordinate of c.g. of shaft, in.
α	coefficient of linear thermal expansion, per °F
β	groove angle, degrees
Δc	centrifugal growth of journal brg. radial clearance, in.
Δh	thermal distortion of thrust stator, in.
θ	angular coordinate of spiral groove, or angular coordinate of c.g. of rotor rotation, radians
μ	viscosity of air or silicone fluid, lb-sec/in^2
ν	Poisson's ratio
ρ	density, lb/in^3
ϕ	angular coordinate of c.g. of shaft rotation, radians
ω	rotor speed, rad/sec.

REFERENCES

1. "Design Of Gas Bearings" Mechanical Technology, Inc., Latham, New York, June, 1966, Vol. I, Sections: 5.3, 5.5, 6.1, 6.3, and 8.1.

2. Lukas, S. V., "Analysis Of A Gas Bearing System With Shaft Damping For Stability" Final Report NASA CR-72246, June, 1967, Contract NAS3-8516.

3. Tondl, A., "The Effect Of The Out-Of-Roundness Of Journals On Rotor And Bearing Dynamics" (in English) Acta Technica, CSAV 12, 1, 62-79 (1967).

REPORT DISTIRUBTION LIST FOR
CONTRACT NAS3-10927

NASA-Lewis Research Center
21000 Brookpark Road
Cleveland, Ohio 44135
Attention: H. B. Tryon, MS 500-201 (3)
W. J. Anderson, MS 23-2
D. G. Beremand, MS 500-201
H. O. Slone, MS 500-201
J. H. Dunn, MS 500-201
G. M. Bode, MS 21-4
J. A. Heller, MS 500-201
B. Lubarsky, MS 3-3
T. A. Moss, MS 500-201
Z. N. Nemeth, MS 6-1
J. E. Dilley, MS 500-309
Technology Utilz. Office, MS 3-19
D. R. Packe, MS 500-201
Library, MS 60-3 (2)
Report Control Office, MS 5-5
V. F. Hlavin, MS 3-14
R&QA Office, MS 500-111
R. E. English, MS 500-201
D. P. Fleming, MS 6-1
R. E. Cunningham, MS 6-1

NASA Goddard Space Flight Center
Greenbelt, Maryland 20771
Attention: Library

NASA Langley Research Center
Langley Station
Hampton, Virginia 23365
Attention: Library

National Aeronautics & Space Administration
Washington, D. C. 20546
Attention: H. D. Rochen, Code RNP
Dr. F. Schulman, Code RNP
Arvin Smith, Code RNW

NASA Scientific & Technical Information Facility
P.O. Box 33
College Park, Maryland 20740
Attention: Acquisitions Branch (SQT-34054)

NASA Ames Research Center
Moffett Field, California 94035
Attention: Library

NASA Flight Research Center
P.O. Box 273
Edwards, California 93523
Attention: Library

NASA Manned Spacecraft Center
Houston, Texas 77058
Attention: Tony Redding

Jet Propulsion Laboratory
4800 Oak Grove Drive
Pasadena, California 91103
Attention: Library

U.S. Army Engineer R&D Labs.
Gas Turbine Test Facility
Fort Belvoir, Virginia 22060
Attention: W. Crim

Office of Naval Research
Department of the Navy
Washington, D. C. 20025
Attention: Dr. Ralph Roberts

Bureau of Ships
Department of the Navy
Washington, D. C. 20025
Attention: G. L. Graves

Bureau of Naval Weapons
Department of the Navy
Washington, D. C. 20025
Attention: Code RAPP

Institute for Defense Analyses
400 Army-Navy Drive
Arlington, Virginia 22202
Attention: Librarian

Power Information Center
University of Pennsylvania
Room 2107
3401 Market Street
Philadelphia, Pennsylvania 19104

NASA Manned Spacecraft Center
Houston, Texas 77058
Attention: Library

NASA Marshall Space Flight Center
Huntsville, Alabama 35812
Attention: Library

Wright-Patterson AFB, Ohio 45433
Attention: George Thompson
(APFL, Air Force Aero Propulsion)

Air Force Systems Command
Aeronautical Systems Division
Wright-Patterson AFB, Ohio 45433
Attention: Librarian

Aerojet-General Corporation
Von Karman Center
Azusa, California 91702
Attention: Librarian

Aerospace Corporation
P.O. Box 95085
Los Angeles, California 91745
Attention: Librarian

AVCO-Bay State Abrasives Division
Westbord, Massachusetts 01581
Attention: Mr. G. Herterick

AiResearch Manufacturing Company
The Garrett Corporation
402 South 36th Street
Phoenix, Arizona 85034
Attention: Librarian
E. L. Wheeler

AiResearch Manufacturing Company
The Garrett Corporation
9851 Sepulveda Boulevard
Los Angeles, California 90009
Attention: Librarian

Bendix Research Labs Division
Southfield (Detroit), Mich. 48232
Attention: Librarian

The Boeing Company
Aerospace Division
Box 3707
Seattle, Washington 98124
Attention: Librarian

Borg-Warner Corporation
Pesco Products Division
24700 North Miles Road
Bedford, Ohio 44014
Attention: Librarian

Continental Aviation & Engineering Corp.
12700 Kercheval Avenue
Detroit, Michigan 48215
Attention: Librarian

Curtiss-Wright Corporation
Wright Aero Division
Main & Passaic Streets
Woodridge, New Jersey 07075
Attention: Librarian

McDonnell Douglas Corporation
Douglas Aircraft Company Division
3000 Ocean Park Boulevard
Santa Monica, California 90406
Attention: Librarian

McDonnell Douglas Corporation
Lambert Field
St. Louis, Missouri 63166
Attention: Librarian

Battelle Memorial Institute
505 King Avenue
Columbus, Ohio 43201
Attention: Librarian

Franklin Institute Laboratories
Benjamin Franklin Parkway at 20th St.
Philadelphia, Pennsylvania 19103
Attention: Otto Decker

General Dynamics Corporation
16501 Brookpark Road
Cleveland, Ohio 44142
Attention: Librarian

General Electric Company
FPLD
Cincinnati, Ohio 45215
Attention: Librarian

General Electric Company
Missile and Space Division
Cincinnati, Ohio 45215
Attention: M. A. Zipkin

General Electric Company
Mechanical Technology Laboratory
R&D Center
Schenectady, New York 12301
Attention: Librarian

General Electric Company
Missile & Space Vehicle Department
3198 Chestnut Street
Philadelphia, Pennsylvania 19104
Attention: Librarian

General Motors Corporation
Indianapolis, Indiana 46206
Attention: Librarian

Lear Siegler, Inc.
3171 S. Bundy Drive
Santa Monica, California 90406
Attention: Librarian

Massachusetts Institute of Technology
Cambridge, Massachusetts 02139
Attention: Librarian

Mechanical Technology Inc.
968 Albany-Shaker Road
Latham, New York 12110
Attention: Librarian
E. B. Arwas
P. W. Curwen

North American Rockwell Corporation
North American Aviation, Inc.
Space and Information Systems Div.
Downey, California 90241
Attention: Librarian

Northern Research & Engineering Co.
219 Vassar Street
Cambridge, Massachusetts 02139
Attention: Librarian

Pratt & Whitney Aircraft
400 Main Street
East Hartford, Connecticut 06108
Attention: Librarian

Space System Division
Los Angeles Air Force Station
Los Angeles, California 90045
Attention: Librarian

Solar, Div. of International Harvester
2200 Pacific Highway
San Diego, California 92112
Attention: Librarian

Space Technology Laboratories, Inc.
One Space Park
Redondo Beach, California 90278
Attention: Librarian

Sunstrand Denver
2480 West 70 Avenue
Denver, Colorado 80221
Attention: Librarian

TRW Accessories Division
23555 Euclid Avenue
Cleveland, Ohio 44117
Attention: Librarian

Pratt & Whitney Aircraft
SWEF
Governors Highway
South Windsor, Connecticut 06074
Attention: R. Cohen

University of Maryland
College of Engineering
College Park, Maryland 20740
Attention: M. E. Talaat

University of Virginia
School of Engineering & Applied Science
Department of Mechanical Engineering
Charlottesville, Virginia 22903
Attention: Dr. E. Gunter, Jr.

Westinghouse Electric Corporation
Astronuclear Laboratory
P.O. Box 10864
Pittsburgh, Pennsylvania 15236
Attention: Librarian

Williams Research
Walled Lake, Michigan 48088
Attention: Librarian